PHOTOPHYSICOCHEMICAL PROPERTIES AND SURFACE-ENHANCED RAMAN SCATTERING OF PHTHALOCYANINE-NANOPARTICLE CONJUGATES

A thesis submitted in fulfilment of the requirements

For the degree of

MASTER OF SCIENCE

RHODES UNIVERSITY

By

NNAMDI NWAHARA

April 2018

DEDICATION

To My Parents (Davidson and Happiness Nwahara),

My siblings Queenett and Esther

ACKNOWLEDGEMENTS

"Not by power, nor by might, but by my Spirit, says the Lord." The Lord has been gracious.

My sincere and heartfelt gratitude goes to my supervisor, Distinguished Professor Tebello Nyokong for her invaluable guidance and mentorship throughout this Master's work. You introduced me to the wonderful field of nanochemistry, and granted me freedom in my investigations of interesting research topics. Thank you Prof.

To my Romanian hosts; Prof. Ion and Nelu, you were very welcoming. It felt like I never left home. Thank you

Special thanks goes to Ms Gail Cobus, Dr Jonathan Britton, Dr John Mack, Dr Samson Khene and Mr Francis Chindeka for their support and help in the course of this research. I would be remiss not to thank the entire member of staff of Chemistry department of Rhodes University, as well as the EMU unit, Marvin and Shirley.

To my senior colleagues, friends and labmates; Dr Pitchuo Ngoy, Dr David Oluwole, Dr Munyaradzi Shumba and Dr Edward Sekhosana, Ojodomo Achadu, Sixolile Centane, Nwaji Njemuwa, Gugu Khubeka, Eric Ofei, Philip Magambo and Reitumetse Nkhahle as well as the entire S22, Thank you all for your support.

The National Research Foundation (NRF) of South Africa, Desmond Goddard Bursary, and Rhodes University are acknowledged for their financial support. Opinions expressed and conclusions arrived at, are those of the author and are not necessarily to be attributed to the NRF or any other sponsor.

ABSTRACT

This work presents the synthesis, photophysical and photochemical characterization of a series of metallophthalocyanines (MPcs) and boron dipyrromethene (BODIPY) and their conjugates with either gold or silver nanoparticles (AuNPs or AgNPs) or graphene quantum dots (GQDs). The rich π-electron systems of GQDs and MPcs employed in this work enabled the coordination of MPcs to GQDs (either as pristine or modified) via the non-covalent (π-π stacking) method. GQDs, AuNPs and AgNPs were also functionalized with L-glutathione (GSH) in order to assist coupling to the Pcs or BODIPY dye. Spectroscopic and microscopic studies confirmed the formation of the respective nanoparticles (NPs) as well as the conjugates which exhibited enhanced photophysicochemical properties in comparison to the phthalocyanines (Pcs) or BODIPY alone. This work also shows that the incorporation of folic acid (FA) into Pcs-NPs composites leads to further enhancements in the singlet oxygen generation capabilities of the resulting conjugates, and so experimentally demonstrates for the first time, a synergy between FA and the respective nanoparticles (GQDs, AuNPs and AgNPs) in affecting the photophysical properties of Pcs complexes.

GQDs and Pcs/GQDs hybrids were also herein decorated with AuNPs – metallic nanostructures that employ localized surface plasmon resonances to capture or radiate electromagnetic waves at optical frequencies. These nanostructures herein reported, have been shown to possess enhanced light-matter properties, enabling unique surface-enhanced Raman scattering (SERS) behaviours, with unprecedented enhancement factors of up to 30-fold. This work therefore, reports on the fabrication of Pc/GQDs/AuNPs hybrids and experimentally demonstrates their incredible potential as novel Raman-active PDT agents.

CONTENTS

LIST OF ABRREVIATIONS

A.U. = Absorbance Unit

AgNSs = Silver nanospheres

AuNPs = Gold nanoparticles

AuNRs = Gold nanorods

AuNSs = Gold nanospheres

$CDCl_3$ = Deuterated Chloroform

CTAB = Cetyltrimethylammonium bromide

DBU = 1,8-Diazabicyclo-[5.4.0]-undec-7-ene

DCC = Dicyclohexylcarbodiimide

DCM = Dichloromethane

DMF = Dimethylformamide

DMSO = Dimethyl Sulfoxide

DMSO-d = Deuterated Dimethylsulfoxide

DPBF = 1,3-Diphenylisobenzofuran

DPE = Diphenyl Ether

EDC = N-(3-Dimethylaminopropyl)-N'-ethylcarbodiimide

FA = Folic acid

FRET = Forster Resonance Energy Transfer

FT-IR = Fourier Transform Infrared

GQDs = Graphene quantum dots

GSH = Glutathione

ISC = Intersystem Crossing

MPc = Metallophthalocyanine

NHS = N-hydroxysuccinimide

NMR = Nuclear Magnetic Resonance

NPs = Nanoparticles

NRs = Nanorods

NSs = Nanospheres

OA = Oleic Acid

OLA = Oleylamine

Pc = Phthalocyanine

ROS = Reactive oxygen species

RSD = Relative standard deviation

TEM = Transmission electron microscopy

UV-Vis = Ultraviolet-Visible

VR = Vibrational Relaxation

XPS = X-ray photoemission spectroscopy

XRD = X-ray powder diffraction

LIST OF SYMBOLS

Abs = Absorbance

F = Fluorescence intensity

α = Non-peripheral position

β = Peripheral position

λ = Wavelength

τ_F = Fluorescence lifetime

Φ_F = Fluorescence quantum yield

Φ_T = Triplet quantum yield

Φ_Δ = Singlet oxygen quantum yield

CHAPTER ONE

INTRODUCTION

INTRODUCTION

Preface: There is need a for phthalocyanine complexes with improved photophysicochemical properties, hence this thesis focuses on the influence of graphene quantum dots (GQDs), Au and Ag nanoparticles (AuNPs and AgNPs) on the photophysical and photochemical properties of selected metallophthalocyanines (MPcs). This section of the thesis provides a brief overview of the synthesis and properties of phthalocyanines (Pcs). The general properties, diverse uses and synthesis of GQDs, AuNPs and AgNPs, as well as their combination (covalently and non-covalently) with the MPcs of interest are also presented. The ensuing pages also present an overview of the selectivity of phthalocyanines, and the methods employed to improve Pcs cancer targeting ability for possible applications in photodynamic therapy (PDT). Folic acid was employed as a potential cancer marker, and is herein discussed. This work also reports on the influence of novel boron-dipyrromethene (BODIPY)-functionalized GQDs on the photophysical properties of Pcs. Such BODIPY/GQDs/Pcs supramolecular are herein reported for the first time. Since the Pcs-nanoparticle conjugates were employed in surface-enhanced Raman scattering (SERS), a small portion of this introduction is devoted to SERS and how such hybrid structures may hold promise for PDT dosimetry. The general outline of Pcs modification is illustrated in **Fig. 1.1**.

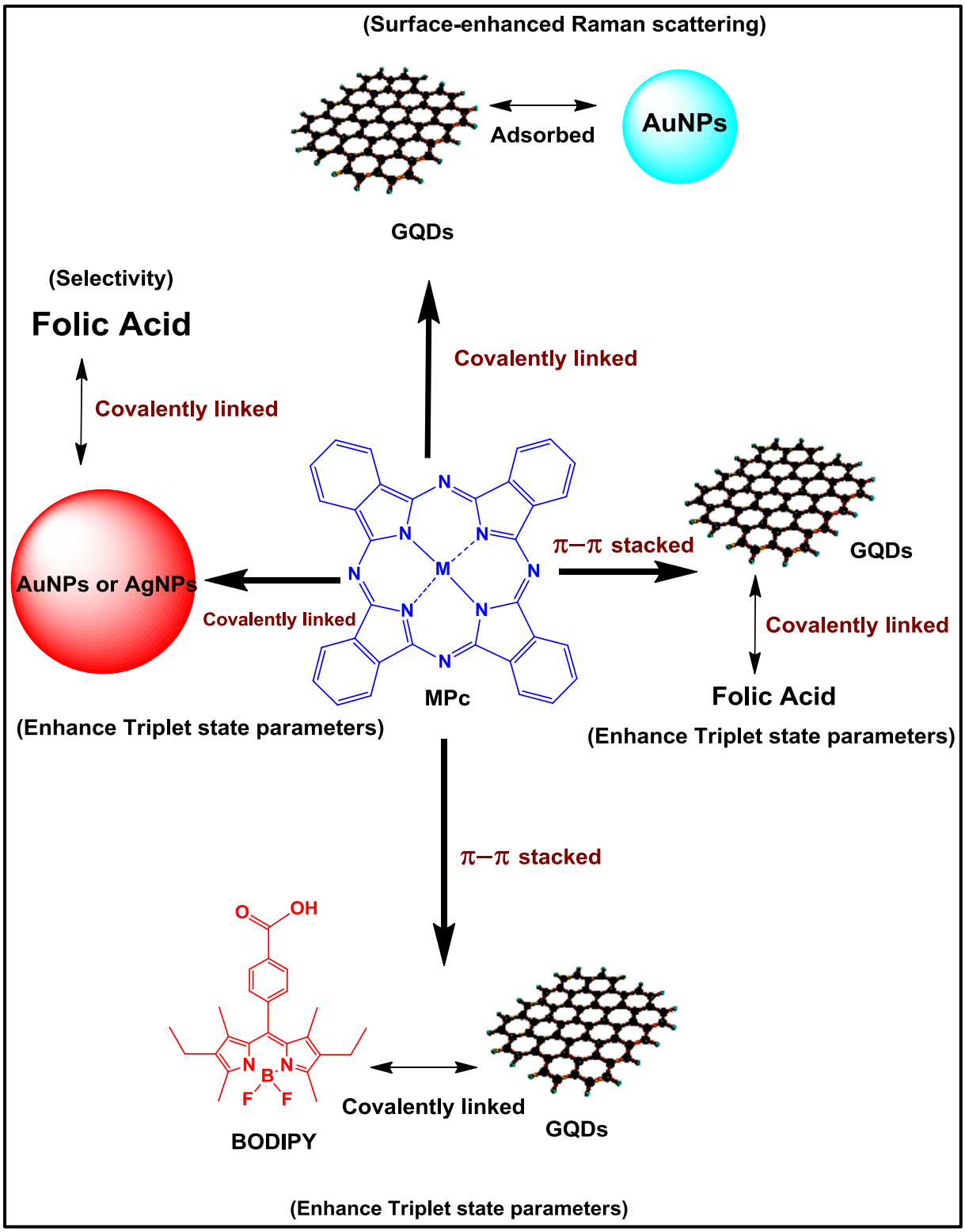

Figure 1.1. Illustration of various ways Pcs were modified in this study, highlighting intention behind each modification.

1. Introduction

1.1. Metallophthalocyanines

Phthalocyanines (Pcs) are two-dimensional 18 π-electron aromatic macrocycles [**1**] consisting of four isoindole sub-units linked together through nitrogen atoms (**Scheme 1.1**) [**2-4**]. Traditionally used as dyes, their architectural flexibility, high thermal, chemical and photochemical stability have allowed their application in a myriad of fields such as catalysis, optical limiting, and as photosensitizers (PS) in photodynamic therapy (PDT) [**5-10**]. Modifications in the Pc macrocycle can be made by incorporation of a variety of substituents to their outer hydrocarbon moiety. These substitutions can occur either at the non-peripheral (α) or peripheral (β) positions, modulating a varied number of important properties such as solubility and biocompatibility [**11**]. The central cavity in phthalocyanines can also allow for the inclusion of more than 70 different metals or metalloids into their inner core to form metallophthalocyanines (MPcs) by a coordinate-covalent bond between the nitrogen atoms and metal ions [**12**]. The general versatility and ease of synthesis of these macrocycles, as well as their interesting optical and electronic properties, make them highly attractive tools for the construction of functional hybrid materials [**13,14**].

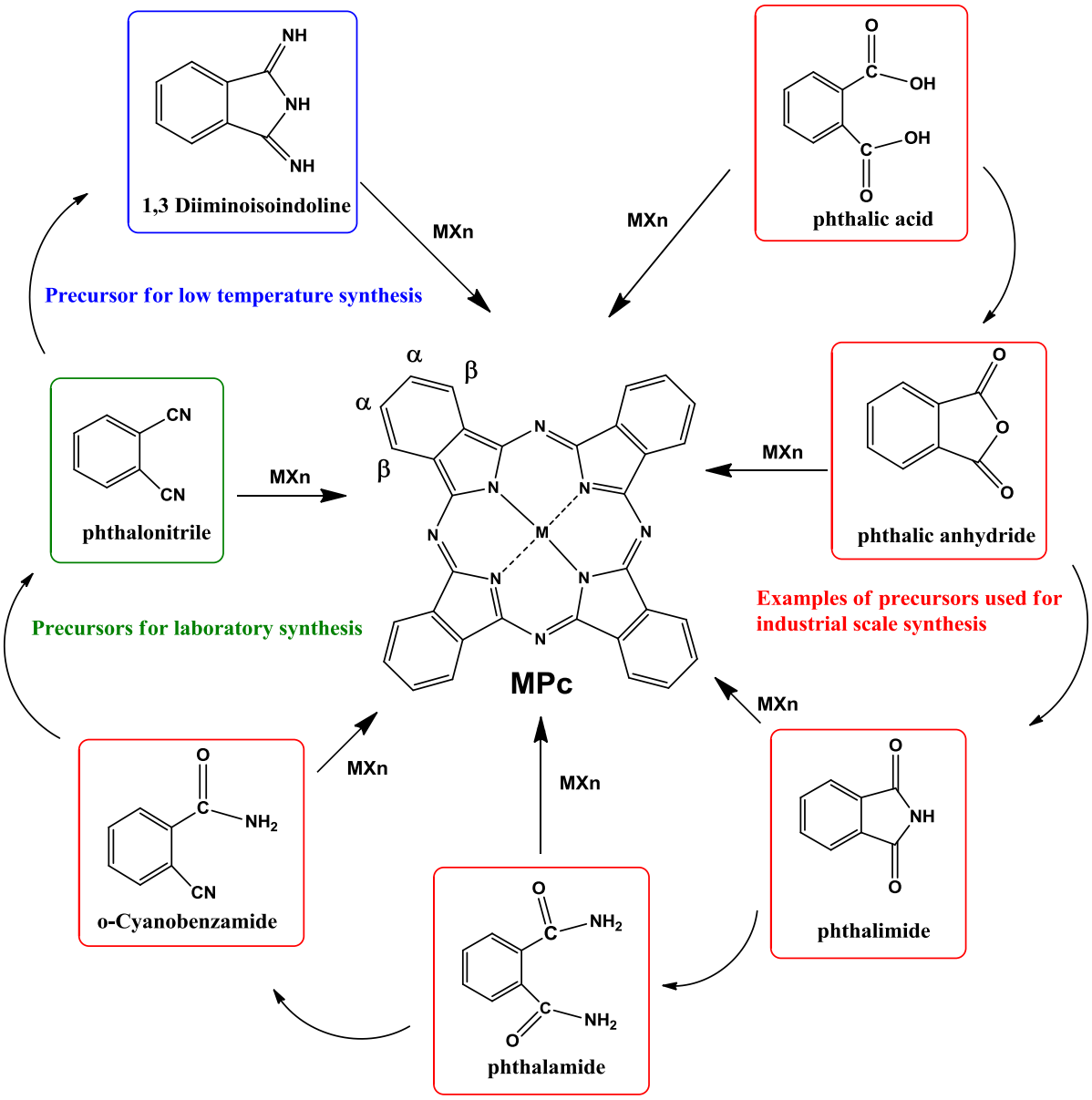

Scheme 1.1: Phthalocyanine ring showing potential sites for substitution (peripheral and non-peripheral positions) and synthesis from varied starting materials. MXn = Appropriate metal salt.

1.1.1. General synthesis of symmetrical and asymmetric MPcs

Phthalocyanines may be synthesized from a wide variety of starting materials (such as phthalimides, phthalamides, phthalic acids and anhydrides), depending on their particular application **Scheme 1.1** [**15-18**]. Within the laboratory environment however, phthalocyanine

synthesis generally involves the cyclotetramerization of a desired phthalonitrile (or dicyanobenzene) derivative. The reaction usually takes place in the presence of a suitable catalyst, the desired substituted phthalonitrile derivative and a metal salt of choice, with sufficient heating. Phthalocyanines with both four (tetra-substituted) and eight (octa-substituted) similar substituents can be made in this way. However, tetra-substitution leads to the formations of isomers, which can be difficult to separate from one another due to their comparable solubility in given solvents as well as similar retention factors. No attempts were made to isolate the isomers in the tetra-substituted phthalocyanines employed in this work.

The inherent uniformity of symmetrical Pcs often limits their application where specific binding or coordination with other molecules are needed. As a result, there has been a lot of interest on the design of asymmetrical Pcs. This stems from the fact that, besides allowing for specific binding, such Pcs exhibit better organization capabilities and improved physicochemical properties [**19**]. Amongst the numerous methods employed in the synthesis of asymmetric Pcs, statistical mixed condensation is the most common. The resulting Pcs bear one (B) isoindole sub-unit and three identical (A) sub-units (or vice versa) (AB_3 or A_3B) which usually affords a mixture of six compounds (**Scheme 1.2**). The desired asymmetrical structure is then obtained by separation of the different fractions formed via chromatographic methods. In this work, both symmetrical (tetra-substituted) and asymmetrical (AB_3 or A_3B) MPcs complexes were employed.

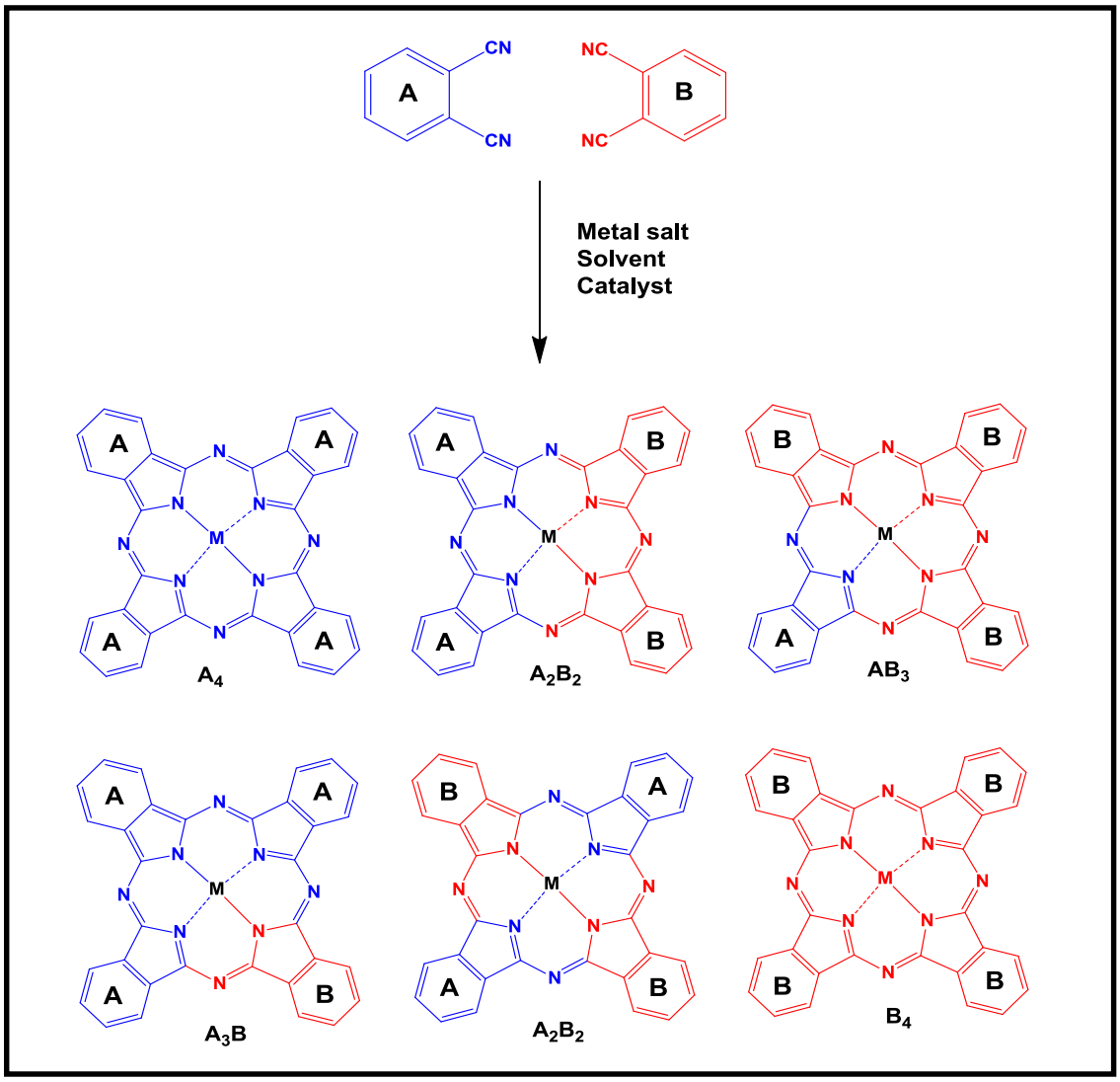

Scheme 1.2: Schematic representation of the synthesis of symmetric and asymmetric phthalocyanines.

1.1.2. UV-Vis spectra of MPcs

The densely conjugated π-electron network of phthalocyanines affords them intense absorption in the UV-Vis region. Their electronic spectra is also strongly influenced by whether or not they are metallated, the nature, number and position of substituents, amongst others [**11, 20,21**]. Their UV-Vis spectra is characterized by two major absorption bands, namely the Q-band and the B-band (**Fig. 1.2**). The Q-band can be attributed to electron transitions from the ground

state a_{1u} highest occupied molecular orbital (HOMO) to e_g lowest unoccupied molecular orbital (LUMO) in accordance with Gouterman's four orbital model, based on linear combination of atomic orbitals (LCAO) [**22-24**] (**Fig. 1.2 (Inset)**). The less intense B-band (consisting of two bands, B1 and B2) which occurs between 300-400 nm, can be attributed to two transitions $a_{2u} \rightarrow e_g$ and $b_{2u} \rightarrow e_g$, respectively (**Fig. 1.2 (Inset)**), often appearing broad.

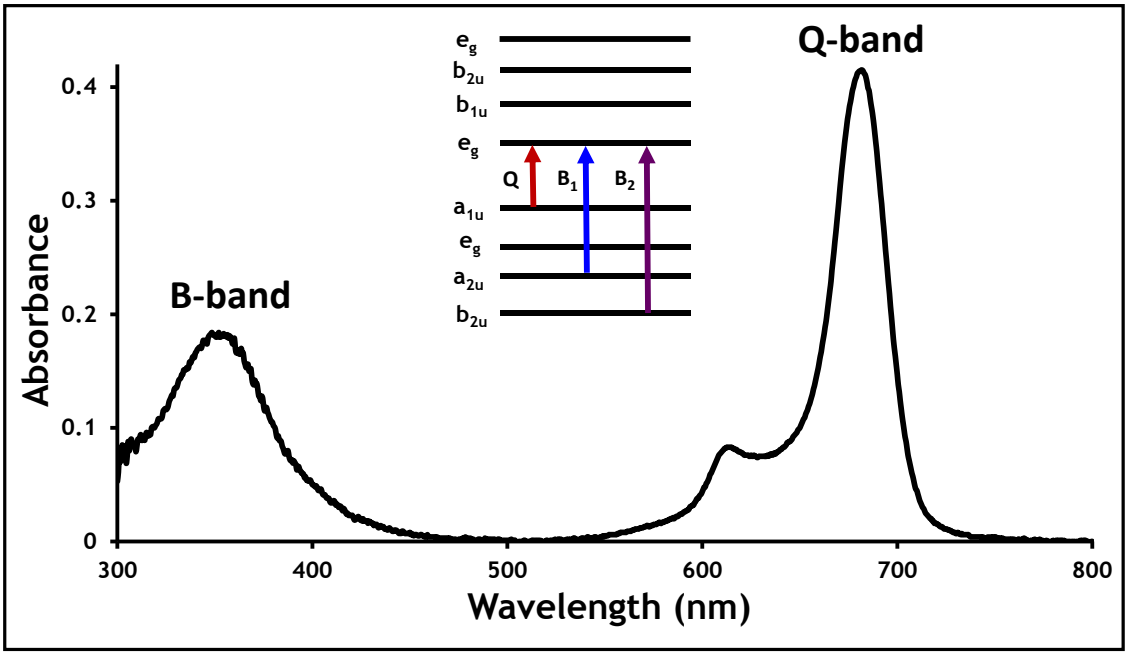

Figure 1.2. Typical UV-VIS spectrum of MPcs [Unpublished work].

In this work, Pcs were conjugated to nanoparticles (particles in a size range of 1–100 nm [**25]**). Nanomaterials differ greatly from their bulk materials [**26**], hence are able to tune the photophysical properties of Pcs. The study of Pcs-nanoparticle conjugates is therefore important. The nanoparticles of interest in this work are graphene quantum dots (GQDs), Au and Ag nanoparticles. These nanoparticles were linked to Pcs, hence introduction to these nanoparticles follows.

1.2 Graphene quantum dots

1.2.1. Background

Graphene quantum dots (GQDs) are an emerging class of zero-dimensional, oxygen-rich (epoxy, hydroxyl and carboxyl-containing) materials made up of few graphene sheets with lateral dimensions less than 20 nm [**27**] (**Fig. 1.3**). Research interest in GQDs largely stems from the fact that they exhibit exciton confinement and quantum-size effect, affording them exceptional properties such as high biocompatibility, robust chemical inertness, as well as excellent photostability [**27**]. Moreover, their relative ease of synthesis, coupled with low cytotoxicity, make them attractive alternatives to semiconductor quantum dots (SQDs) [**28,29**]. The quantum confinement effect in GQDs also provides the opportunity for the exploration of novel structural, optical, and electrical phenomena not easily attainable in other materials. All these, along with their excellent opto-electronics properties and high surface areas make them excellent nanomaterials that have found potential use in photovoltaics [**30-32**], sensing [**33,34**], photocatalysis [**35**], as well as photodynamic therapy (PDT) [**36**].

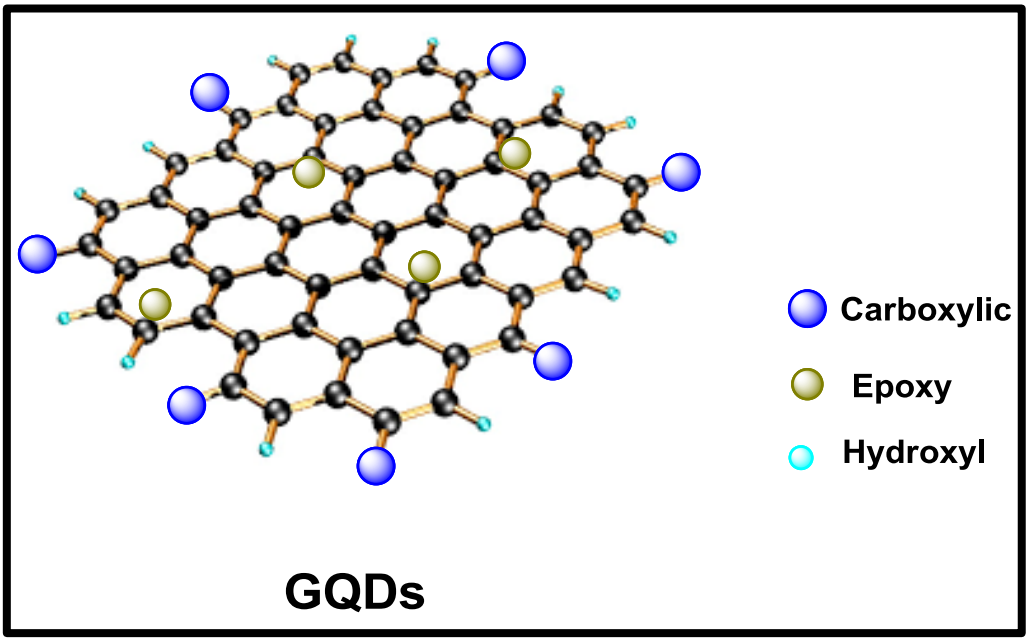

Figure: 1.3. General structure of graphene quantum dots (GQDs).

1.2.2. Synthesis

Various parameters such as the shape, size, surface characteristics, as well as opto-electrical properties of GQDs are largely dependent on the starting materials and the method of synthesis used. Two broad classes of synthetic methods are usually employed; namely top-down, and bottom-up approaches.

1.2.2.1. Top-down Approach

This approach generally involves the cleaving of bulk carbon-based materials into nanoscale GQDs via physical, chemical or electrochemical techniques. A wide selection of carbon sources have been employed using this synthetic route, including coal, graphite, graphene oxide, and carbon fibres. These precursors are usually subjected to acidic oxidation [**37,38**], hydrothermal or solvothermal treatment [**39-41**], chemical exfoliation [**42**] microwave or ultrasound assisted treatment [**43**] to obtain GQDs. A major drawback of this approach is the lack of precise control exercised over the morphology and size distribution of the particles produced, which are essential parameters in GQDs design.

1.2.2.2. Bottom-up Approach

Bottom- up route employs small organic molecules such as citric acid or as well as other aromatic structures as starting materials [**44**]. Techniques such as carbonization (direct pyrolysis) (**Fig. 1.4**) or assisted hydrothermal treatment through the use of autoclave reactors may be used. Unlike top-down, bottom-up approach introduces fewer defects, and affords good control over sizes, shapes and overall properties of the synthesized GQDs [**45**]. Bottom-up synthetic route, using citric acid as a starting material, was employed in this work for the synthesis of pristine (non-functionalized) GQDs with some modifications.

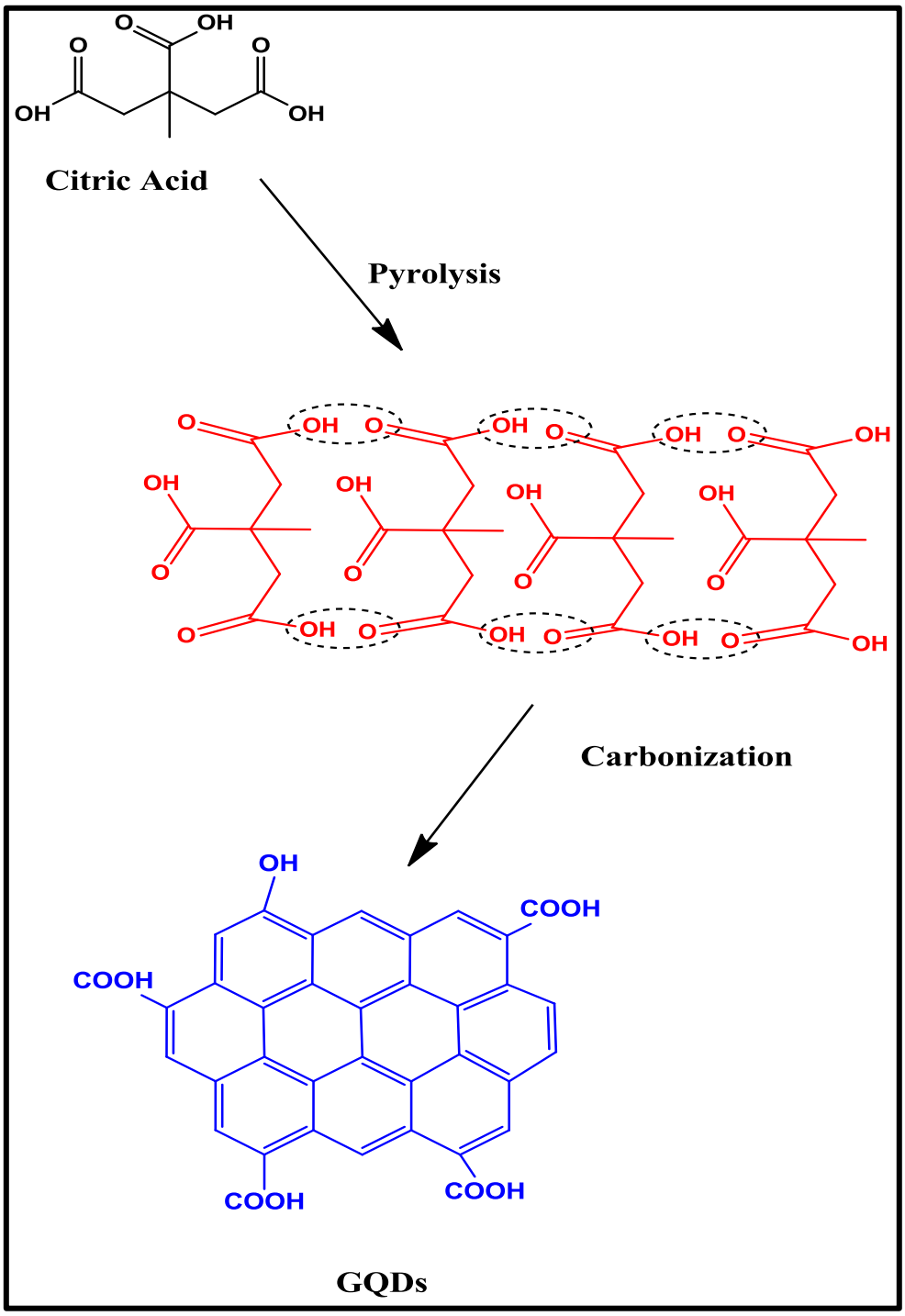

Figure 1.4: Bottom-up synthesis of GQDs via pyrolysis of citric acid [44].

1.2.2.3. *In situ* Doping/Functionalization

The honeycomb lattice of GQDs can allow heteroatoms to penetrate directly into the carbon lattice. This has allowed for modulation of their chemical, optical and electronic properties [**46-48**]. A wide array of organic and inorganic molecules including aryls, amines, thiols and ionic

liquids have been employed in the doping of GQDs [**41, 49-51**]. The introduction of amino and thiol-containing moieties on the GQDs surfaces, allows for further modifications or attachments to other molecules of interest [**52,53**]. These methods, notwithstanding underlying mechanisms are largely unclear, have proven effective for modulating the properties of GQDs. L-glutathione (GSH) was used in this thesis as both the dopant and for surface-functionalization of GQDs (GQDs@GSH). GSH functionality also allows for further modifications and bond formations [**53**]. Moreover, post synthesis modification of the GQDs via π-π interactions with other π-conjugated systems, is also possible owing to their planarity [**54**]. Thus, GSH-functionalized GQDs (GQDs@GSH) were linked to Pcs via π-π stacking and covalent linking to carboxylic acid containing Pcs using the amino groups on GSH.

1.3. Gold and silver nanoparticles (AuNPs and AgNPs)

1.3.1. Synthesis

AuNPs and AgNPs can easily be prepared by the reduction of the respective Au and Ag salts by aqueous citrate solutions [**55**]. They have also been successfully synthesized using oleylamine as both reducing agent and capping agent [**56**]. Oleylamine was employed in this thesis for the synthesis of Au and Ag nanospheres AuNSs and AgNSs, followed by functionalization with L-glutathione (GSH) in order to assist coupling to Pcs and folic acid (FA). The functionalization of Au and Ag nanoparticles with GSH was achieved by taking advantage of the strong affinity of both Au and Ag atoms to sulphur in GSH (**Fig. 1.5**). The synthesis of different shapes of Au nanoparticles is also possible by altering reaction conditions; reagent amounts and reaction times. The seed-mediated method of rod-shaped Au nanoparticles (AuNRs) synthesis has become one of the most widely used. This is largely owing to its relative simplicity and high yields attainable [**57**]. In this two-step protocol, the Au seeds are synthesized by simple reduction of the Au salt by $NaBH_4$. Subsequently, the seed solution is added to a growth solution containing $AgNO_3$ (for shape induction) to allow the growth of Au nanoparticles to rod-like shapes to occur [**58**] (**Scheme 1.3**). In this method, the surfactant, cetyltrimethylammonium bromide (CTAB), is also commonly used to assist growth of the AuNRs. The seed-mediated method was employed in this work in the fabrication of CTAB-capped Au nanospheres and nanorods, and their surface-enhanced Raman scattering (SERS) behaviour was elucidated.

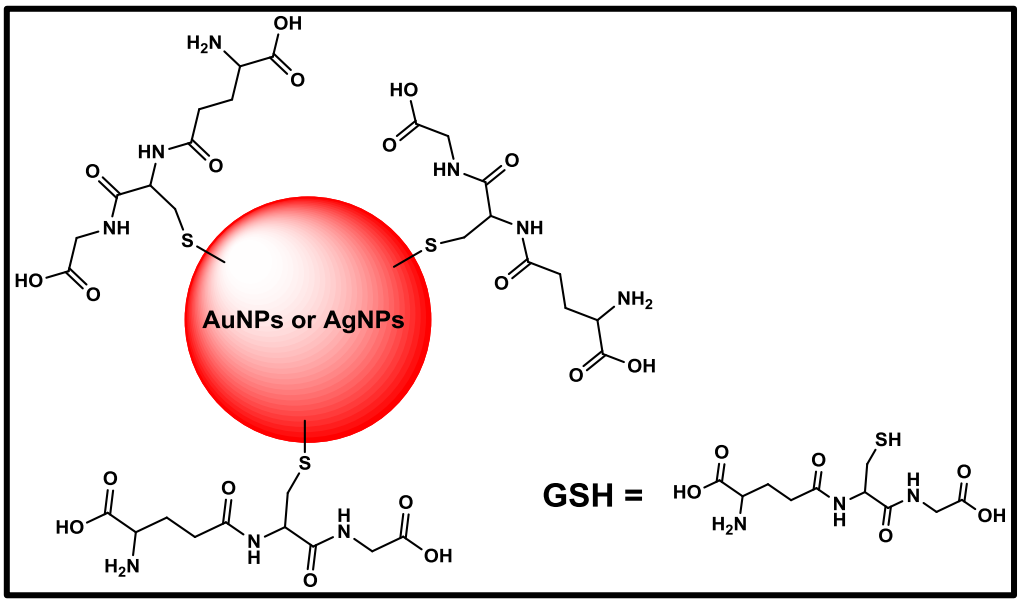

Figure 1.5: Representation of L-glutathione (GSH) functionalized Au and Ag nanoparticles employed in this work.

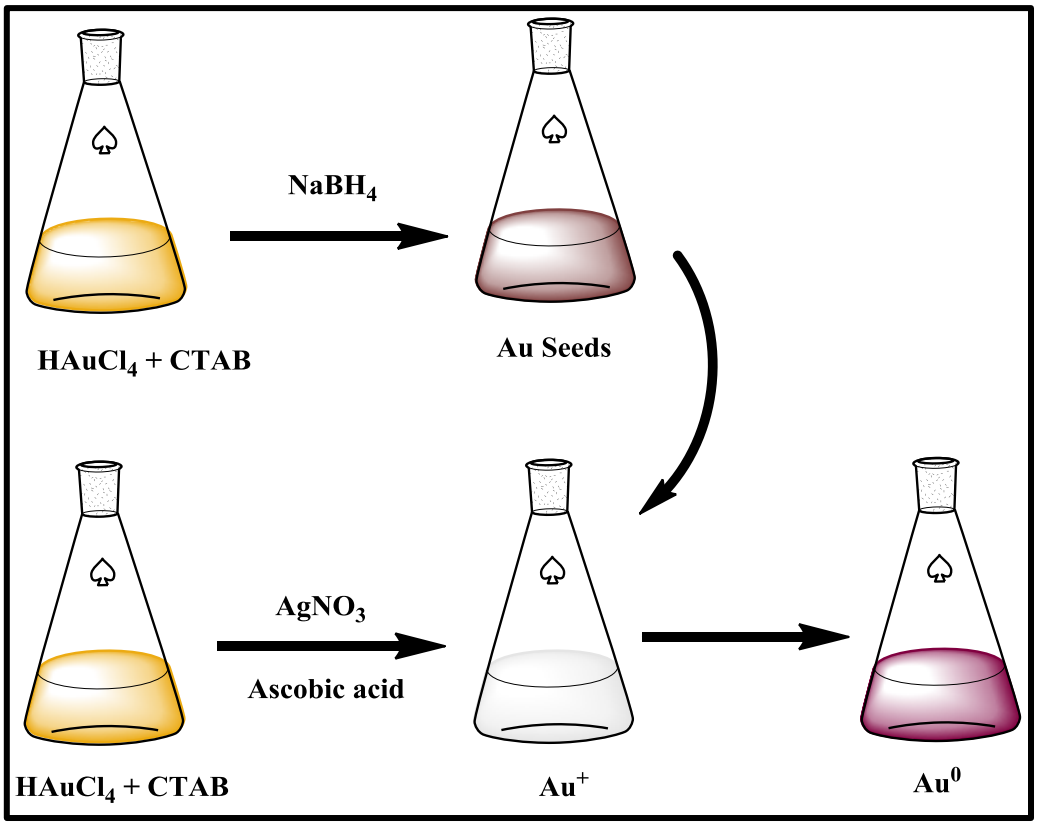

Scheme 1.3: Schematic representation of the seed-mediated growth method.

1.3.2. Optical properties

The UV-Vis spectra of AuNPs and AgNPs are often characterised by a strong absorption band known as surface plasmon resonance (SPR) around 530 nm and 400 nm, respectively [**57**]. For AuNPs, the positions of the SPR are largely dependent on particle shape and size. For example, gold nanorods (AuNRs) usually show two absorption bands; the longitudinal and transverse bands, unlike their spherical counterparts (nanospheres) which only have one SPR band [**57**]. The transverse and longitudinal bands are as a result of electron oscillations along the length and width of the nanorods, respectively [**58-60**]. The intensity of the longitudinal peak is dependent on the concentration and aspect ratio of the nanorods, with aspect ratio being the ratio of the length/width of a nanorod [**57**].

1.4. Folic acid

Pcs, like many drug candidates, often lack selectivity towards cancerous cells, a major drawback that greatly affects drug efficacy. The need for more targeted delivery has spurred recent efforts around the design of biomolecule-based drug delivery systems [**61**]. Among these biomolecules, folic acid (FA) remains one of the most promising epithelial cancer markers, initiating caveolae-mediated endocytosis of potential drug candidates [**62**]. Folic acid, both in its oxidized and reduced folate-form, is a well-known water-soluble vitamin of the B-complex, essential in DNA metabolism [**63**]. Folate receptors (FR) are significantly up-regulated in a number of cancers, including ovarian, breast, lung, renal and colorectal cancer [**64**], as opposed to normal epithelia. Folic acid, characterised by facile conjugation chemistry and lack of immunogenicity, therefore could serve as an active targeting agent for such cancers. These excellent properties have shown promise in the delivery of drugs such as methotrexate (MTX) [**65**] and idebenone [**66**]. This work reports on the photophysicochemical properties of a NPs-folic acid-phthalocyanine conjugates for the first time (using GQDs, Au or Ag nanoparticles), which could couple the properties of phthalocyanines (Pcs) and nanoparticles (NPs) with the targeting potential of FA. In this work GQDs are also linked to boron dipyrromethene dyes, hence these dyes are discussed next.

1.5. BODIPY

Boron dipyrromethene (4,4-difluoro-4-bora-3a,4a-diaza-s-indacene) dyes, abbreviated hereafter as BODIPYs, are a class of highly fluorescent dipyrrin complexes [**67, 68**]. They have found uses as tunable laser dyes [**69**], fluorescent indicators [**70**] and as potential photodynamic therapy agents [**71-73**]. Their ever-increasing successful applications in these fields can be attributed to properties such as chemical robustness, high lasing efficiency [**70**], as well as their low dark cellular toxicity, high thermal, and photochemical stability [**69-73**]. The BODIPY core (**Fig. 1.6**) can be considered as a derivative of monomethine cyanine dyes [**68**]. Their highly flexible framework means that appropriate structural modifications to the BODIPY core can be achieved by the attachment of conjugated units to one or both pyrrole fragments at either the α, β or meso positions (**Fig. 1.6**).

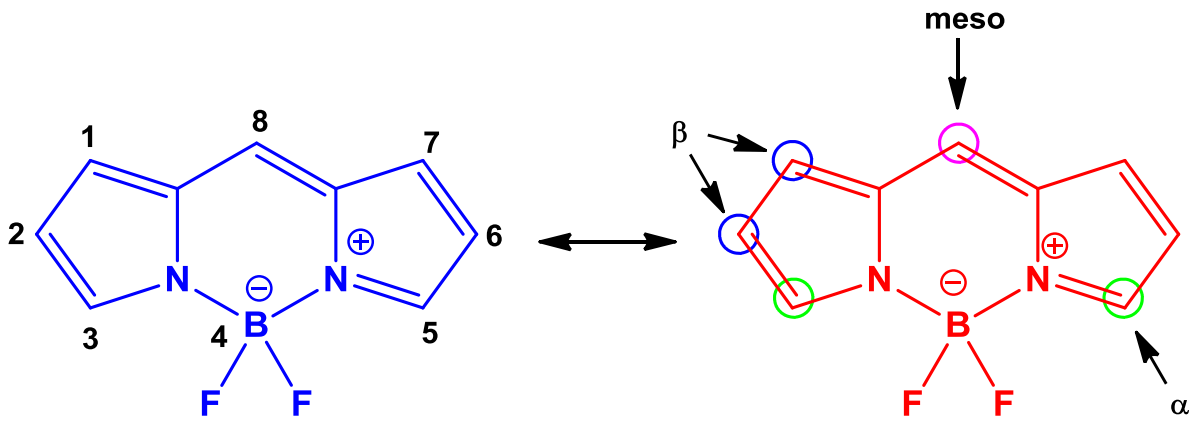

Figure 1.6. The structure of the BODIPY core and its IUPAC numbering system.

1.5.1. Synthesis

The synthesis of BODIPYs is usually through one or two different procedures [**68**]; (a) Lewis acid catalysed condensation between a pyrrole and an aldehyde, followed by oxidation with 2,3-dichloro-5,6-dicyanobenzoquinone (DDQ) or p-chloranil, and subsequent treatment with a suitable base (**Scheme 1.4**), and (b) pyrrole condensation with an acid chloride. In both

procedures trimethylamine or Hunig's base is used. The final step involves the complexation of the synthesized dipyrromethene with boron trifluoride diethyl etherate (BF_3-OEt_2) to yield the BODIPY core. The sensitivity of acid chlorides to moisture often restricts the use of the latter method (b). Accordingly, the condensation of pyrroles with aldehydes is the more commonly utilized synthetic approach [**68,74-75**], and is hence employed in this work (**Scheme 1.4**).

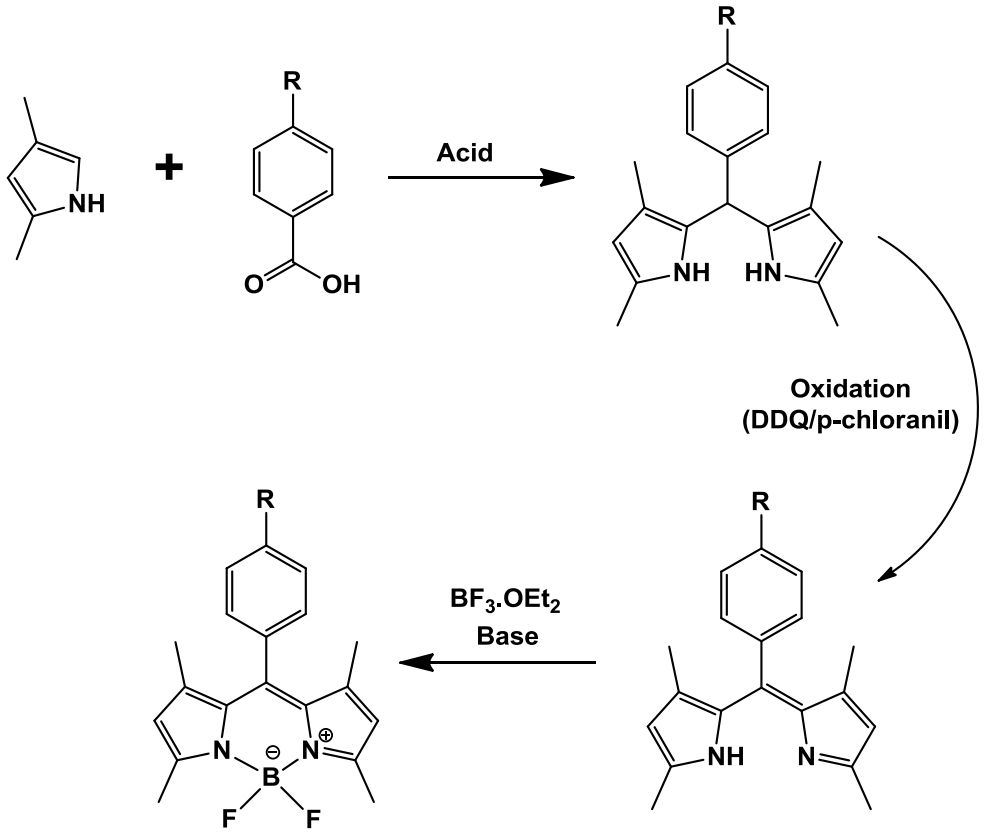

Scheme 1.4. The acid catalysed condensation of aldehyde with pyrrole for the fabrication of a BODIPY core. DDQ = 2,3-dichloro-5,6-dicyanobenzoquinone.

1.5.2. Electronic Spectra

The electronic spectra of BODIPYs is normally characterized by a strong absorption band in the near-UV region and intense fluorescence bands with sharp maxima in the green or red spectral region. This intense band is associated almost entirely with the $S_0 \rightarrow S_1$ ($\pi \rightarrow \pi^*$)

transition [**68,76**] (**Fig. 1.7**). This sharp band is often accompanied by a shoulder, attributed to out-of-plane vibrations of the heterocyclic structure [**76,77**]. An even weaker absorption band which is attributed to the $S_0 \rightarrow S_2$ ($\pi \rightarrow \pi^*$) transition is seen around the 300-400 nm region [**68,76**] (**Fig. 1.7**).

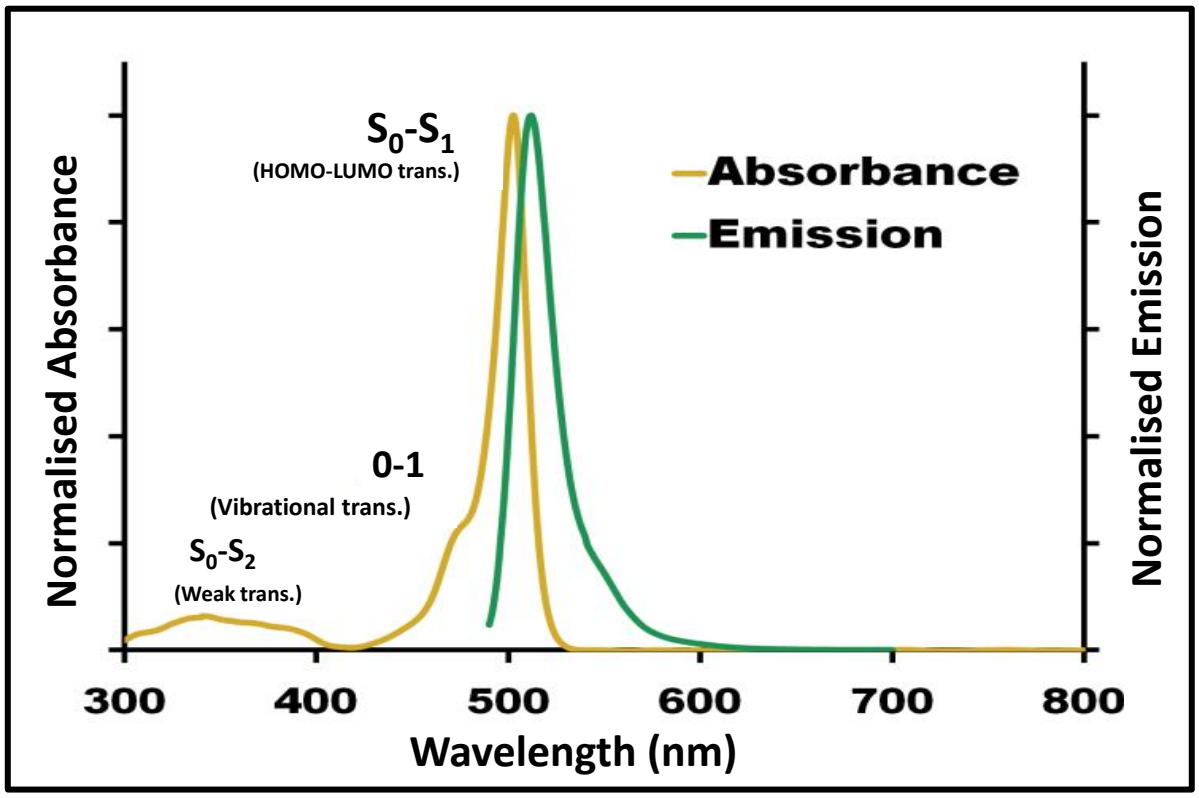

Figure 1.7: Typical absorption (yellow) and emission (green) spectra of a BODIPY dye [Unpublished work].

1.6. Conjugates of Pcs with GQDs, AuNPs/AgNPs, FA or BODIPY.

Table 1.1 [**78-84**] shows that studies on phthalocyanine-GQDs conjugates are limited. Moreover, studies of such complexes only focused on the development of sensors with only one example of photophysical study, a subject of this thesis. The study of MPcs/GQDs hybrids therefore presents an opportunity for exploration of ability of GQDs to affect Pcs properties, and could result in a new class of PDT agents with properties superior to previous Pcs-based

photosensitizers. The GQDs are employed as both pristine GQDs, and tuned by introducing GSH (GQDs@GSH). The GQDs and Pcs conjugates are either π-π stacked or covalently linked.

Au and Ag nanoparticles as well as folic acid have been individually conjugated to Pcs, and have been applied in PDT or photophysical studies (**Table 1.2**) [**85-96**]. This work, for the first time, reports on the photophysical properties of hybrids containing Pcs and FA and either AuNPs, AgNPs or GQDs. These possible new generation MPcs-nanoparticle-FA composites (with either GQDs, Au or Ag nanoparticles conjugated to MPcs and FA (in tandem), could exploit the synergistic properties of phthalocyanines (Pcs) and nanoparticles (NPs) and the targeting potential of folic acid and so pose an important study.

There are many individual examples of BODIPYs and phthalocyanines, but only few hybrid structures have been reported [**97-99]** (**Table 1.3**). This work reports on BODIPY-GQDs conjugates for the first time and subsequently aimed to fabricate a supramolecular hybrid of BODIPY, Pcs and GQDs. Such conjugates (containing BODIPY, GQDs and Pcs) do not exist and could potentially exploit the synergistic properties of the three constituents, which have been individually employed in PDT. This work also reports on the photophysical and surface enhanced Raman scattering (SERS) properties of Pcs/GQDs/AuNPs hybrids, as well as the effect of shape and aspect ratio of AuNPs on their SERS ability for the first time using GQDs as probes.

Table 1.1: Examples of conjugates of Pcs and GQDs for different applications.

Pcs	Nanoparticles	Studies	Ref
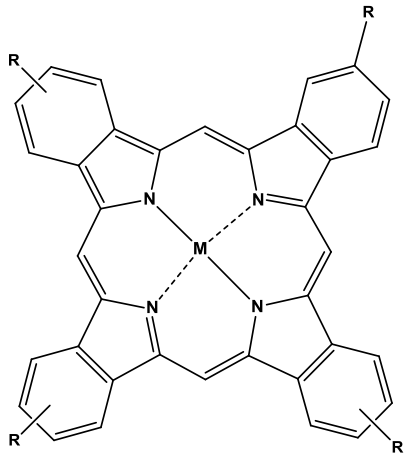 R = 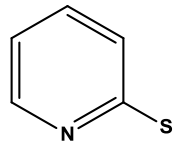 M = Zn	GQDs PEI-GQDs	Hg ion sensing Dual sensing of Hg ion and biothiols	[**78**]
R = 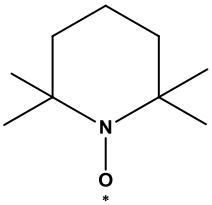 M = Zn	GQDs	Ascorbic acid sensing	[**79**]
R = 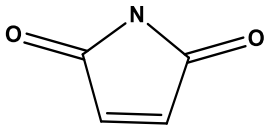 M = Zn	GQDs	Biothiols sensing	[**80**]

R = 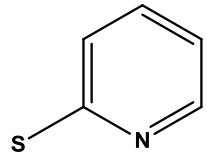 M = Zinc	GQDs	Hg ion sensing	[**81**]
R = 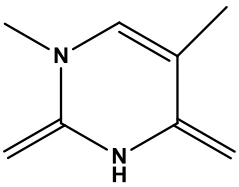 M = Zinc	GQDs	Hg ion sensing	[**82**]
R = 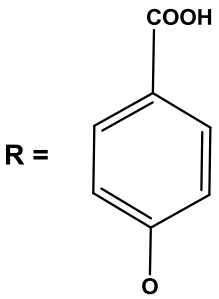 M = Zn	GQDs	Electrocatalysis of N_2H_4	[**83**]
R = 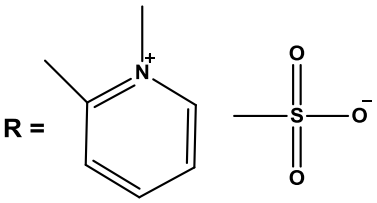 M = Zn	GQDs	Photophysics	[**84**]

Table 1.2: Examples of Pcs and their conjugates with AuNPs/AgNPs or FA with applications.

Pcs	Nanoparticles/Molecule	Studies	Ref
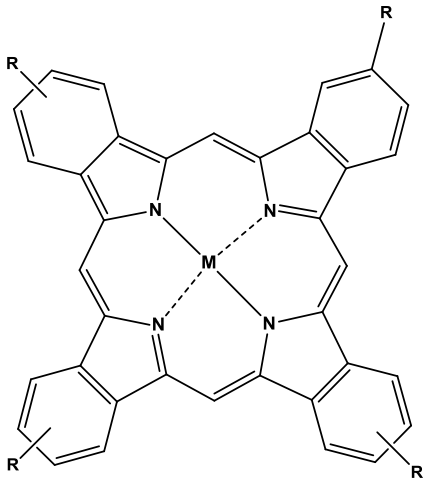 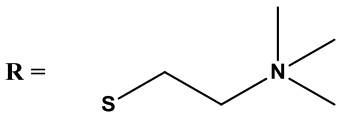 M = Zn	AuNPs	Fluorescence and singlet oxygen studies	[**85**]
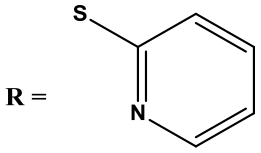 M = Zn	AgNPs	Photophysics	[**86**]
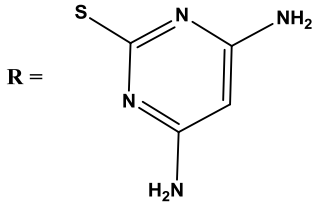 M = Zn	Ag_xAu_y Alloys	Non-linear Optics	[**87**]

R = 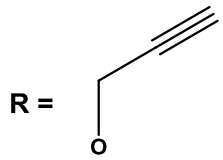 M = InCl, Zn	AuNPs	Non-linear Optics	[**88**]
R = 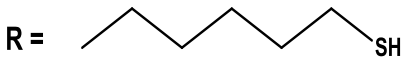 M = Zn	AuNPs	PDT	[**89**]
M = H_2, R = H	AgNPs or AuNPs	Non-linear Optics	[**90**]
R = 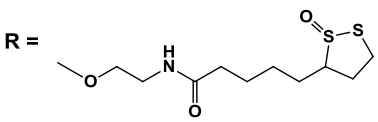 M = Zn	AuNPs	Photophysical	[**91**]
M = Zn, R = NH_2	FA	PDT	[**92**]
M = Zn, R = NH_2	FA	Photophysics	[**93**]
R = 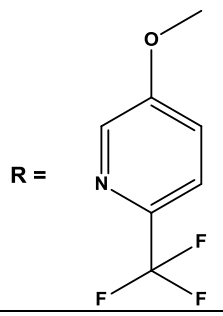	FA	Photophysics	[**94**]

M = Mg, Zn			
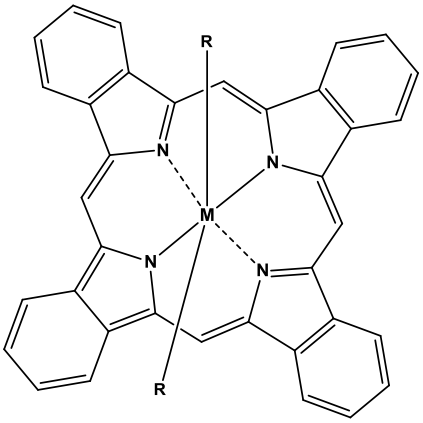 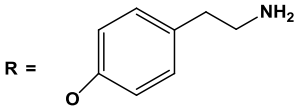 M = $SiCl_2$	FA	PDT	[**95**]
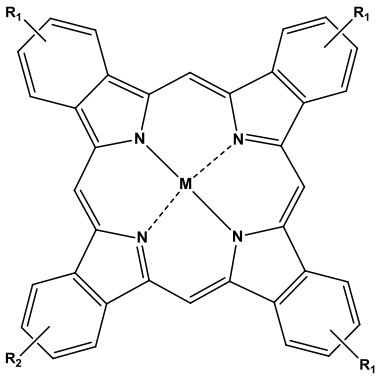 **R_1 = NH_2** 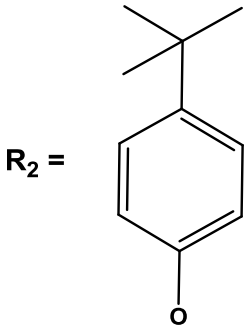 M = Zn	AuNPs	Non-Linear Optics	[**96**]

Table 1.3: Examples of BODIPY-Pcs reported in literature.

Pcs	BODIPYs	Studies	Ref
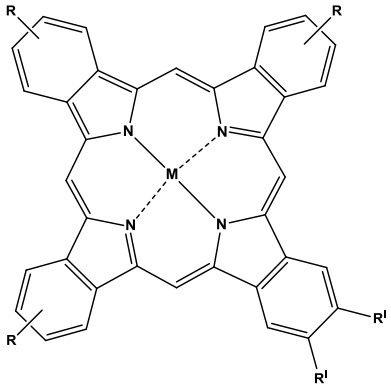 M = Zn, R = Tertiary Butyl, R^I = I	Ethynyl substituted BODIPY	Photophysics	[**97**]
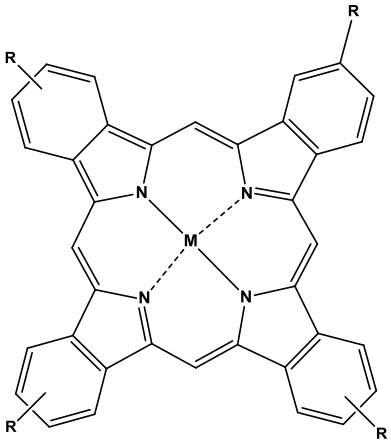 M = Zn, R = I	Ethynyl substituted BODIPY	Photophysics	[**98**]
Zn, R = I	Diethylamino substituted BODIPY	Photophysics	[**99**]

1.7. MPcs and MPcs conjugates used in this thesis

The complexes and conjugates studied in this work are listed in **Table 1.4**. Aluminium-based phthalocyanine [aluminium tetrasulfonated phthalocyanine {ClAlTSPc (**1**)}] [**100**], and the zinc-based phthalocyanines [tris (benzo-thiazole) mono carboxyphenoxy (acetic acid) phthalocyanine {ZnMAPc (**2**)} [**101**], tetrakis (diethylamino) phenoxy phthalocyanine {ZnTAPPc (**3**)} [**102**], and the tris (tert–butyl) mono carboxyphenoxy (propionic acid) phthalocyanine {ZnMPPc (**4**)} were employed in this work. The low symmetry complex (**4**) is reported for the first time in this work. The central metals (zinc and aluminium) were chosen since zinc and aluminium phthalocyanine derivatives have been successfully applied in PDT and more importantly are generally non-toxic metal centres. Benzothiazole was chosen as a Pc ring substituent (**2**) since its derivatives have shown antimicrobial [**103,104**], anti-inflammatory and anti-tumor [**105**] activities. Hence, combining benzothiazole with MPcs may enhance PDT activity. The choice of propionic acid as a substituent (**4**) is based on the fact that porphyrins containing propanoic acid have been employed successfully for PDT [**10**]. The phthalocyanines (**2**) and (**4**), containing only one binding site also present the possibility of specific binding to nanoparticles. The BODIPY (**5**) employed is also reported for the first time in this work, with carboxylic acid substitution to allow covalent linkage to GQDs@GSH.

Table1.4: List of MPcs and MPcs-nanomaterial hybrids employed in this work

Pc/Complex Used	Studies done	Resulting Conjugate
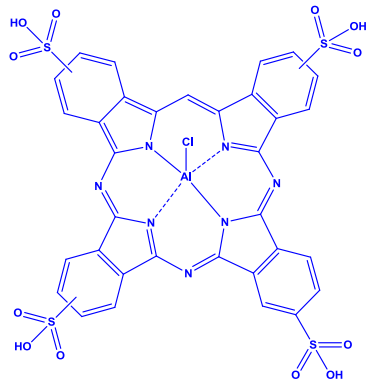 **Aluminium tetrasulfonated Phthalocyanine** {ClAlTSPc (**1**)} [**100**]	Photophysical and photochemical properties	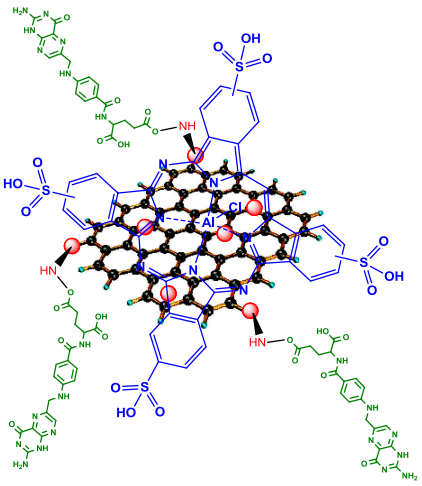 **1** was linked through π-π interactions to GQDs, GQDs@GSH and GQDs@GSH-FA to form **1**-GQDs, **1**-GQDs@GSH and **1**-GQDs@GSH-FA, respectively
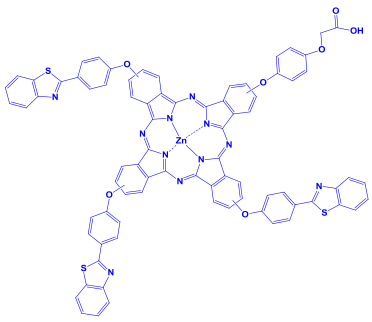 **Zn tris (benzo-thiazole) mono carboxyphenoxy (acetic acid) phthalocyanine** {ZnMAPc (**2**)}[**101**]	Photophysical and photochemical properties	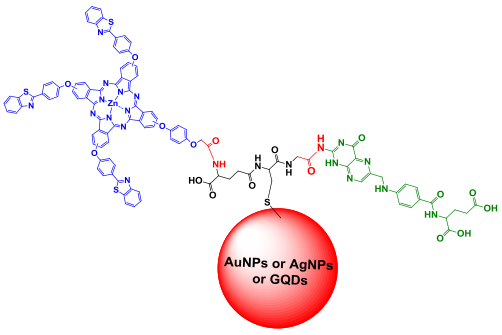 **2** was linked to either GQDs@GSH, AuNSs@GSH or AgNSs@GSH, subsequent to which FA was covalently attached to each conjugate via amide linkage to form **2**-GQDs@GSH-FA, **2**-AuNSs@GSH-FA and **2**-AgNSs@GSH-FA.

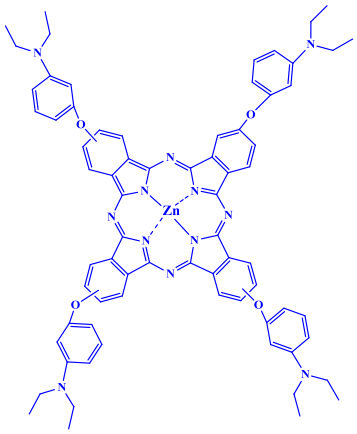 **Zinc tetra (diethylamino) phenoxy phthalocyanine** {ZnTAPPc (**3**)}[**102**]	Photophysical and photochemical properties	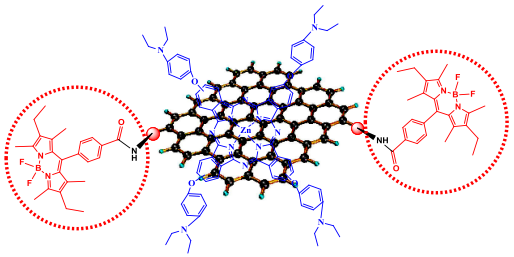 **3** was linked to GQDs@GSH and BODIPY-GQDs@GSH via π-π interactions to form **3**-GQDs@GSH and **3**-BODIPY-GQDs@GSH, respectively.
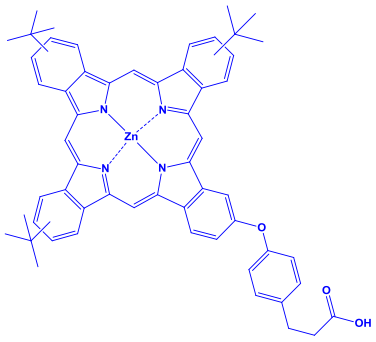 **Zn tris (tert–butyl) mono carboxyphenoxy (propionic acid) phthalocyanine** {ZnMPPc (**4**)} (**New**)	Photophysical and photochemical properties, as well as surface-enhanced Raman scattering behaviour	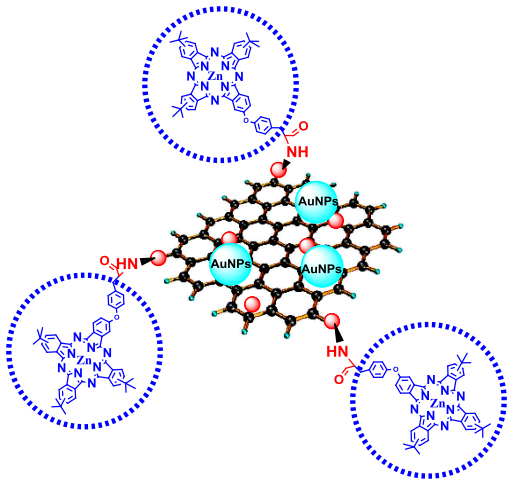 **4** was covalently attached to GQDs@GSH to form **4**-GQDs@GSH. This was followed by in situ synthesis of AuNSs on the **4**-GQDs@GSH to form **4**-GQDs@GSH-AuNSs

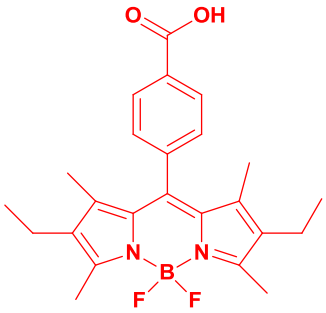 **Carboxylic BODIPY** **{BODIPY (5)}** (New)	Photophysical and photochemical properties	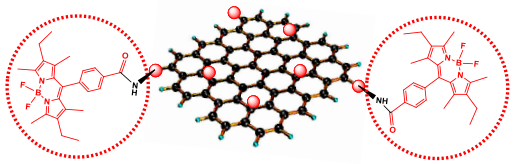

1.8. Photophysical and photochemical properties

Photophysical properties generally describe measured changes within the electronic or quantum states of a molecule upon interaction with light of appropriate wavelength [**106**], and can be explained with a Jablonski diagram (**Fig. 1.8**) [**107**]. They include both radiative processes (fluorescence (F) and phosphorescence (P)) and non-radiative processes (vibrational relaxation (VR) and internal conversion (IC)) [**108**].

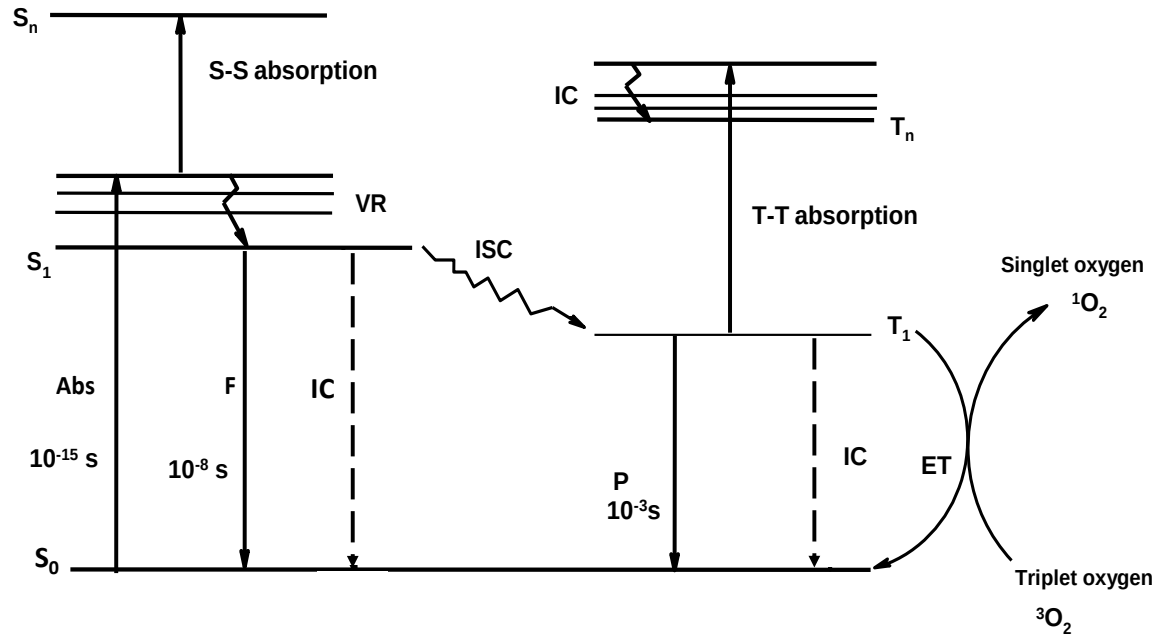

Figure 1.8: A modified Jablonski diagram showing the transition between ground state (S_0) and electronic excited states (S_1 and T_1). Abs = absorption, F = fluorescence, VR = vibrational relaxation, IC = internal conversion ISC = intersystem crossing, P = phosphorescence, T-T absorption = triplet to triplet absorption, S-S = singlet to singlet absorption, S_1 = singlet excited state, T_1 = first triplet state [107].

1.8.1. Fluorescence quantum yield (Φ_F) and lifetime (τ_F)

Fluorescence can simply be defined as a spin allowed transition of a molecule from an excited singlet state to the ground state by emission of a photon [**107**]. Pcs and BODIPYs like many

other fluorophores, fluoresce. Fluorescence quantum yields (Φ_F) and lifetimes (τ_F) are perhaps two of the most important characteristics of any fluorophore and help define their fluorescence efficiency. Fluorescence quantum yield is the measure of the number of fluorescence photons emitted per excitation photon absorbed, while the fluorescence lifetime is average time a molecule spends in its excited state before returning to the ground state through fluorescence. For Pcs, these can be greatly influenced by factors such as; the nature of the central metal, the substituents, temperature, solvent, photo-induced energy transfer (PET) or Forster resonance energy transfer (FRET) amongst others [**109,110**]. Fluorescence quantum yields may be determined using comparative methods [**107**] with a suitable standard, **Equation 1.1**.

$$\Phi_F = \Phi_{F\,(std)} \frac{FA_{std}n}{F_{std}An_{std}} \qquad \textbf{(1.1)}$$

where F and F_{std} are the areas under the fluorescence emission curves of the samples and the employed standard, respectively. A and A_{std} are the respective absorbances of the sample and the standard at the excitation wavelength, and n and n_{std} are the respective refractive indices of solvents used for the sample and the standard. In this study, Φ_F was assessed using unsubstituted ZnPc in DMSO as standard for the MPcs (Φ_F = 0.20) [**11**], quinine sulfate in H_2SO_4 (0.05 M, HCl) (Φ_F = 0.52) [**111**] for the GQDs, and Rhodamine 6G (Φ_F = 0.92) BODIPY employed [**111**].

The fluorescence lifetime for all the complexes studied in this work were determined using the time-correlated single-photon counting (TCSPC) technique.

1.8.2. Triplet quantum yield (Φ_T) and lifetime (τ_T)

An optically excited Pc molecule may either return to its ground state or undergo intersystem crossing (ISC) to its triplet state. The triplet state population is therefore an important parameter in the description of the photophysics of such molecules. Laser flash photolysis is used to study

the triplet properties of molecules, and measures the transient absorption molecules generated by short intense light pulses [**112**]. Triplet quantum yield (Φ_T) can be defined as a measure of the fraction of absorbing molecules that undergo intersystem crossing to the triplet state. The triplet lifetime (τ_T) is the average time a molecule spends at the excited triplet state. Triplet quantum yields and lifetimes are important parameters of Pcs especially in relation to visible light-driven processes such as photosensitization, since the triplet state is a prerequisite for singlet oxygen generation. In this work, the triplet state parameters were determined experimentally using a comparative method [**112**], **Equation 1.2**.

$$\Phi_T = \Phi_{T\,(std)} \frac{\Delta A_T \varepsilon_T^{std}}{\Delta A_T^{std} \varepsilon_T} \quad \textbf{(1.2)}$$

where ΔA_T and ΔA_T^{std} are the changes in the triplet state absorbance of the sample and the standard, respectively. $\Phi_{T\,(std)}$ is the triplet state quantum yield for the unsubstituted ZnPc which was the employed standard in this work ($\Phi_{T\,(std)}$ = 0.65 for ZnPc in DMSO) [**113**]. ε_T and ε_T^{std} are the triplet state extinction coefficients of the sample and the standard, respectively. They were calculated from ground state molar extinction coefficients of the sample and standard, ε_s and ε_s^{std}, respectively, using equation **1.3a** and **1.3b**, respectively.

$$\varepsilon_T = \varepsilon_s \frac{\Delta A_T}{\Delta A_s} \quad \textbf{(1.3a)}$$

$$\varepsilon_T^{std} = \varepsilon_s^{std} \frac{\Delta A_T^{std}}{\Delta A_s^{std}} \quad \textbf{(1.3b)}$$

where ΔA_s and ΔA_s^{std} are the changes in the ground state absorbance of the sample and the standard, respectively. The triplet lifetimes were obtained by fitting the triplet decay curves obtained from laser flash photolysis measurements using OriginPro® 8 software (**Fig. 1.9**).

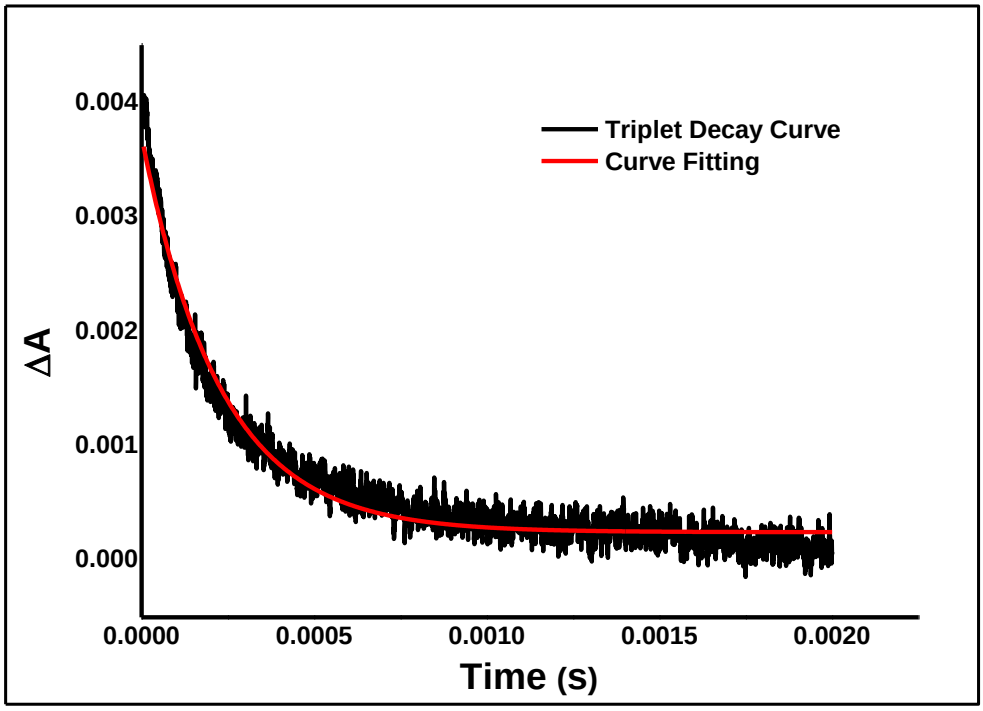

Figure 1.9: Triplet decay curve of a typical MPc in DMSO solution [Unpublished work].

1.8.3. Singlet oxygen quantum yields (Φ_Δ)

Singlet oxygen is a highly reactive cytotoxic oxidative species involved in photo-induced oxidative processes [**114**]. Photosensitized oxidations involving singlet oxygen are implicated in a variety of areas such as photodegradation of dyes and polymers, DNA damage, and is responsible for tumour necrosis in PDT [**115**]. Singlet oxygen is measured by the quantum yield; an important determinant of photosensitizer efficiency. Through energy transfer processes between excited triplet state (T_1) of MPcs (^{3}MPc*) or BODIPY and ground state molecular oxygen, Pcs or BODIPYs are able to produce singlet oxygen. In this manner, ground state triplet oxygen can be excited to singlet oxygen ($^1O_2$) [**114,116**] (**Fig. 1.8**).

Singlet oxygen quantum yields in this work were determined using a comparative photochemical method, requiring the use of chemical scavengers. In this work, the singlet oxygen scavengers, 1,3 diphenylisobenzofuran (DPBF) and Rose Bengal were used. This

method is the most common method for quantifying singlet oxygen in laboratory settings owing mainly to its undeniable simplicity. The values of the Pcs or BODIPY alone and in conjugates were determined using Equation **1.4**.

$$\Phi_{\Delta} = \Phi_{\Delta}^{std} \frac{R\, I_{abs}^{std}}{R^{std} I_{abs}} \quad (\mathbf{1.4})$$

where Φ_{Δ}^{std} is the singlet oxygen quantum yield for the unsubstituted ZnPc which was the employed standard for MPcs (0.67 in DMSO) [**117**], and Rose Bengal (0.76 in DMSO) [**118**] as the standard for the BODIPY. R and R^{std} are the DPBF photobleaching rates in the presence of the sample and the standard, respectively. I_{abs} and I_{abs}^{std} are the rates of light absorption by the sample and the standard, respectively.

1.9. Surface enhanced Raman scattering (SERS)

Accurate photosensitizer dose designs are essential for improved treatment outcomes in photodynamic therapy (PDT), either as an adjunct or alternative therapy modality [**119**]. Although MPcs-nanoparticles conjugates are typically characterized by high triplet quantum yields, they often suffer from very low fluorescence [**120,121**]; an important parameter in conventional PDT dosimetry [**122**]. Various matrices such as the amount of Pcs at the treatment site before and after PDT are monitored by fluorescence and are hence utilized for PDT dose design [**123,124**]. The interplay between fluorescence and intersystem crossing from the excited singlet state, which must be carefully negotiated in the design of suitable photosensitizers for PDT [**125,126**], coupled with the variability in the optical features of tissues between patients [**127**], consequently necessitate the development of alternative techniques for PDT dosimetry.

Such a technique must possess several key characteristics such as excellent sensitivity and reproducibility. Surface-enhanced Raman scattering (SERS) has emerged as one the most promising alternative [**127**]. SERS, an agglomeration of Raman spectroscopy and nanotechnology, enables identification of a large number of molecules through their characteristic vibrational spectra. Molecular fingerprint specificity is possible in SERS since vibrational states are directly related to molecular structure [**128**]. In SERS, the adsorption of target analytes onto rough metals surfaces results in huge enhancements in Raman signals, which are otherwise very weak.

Noble metals with rough surfaces, such as gold (Au) have been traditionally employed for SERS [**129**]. Such colloidal metal nanostructures give rise to local electromagnetic fields normally referred to as electromagnetic 'hot-spots', which result in significantly enhanced Raman signals [**130**]. Moreover, adsorption of analytes of interest onto metallic surfaces usually results in quenched fluorescence, the consequence of which is high sensitivity and low interference from fluorescence backgrounds; an otherwise major drawback of conventional Raman spectroscopy. Furthermore, Raman scattering is unaffected by its surrounding environment (pH, ionic strength, quenchers, amongst others), the result of which is a more stable and reproducible signal [**131**]. These critical features have encouraged the recent interest in SERS-based PDT dosimetry [**125,131-134**].

GQDs exhibit strong resonance Raman scattering and have several distinctive Raman scattering features which include the radial breathing mode (D-band) and tangential mode (G-band). These are sharp and strong peaks that can be easily distinguished from fluorescence backgrounds and are thus suitable for optical Raman imaging [**135**]. Their Raman features as well as their low cytotoxicity make them ideal Raman-signalling probes, and are hence employed in this work for the first time as hybrid structures with Pcs and AuNPs. Moreover,

the dependence of the SERS of AuNPs on their aspect ratio and shape were simultaneously investigated using GQDs as probe for the first time. This work therefore, reports on the successful fabrication of a novel Pcs/GQDs@GSH/AuNPs supramolecular hybrid. This was achieved via *in situ* synthesis of AuNPs onto GQDs@GSH covalently bound to Pcs. This work envisaged that such hybrid structures, comprising Pcs, GQDs and AuNPs present the possibility of both efficient singlet oxygen generation (owing to the presence of the Pcs) and significant Raman scattering potential (owing to the presence of the GQDs and AuNPs), and so hold potential as novel PDT dosimetric agents.

1.10. Summary of aims of this work

This work is aimed at studying (**i**) the effect of nanomaterials (Au, Ag and GQDs) on photophysical properties of MPcs (the GQDs were conjugated to the MPcs either by a covalent bond or π-π interactions), (**ii**) the effect of pristine GQDs and BODIPY-functionalized GQDs on the photophysical properties of MPcs, (**iii**) the effect of folic acid as an active cancer biomarker on the photophysical properties of MPcs-NPs complexes, as well as the (**iv**) surface enhanced Raman scattering (SERS) properties of AuNPs-GQDs-MPcs hybrids.

The objectives of the work in this thesis are summarized below:

1. Synthesis, surface functionalization and characterization of GQDs, Au and Ag nanoparticles.
2. Synthesis, spectroscopic and photophysical characterization of aluminium and zinc phthalocyanines.
3. Investigation of the effect of GQDs, Au or Ag nanoparticles on the photophysical and photochemical properties of phthalocyanines.
4. Investigation of the effect of folic acid on the photophysicochemical properties of phthalocyanines conjugated to either GQDs, Au or Ag nanoparticles.
5. Investigation of the effect of Au nanoparticle shape and aspect ratio on their surface-enhanced Raman scattering behaviour.
6. Examination of the photophysicochemical and surface-enhanced Raman scattering properties of GQDs/MPcs/Au nanoparticles supramolecular hybrids.

CHAPTER TWO

EXPERIMENTAL

2. Experimental

This chapter provides information on the materials, instrumentation, experimental procedures as well as the methods of characterization employed for the complexes synthesized and studied in this work.

2.1 Instrumentation

- Shimadzu UV-2550 UV/Vis spectrophotometer was used to record the ground state electronic absorption spectra in the range of 300-800 nm.
- FT-IR spectra were recorded on a Bruker® ALPHA FT-IR spectrometer with universal attenuated total reflectance (ATR) sampling accessory.
- Fluorescence excitation and emission spectral measurements were performed on a Varian Eclipse spectrofluorimeter. For the determination of the fluorescence quantum yield, the absorbance sample solution and the standard were ~0.5 at vibronic-band.
- Fluorescence lifetimes were measured using a time correlated single photon counting (TCSPC) setup (Fluo Time 300, Picoquant GmbH) with a diode laser as an excitation source (LDH-P-670 driven by PDL 800-B, 670 nm, 20 MHz repetition rate, Picoquant GmbH) for the MPcs, and a diode laser (LDH-P-485 with 10 MHz repetition rate, 88 ps pulse width) for GQDs and BODIPY dye. Fluorescence was detected under the magic angle with a peltier cooled photomultiplier tube (PMT) (PMA-C 192-N-M, Picoquant) and integrated electronics (Pico Harp 300E, Picoquant GmbH). A monochromator with a spectral width of about 8 nm was used to select the required emission wavelength band. A scattering Ludox solution (DuPont) was used to measure the response function of the system and had a full width at half maximum (FWHM) of about 280 ps. The wavelength of emission

maxima was used for all luminescence decay curves. Data analysis was executed using the FluoFit software (Picoquant), with estimated decay error times carried out using the support plane approach.

- A Bruker Vertex 70-Ram II Raman spectrometer (equipped with a 1064 nm Nd: YAG laser and liquid nitrogen cooled germanium detector) was used for all Raman spectral measurements.
- X-ray powder diffraction (XRD) patterns were recorded on a Bruker D8 Discover equipped with a Lynx-Eye Detector, using Cu Ka radiation (=1.5405 Å, nickel filter) in the range from $2\theta = 10^{o}$ to 100^{o}, and scanning rate of $1° \text{ min}^{-1}$ with a filter time-constant of 2.5 s per step and a slit width of 6.0 mm. Samples were placed on a zero background silicon wafer slide. Baseline correction was performed on each diffraction pattern by subtracting a spline fitted to the curved background using EVA (evaluation curve fitting) software.
- Transmission electron microscope (TEM) micrographs were obtained using a Zeiss Libra 120 TEM.
- Energy dispersive X-ray spectroscopy (EDS) was done on an INCA PENTA FET coupled to the VAGA TESCAM using 20 kV accelerating voltage.
- Dynamic light scattering (DLS) experiments were done on a Malvern Zetasizer nanoseries, Nano-ZS90.
- Elemental analyses were carried out on a Vario EL III Micro Cube CHNS Analyser.
- Mass spectral data were collected with a Bruker Auto FLEX III Smartbeam TOF Mass spectrometer. The spectra were acquired using α-cyano-4-hydroxycinnamic acid as the MALDI matrix in positive ion mode.
- Atomic force microscopy (AFM) measurement in tapping mode was carried out with MFP-3D Origin supplied by Asylum research (Oxford instruments company,

USA). Samples for AFM analysis were prepared by drop casting and room temperature drying of the analyte solution on freshly cleaved mica surface.

- ^{1}H and ^{13}C NMR spectra were obtained using a Bruker AVANCE 600 MHz or Bruker® AMX 400 MHz spectrometer.
- A laser flash photolysis system was used for the determination of the decay kinetics. Samples were prepared in deoxygenated DMSO by bubbling with argon for 15 min. The excitation pulses were produced using a tunable laser system consisting of an Nd:YAG laser (355 nm, 135 mJ/4-6 ns) pumping an optical parametric oscillator (OPO, 30 mJ/3-5 ns) with a wavelength range of 420-2300 nm (NT-342B, Ekspla). The detailed procedure of the flash photolysis experiment is as follows; the absorbance of sample solution and the standard were ~1.5 at Q-band. The solution was introduced into a 1 cm path length UV-Visible spectrophotometric cell and deaerated using argon for 15 min. Thereafter, the solution was sealed and illuminated using an appropriate excitation wavelength source (the crossover wavelength of the sample and the standard was utilized as the laser excitation source wavelength). The maximum triplet absorption detection wavelength was determined from the transient curve. The triplet lifetimes were determined by exponential fitting of the kinetic curves using OriginPro 8 software.
- Photo irradiation for singlet oxygen determinations were done using a General Electric Quartz line lamp (300 W). A 600 nm glass cut off filter (Schott) and a water filter were used to filter off ultraviolet and infrared radiations, respectively. An interference filter (Intor, 670 nm with a band width of 40 nm) was additionally placed in the light path before the sample. Light intensities were measured with a POWER MAX5100 (Molelectron detector incorporated) power meter and were found to be 2.97×1016 photons-1 cm^{-2}.

- Hydrothermal synthesis were carried out using a Berghof (Germany) High Pressure Laboratory Reactor (highpreactor) BR-300, V.3.0 equipped with PT-100 temperature and pressure sensors, BTC-300 Temperature regulator and manometer and PTFE lining. The set-up is shown in **Figure 2.1**.

Figure 2.1. Berghof high pressure reactor employed for the hydrothermal synthesis of the GQDs used in this work.

2.2 Materials

2.2.1 General solvents

Dimethyl sulfoxide (DMSO), chloroform, 1-pentanol, thionyl chloride, deuterated (DMSO and acetone), diphenyl ether (DPE), hydrochloric acid and sulphuric acid were obtained from Sigma Aldrich. Absolute ethanol (EtOH), methanol (MeOH), dimethylformamide (DMF), tetrahydrofuran (THF) were obtained from SAARCHEM. Dichloromethane (DCM) was purchased from BM® scientific. All chemicals obtained were of analytical grade and employed directly without further purification. All aqueous solutions and mixtures were prepared using ultra-pure water obtained from a Mili-Q Water system (Millipore Corp. Bedford, MA, USA).

2.2.2 Nanomaterials preparation and conjugation

Citric acid, dialysis membrane tubing (MWCO 1.5kDa), 1-ethyl-3-(3-dimethylaminopropyl)-carbodiimide (EDC), N-hydroxysuccinimide (NHS), gold(III) chloride hydrate ($HAuCl_4.3H_2O$) 99.9%, l-glutathione (GSH), silver acetate, oleic acid (OA), oleylamine (OLA), N,N′-dicyclohexylcarbodiimide (DCC), potassium hydroxide pellets, cetyltrimethylammonium bromide (CTAB), silver nitrate, folic acid and ascorbic acid were obtained from Sigma-Aldrich.

2.2.3 Reagents for MPcs and BODIPY synthesis and photophysicochemical studies

Zinc acetate, 1,8-diazabicyclo [5.4.0]undec-7-ene (DBU), 4-*tert*butylphthalonitrile, unsubstituted zinc phthalocyanine (ZnPc), rhodamine 6G, 1,3-diphenylisobenzofuran (DPBF), quinine sulfate, 2,4-dimethyl-3-ethylpyrrole, 4-formylbenzoic acid, Rhodamine 6G, tetrachloro-1,4-benzoquinone (p-chloranil), trifloroacetic acid (TFA), boron trifluoride diethyl etherate ($BF_3.OEt_2$), magnesium sulphate, rose bengal, and trimethylamine were purchased from Sigma-Aldrich. Column chromatography was performed using silica gel. The synthesis

of 3(4-phenoxy)-propanoic acid) phthalonitrile was as reported in literature [**136**]. The employed phthalocyanines; aluminium tetrasulfonated phthalocyanine, zinc tris (benzo-thiazole) mono carboxyphenoxy (acetic acid) phthalocyanine, zinc tetra (diethylamino) phenoxy phthalocyanine were synthesized according to reported methods [**100-102**].

2.3 Synthesis of nanoparticles (NPs)

2.3.1 GQDs

2.3.1.1 Pristine GQDs

Pristine GQDs were synthesized following bottom-up methods discussed in the literature [**137**], but with some modifications as follows; citric acid (4.1 g, 21 mmol) and NaOH (2.2 g, 55 mmol) were dissolved in 100 mL water, and stirred to form a clear solution. The solution was then transferred to a 400 mL teflon-lined hydrothermal reactor (**Fig. 2.1)** with subsequent heating to 160 ^{0}C for 4 h. The final product was precipitated and centrifuged at 5000 rpm for 15 min. The solid was re-dispersed in water and dialyzed for two days using a dialysis membrane (MW 1.5 kDa) to remove excess salts. The final product is denoted GQDs.

2.3.1.2 L-glutathione (GSH) functionalized GQDs (GQDs@GSH)

The preparation of GQDs@GSH is according to reported methods [**53**], with slight modifications. Briefly, 0.6 g (3.1 mmol) of citric acid was first mixed with 0.21 g (69.7 mmol) of L-glutathione, and then the mixture was placed in a 5-mL beaker and heated to 240 °C using a heating mantle. About 2 min later, the mixture began to melt and fuse. Subsequently, the colour of the liquid changed from colourless to pale yellow and then brown in 10 min. The resulting liquid was then dissolved in Milli-Q ultrapure water. The resultant GQDs@GSH solution was purified by silica gel column chromatography with 0.01 M HCl solution as the developing solvent. The purified GQDs@GSH solution was stored in the dark at room temperature.

2.3.1.3 GQDs@GSH-FA (Scheme 3.1)

Conjugation of folic acid to GQDs@GSH to form GQDs@GSH-FA was achieved as follows; a mixture of folic acid (0.014 g, 0.031 mmol) and EDC (0.019 g, 0.092 mmol) in 8 mL of water was stirred in the dark for 2 h. Then, GQDs@GSH (5 mg) and NHS (7.24 g, 0.064 mol) were added to the reaction mixture. The reaction was further stirred in the dark at room temperature for 24 h. The product (GQDs@GSH-FA) was extracted with ethyl acetate, dried and purified by repetitive dissolution in DMSO.

2.3.2 AuNPs and AgNPs

2.3.2.1 L-glutathione capped AgNSs/AuNSs, Scheme 3.2.

The GSH capped AuNSs and AgNSs (AuNS@GSH and AgNSs@GSH) were synthesized as reported in the literature [**136-141**] with modifications as follows; silver acetate (0.19 g, 1.13 mmol) or gold (III) chloride trihydrate (0.15 g, 0.37 mmol) were individually weighed into round bottom flasks containing diphenyl ether (DPE) (20.0 g, 118 mmol), oleylamine (OLA, 10 mL) and oleic acid (OA, 5 mL). The reaction mixtures were refluxed at 160 °C with constant stirring and maintained under nitrogen flow for 5 h followed by cooling to ambient temperature. The products were successively purified with ethanol, dried in an enclosed fume hood and are represented as AgNSs and AuNSs, respectively. The formed NPs were each transferred into two separate round bottom flasks containing chloroform (3 mL). A solution containing methanol (20 mL), GSH (0.25 g, 0.81 mmol) and KOH (0.50 g, 8.93 mmol) was added to the NPs mixture. The mixtures were allowed to stir for 2 h at ambient temperature. Afterwards, the formed GSH capped NPs were precipitated out of solution using ethanol, and purified with

methanol. The obtained solid precipitates were air dried in an enclosed fume hood. The nanoparticles are represented as AuNSs@GSH and AgNSs@GSH.

2.3.2.2 CTAB capped AuNPs

First, Au nanospheres (AuNSs) seed solution, was prepared following literature methods [**142**], with slight modifications; an aqueous solution of 2.5×10^{-4} M (5 mL) $HAuCl_4$ was mixed with 10 mL of 0.1 M CTAB solution, and the mixture was stirred for 2 min. Then, 0.6 mL of an ice-cold aqueous solution of 0.01 M $NaBH_4$ was added, and the mixture was shaken by hand at 2 min intervals. The solution was allowed to stand for 2 h and then used for the subsequent synthesis of shaped AuNPs.

For the synthesis of AuNRs, the growth solution (**Fig. 1.3**) was prepared according to literature [**142**] by mixing 77 mL of 9.4 mmol CTAB, 20 mL of 0.09 mmol $HAuCl_4$ and 0.004 M $AgNO_3$. The aspect ratio of the nanorods was adjusted by adding 1 mL of two different amounts of $AgNO_3$; 0.039 mmol and 0.0576 mmol for AuNRs with aspect ratios of 2.0 and 4.0, respectively. To these solutions, 1 mL of 0.105 mmol ascorbic acid was added and the reaction turned colourless. Then the seed solution (0.14 mL) prepared above was added and the mixture was shaken by hand and left undisturbed between 30 and 37 °C for 1 h. A secondary growth solution (5 ml) which composed of ascorbic acid (16.7 mg, 0.09 mmol) was then injected by syringe into the 100 mL stirring gold solutions in the water bath. Gold nanorods were purified by centrifuging for 20 min at 2000 rpm to remove the unreacted gold and spherical gold nanoparticles. The supernatant was removed and the resulting pellet of AuNRs was dissolved in 3 mL of distilled water. The AuNRs of different aspect ratios are represented as AuNRs (2.0) and AuNRs (4.0).

Determination of surface area of CTAB capped AuNPs

Surface area (SA) of a rod may be determined using **Eq. 2.1**.

$$\boldsymbol{SA\ (rod) = \ 2\pi r^2 + 2\pi rl} \qquad \textbf{(2.1)}$$

where r and l are radius and length of a rod respectively. The usual equation ($4\pi r^2$) was employed for the calculation of the surface area of the sphere.

2.3.2.3 Conjugates of GQDs@GSH and CTAB capped AuNPs

An aqueous solution of either CTAB capped (**Fig. 3.1**) AuNS, AuNRs (2.0) or AuNRs (4.0) with concentrations ranging from 1 mg/ml to 6 mg/mL was mixed with GQDs@GSH (1 mg/ml, 3 mL) and stirred for 24 h at room temperature to allow ligand exchange of the CTAB on AuNPs for the GQDs@GSH to take place. The conjugated system was then centrifuged at to obtain the conjugates, represented as complex GQDs@GSH/AuNSs, GQDs@GSH/AuNRs (2.0) and GQDs@GSH/AuNRs (4.0).

2.4 Synthesis of metallophthalocyanines (MPcs) and BODIPY.

Detailed synthetic procedures are not provided for the MPcs employed in this work which have been reported in literature. However, the synthetic methods for the novel low symmetry zinc Pc and BODIPY are presented.

2.4.1 Zn tris–(*tert*–butyl) mono carboxyphenoxy (propionic acid) phthalocyanine (ZnMPPc) (4) (Scheme 3.3)

The synthesis of ZnMPPc (**4**) was as follows; a mixture of 4-*tert*-butyl phthalonitrile (**a**) (0.460 g, 0.0025 mol), 3((4-phenoxy)-propanoic acid) phthalonitrile (**b**) (0.242 g, 0.83 mmol), zinc (II) acetate dihydrate (0.25 g, 1.1 mmol) and DBU (0.3 mL), dissolved in dry 1-pentanol (3

mL) was refluxed at 180 °C with constant stirring, in the presence of nitrogen for 6 h. The product was precipitated out of solution with methanol, followed by purification using silica packed column and a solvent mixture of methanol:THF (1:9) as eluent to give a blue powder. 40 % yield (w/w); UV-Vis (DMSO) λmax/nm (Log Ɛ): 678 (5.42), 611 (4.67), 352 (4.96). MALDI-TOF MS (m/z): calcd 910.39: found 909.86. Anal. $C_{53}H_{48}N_8O_3Zn.4H_2O$: Calc.: C, 64.82; H, 5.74; N, 11.41; Found: C, 63.58; H, 4.46; N, 10.09. FT-IR (ATR): ν (cm^{-1}): 3272 (OH), 3053 (Ar-CH), 2953 (CH), 1719 (C=O), 1478 (Ar-C=N). ^{1}H NMR (600 MHz, DMSO-d_6) δ 9.14 (s, 2H, Ar-H), 7.84 (d, J = 39.2 Hz, 5H, Ar-H), 7.41 – 7.27 (m, 5H, Ar-H), 7.09 (s, 2H), 6.68 (s, 2H, Ar-H), 3.18 (s, 4H, -CH_2), 2.10 (s, 27H, -CH_3).

2.4.2 BODIPY (Scheme 3.4)

The synthesis of the BODIPY dye was carried out according to reported methods [**143**] with slight modifications (**Scheme 3.4**). Firstly, to a solution of 2,4-dimethyl-3-ethylpyrrole (2 g, 16.2 mmol) in dry dichloromethane (100 mL), 4-formylbenzoic acid (1.2 g, 8.1 mmol) was added followed by 3 drops of trifluoro acetic acid (TFA) under N_2. The mixture was stirred for 3 h. The reaction mixture was cooled at 0 ^{o}C while p-chloranil (2.34 g, 9.52 mmol) was added and the stirring continued for 1 h. Triethylamine (10 mL) and boron trifluoride diethyl etherate (10 mL) were added at 0 ^{o}C and the reaction mixture was stirred overnight at room temperature. The crude product was filtered, washed with water (30 × 50 mL) and the organic layer was dried over $MgSO_4$, and then the solvent evaporated. Column chromatography using dichloromethane and ethyl acetate (2:1) with 40 % yield (w/w); UV-Vis (DMSO) λmax/nm (Log Ɛ): 523 (5.11). FT-IR (ATR): ν (cm^{-1}): 3404 (OH), 2963 (CH), 1683 (C=O). Anal. $C_{24}H_{27}NBF_2N_2O_2.2H_2O$: Calc.: C, 62.62.; H, 6.78; N, 6.09; Found: C, 63.32; H, 6.44; N, 7.05. ^{1}H NMR (600 MHz, Acetone) 8.27 (d, 2H, Ar-H), 7.59 (d, 2H, Ar-H), 2.52 (s, 6H, -CH_3), 2.43 – 2.29 (m, 4H, - CH_2), 1.35 (s, 6H, -CH_3), 1.01 (s, 6H, -CH_3) ppm. ^{13}C NMR (151 MHz,

Acetone) 166.18, 153.92, 140.32, 139.56, 138.09, 132.96, 131.17, 130.45, 128.83, 16.56, 13.9, 11.71, 11.13 ppm.

2.4.3 BODIPY and GQDs (Scheme 3.7)

BODIPY decorated GQDs (BODIPY-GQDs@GSH) were prepared as follows; a mixture of as-synthesized BODIPY (20 mg, 0.047 mmol) was dissolved in DMSO (3 ml). Then DCC (0.02 g, 0.098 mmol) and NHS (0.015 g, 0.13 mmol) were added and the resulting solution was stirred for 48 h under gentle stirring in order to activate the carboxylic groups of the BODIPY, following which GQDs@GSH (10 mg) was added and the mixture further stirred for 48 h. The resulting conjugate (BODIPY-GQDs@GSH) was precipitated out from solution with trifluoroacetic acid (TFA) and ice. The precipitate was washed several times with water, centrifuged, and then dried in the fume hood to obtain the BODIPY-GQDs@GSH.

2.5 Pc Linking

A full list of all the conjugates are shown in **Table 3.1.**

2.5.1 General procedure for π-π conjugation

The rich π-electron systems of GQDs and MPcs (complexes **1** and **3** were used as examples), **Scheme 3.5** and **Scheme 3.7**, employed in this work enabled the coordination of MPcs to GQDs via the non-covalent (π-π stacking) method due to the absence of groups for covalent linkages. Adsorption of MPcs to GQDs surface (either as pristine or as modified) was according to methods previously described for the noncovalent (adsorption) of other Pcs to carbon nanomaterials with some modification [**144**]. The conjugates were prepared as follows; GQDs, GQDs@GSH or GQDs@GSH-FA (3 mg each) and **1** (10 mg, 0.011 mmol) were added to 10 mL DMSO and the mixture was ultrasonicated for 4 h, followed by stirring for 4 days. The green Pc turned light green due to adsorption onto functionalized GQDs in each case. The

conjugates were dried under vacuum to obtain a powder form. The conjugates are represented as **1**-GQDs, **1**-GQDs@GSH, and **1**-GQDs@GSH-FA, (**Scheme 3.5**) respectively.

For adsorption of **3** onto GQDs@GSH and BODIPY-GQDs@GSH, the procedure below was followed; 10 mg/ml of GQDs or BODIPY-GQDs@GSH was added to **3** (30 mg, 0.024 mmol), in 5 mL of dry DMF, **Scheme 3.7**. The resulting mixture was ultrasonicated for 4 h, followed by stirring in the dark for 96 h. The resulting conjugate was precipitated out of solution with ethanol to ensure that uncomplexed GQDs@GSH, BODIPY-GQDs@GSH and Pcs were eliminated. The solid products were then dried under vacuum and are represented as **3**-GQDs and **3**-BODIPY-GQDs@GSH.

2.5.2 Covalent Linkages

Complexes **2** and **4** have groups for covalent linkages, and are hence employed.

2.5.2.1 Complex 2 linked to either GQDs@GSH, AuNSs@GSH or AgNSs@GSH, and then to FA (Scheme 3.6)

2-AuNSs and **2**-AgNSs conjugates were synthesized as follows; complex **2** (0.02 g, 0.017 mmol) was dissolved in dry DMF (3 mL). Then DCC (0.01 g, 0.049 mmol) and NHS (0.015 g, 0.13 mmol) were added and the resulting solution was stirred for 48 h. AuNSs@GSH and AgNSs@GSH (0.04 g each) were added after the 48 h had elapsed and the reaction mixture was stirred for a further 48 h at ambient temperature. The resultant nanoconjugates were precipitated out of solution using methanol, centrifuged, washed several times using ethanol, and dried in an enclosed fume hood to form **2**-AuNSs@GSH and **2**-AgNSs@GSH, respectively. **2**-GQDs@GSH were prepared as follows; a mixture of complex **2** (20 mg, 0.26 mmol), EDC (0.025 g, 0.13 mmol), and NHS (0.013 g, 0.11 mmol) in DMSO (3 mL) was stirred at room temperature for 24 h to activate the carboxylic groups, following which

GQDs@GSH (10 mg) was added and the mixture further stirred for 48 h. The resulting conjugate (**2**-GQDs@GSH) was precipitated out from solution with methanol:ethyl acetate (1:1), centrifuged and then dried in the fume hood to get the **2**-GQDs@GSH. Please note: NH_2 group of GSH was used for this conjugation leaving the COOH for further linking to FA discussed below.

2-AuNSs@GSH, **2**-AgNSs@GSH, and **2**-GQDs@GSH (0.02 g each) and DCC (0.035 g, 0.13 mmol) and NHS (0.013 g, 0.11 mmol) were added to 3 ml DMF and stirred for 48 h. The coupling agents were added to activate the carboxylic acid group in the GSH-capped nanoparticles (AuNSs@GSH, AgNSs@GSH, and GQDs@GSH) to allow amide bond formation between the Pc-nanoparticle complexes and folic acid. Folic acid (0.07 g, 0.155 mmol) was added to each conjugate and the reaction mixture was stirred for a further 96 h at ambient temperature. Folic acid-linked conjugates were precipitated and successively purified using methanol, centrifuged and dried. The composites are represented as **2**-GQDs@GSH-FA, **2**-AuNSs@GSH-FA, and **2**-AgNSs@GSH-FA.

2.5.2.2 Complex 4 to GQDs@GSH and AuNSs (Scheme 3.8).

4-GQDs@GSH was synthesized as follows (**Scheme 3.8**); a mixture of complex **4** (20 mg, 0.26 mmol), DCC (0.025 g, 0.12 mmol), and NHS (0.013 g, 0.11 mmol) in DMSO (3 mL) was gently stirred at room temperature for 48 h to activate the carboxylic groups of **4**. GQDs@GSH (10 mg) was then added and the reaction mixture stirred for a further 48 h at ambient temperature. The resultant conjugate (**4**-GQDs@GSH) was precipitated out from solution with trifluoroacetic acid (TFA) and ice. The precipitate was washed several times with water, centrifuged, and then dried in the fume hood to obtain the **4**-GQDs@GSH.

The *in situ* synthesis of the AuNSs on **4**-GQDs@GSH nanoplatform (**4**-GQDs@GSH-AuNSs) was as follows; briefly, to a solution of **4**-GQDs@GSH (20 mg) in 3 mL DMF, $NaBH_4$ (1 mg, 0.053 mol) was added. To this solution $HAuCl_4 \cdot 4H_2O$ (0.12 mmol) was quickly added and the resulting solution stirred vigorously for 2 min. Upon completion, the solution changed from green to light purple and the resulting conjugate began to precipitate out of solution. The precipitate was then repeatedly washed with water, centrifuged and dried in a fume hood to obtain **4**-GQDs@GSH-AuNSs conjugates.

2.6 Raman spectra and SERS measurement.

The 1064 nm laser was employed and operated at a power of 150 mW. An integration time of 100 ms was employed in the Raman spectral measurements. Measurements were performed over select wavenumber ranges of 400 to 4000 cm^{-1}. To appreciate the SERS effect, the enhancement factor (EF) of **4**-GQDs@GSH-AuNSs when compared to GQDs@GSH alone or **4**-GQDs@GSH was quantitatively determined according to **Eq. 2.2** [**145**].

$$EF = \frac{I_{SERS}\, C_{Raman}}{I_{Raman} C_{SERS}} \qquad (2.2)$$

where I_{SERS} represents the Raman spectral intensities of **4**-GQDs@GSH in the presence of AuNPs, while I_{Raman} represents spectral intensities of GQDs@GSH or **4**-GQDs@GSH alone. C_{Raman} is the estimated concentration of the GQDs@GSH alone and C_{SERS} represents estimated concentrations of GQDs@GSH in **4**-GQDs@GSH and **4**-GQDs@GSH-AuNSs. The D-band was chosen as the vibrational mode for calculations of the enhancement factor. The background signal was subtracted from the recorded Raman spectra and the resulting data were individually normalized with respect to the integrated area.

Publications

The results discussed in subsequent chapters comprise of published or submitted material in the following peer reviewed journals. These publications have not been referenced in text.

Nnamdi Nwahara, Jonathan Britton and Tebello Nyokong, Improving singlet oxygen generating abilities of phthalocyanines: aluminum tetrasulfonated phthalocyanine in the presence of graphene quantum dots and folic acid. J. Coord. Chem., 70 (**2017**) 1601-1616.

Nnamdi Nwahara, Njemuwa Nwaji and Tebello Nyokong, Enhanced photophysical parameters of folate-targeted phthalocyanine-nanoparticles composites as potential drug delivery nanosystems, J. Photochem. Photobiol. A: Chem., (**2018**) **Submitted**.

Nnamdi Nwahara, Reitumetse Nkhahle, Bokolombe P. Ngoy, John Mack and Tebello Nyokong, Synthesis and Photophysical properties of BODIPY-decorated Graphene Quantum Dots-Phthalocyanines conjugates, New J. Chem., 42 (**2018**) 6051-6061

Nnamdi Nwahara, Ojodomo Achadu and Tebello Nyokong, *In-situ* synthesis of gold nanoparticles on graphene quantum dots-phthalocyanine nanoplatforms: First description of the photophysical and surface enhanced Raman scattering behaviour, J. Photochem. Photobiol. A: Chem., 359 (**2018**) 131-144.

Nnamdi Nwahara, Munyaradzi Shumba, Ojodomo Achadu, Marcel Louzada, Samson Khene, Jonathan Britton and Tebello Nyokong, New insights into the surface-enhanced Raman spectroscopy Au nanoparticles of different aspect ratios using graphene quantum dots as probe molecules (**2018**) **In preparation**.

Extra publications not directly related to thesis:

Rodica Mariana Ion, Tebello Nyokong, **Nnamdi Nwahara**, Ioana-Raluca, Suica-Bunghez, Lorena Iancu, Sofia Teodorescu, Ioana Daniela Dulama, Raluca Maria Stirbescu, Anca Gheboianu, Wood preservation with gold hydroxyapatite system, J. Heritage Science, (**2018**) **Submitted**.

CHAPTER THREE

SYNTHESIS AND CHARACTERIZATION

This chapter outlines the synthesis and characterization of GQDs, AuNPs, AgNPs, BODIPY, MPcs and their conjugates employed in this thesis.

Only the synthesis of new MPcs, BODIPY or conjugates will be discussed in the following sections. Surface functionalization of the NPs was achieved using CTAB or GSH capping, allowing for utilization of the thiol, amine or carboxylic acid moieties for linkage to Pcs, BODIPY or other NPs.

3.1 Synthesis

3.1.1 GQDs

In this work, pristine GQDs were synthesized using the bottom-up assisted hydrothermal treatment of citric acid (CA) in the presence of sodium hydroxide (NaOH). GQDs@GSH were synthesized using direct pyrolysis of citric acid and GSH. The GQDs@GSH were further linked to FA by taking advantage of the COOH functionality of FA and the NH_2 of the GSH capping on the GQDs, represented as GQDs@GSH-FA (**Scheme 3.1**).

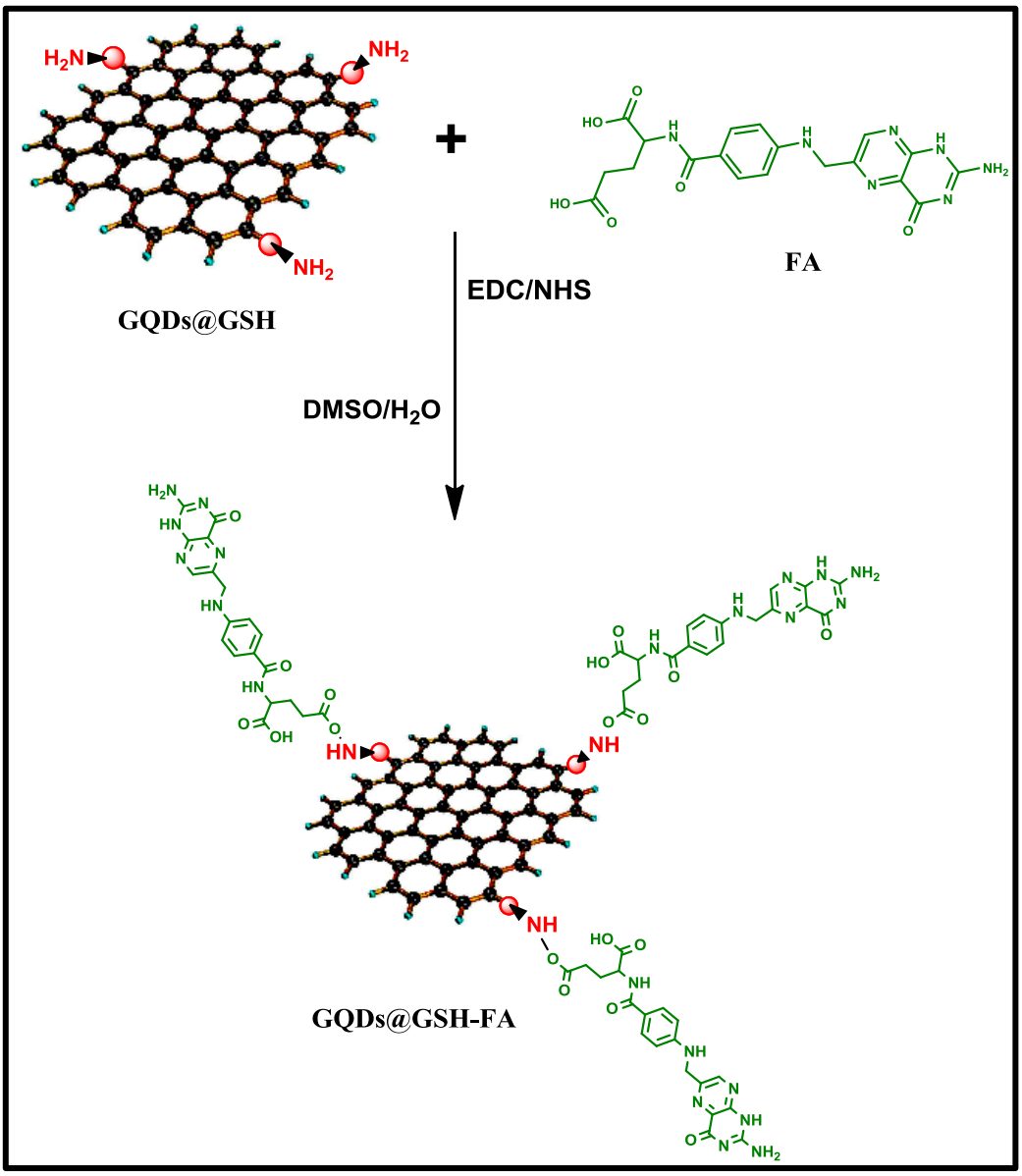

Scheme 3.1: Conjugation of folic acid with GQDs@GSH to form GQDs@GSH-FA

3.1.2 AuNPs and AgNPs

3.1.2.1 GSH-capped AuNSs and AgNSs

The AuNSs and AgNSs used for amide bond linking to complex **2** were synthesised from Au and Ag salts and capped with OLA/OA, which were replaced by GSH to form AuNSs@GSH and AgNSs@GSH, **Scheme 3.2**. The process was achieved by replacement of the OLA/OA capping with glutathione (GSH) due to the stronger affinity of the thiol in the later for the NPs

surface in comparison to the former. It is noteworthy that upon functionalization with GSH, the AuNSs and AgNSs become water soluble. This GSH-functionalization of the nanoparticles was carried out in order to assist the covalent coupling of the nanoparticles to the MPcs and FA.

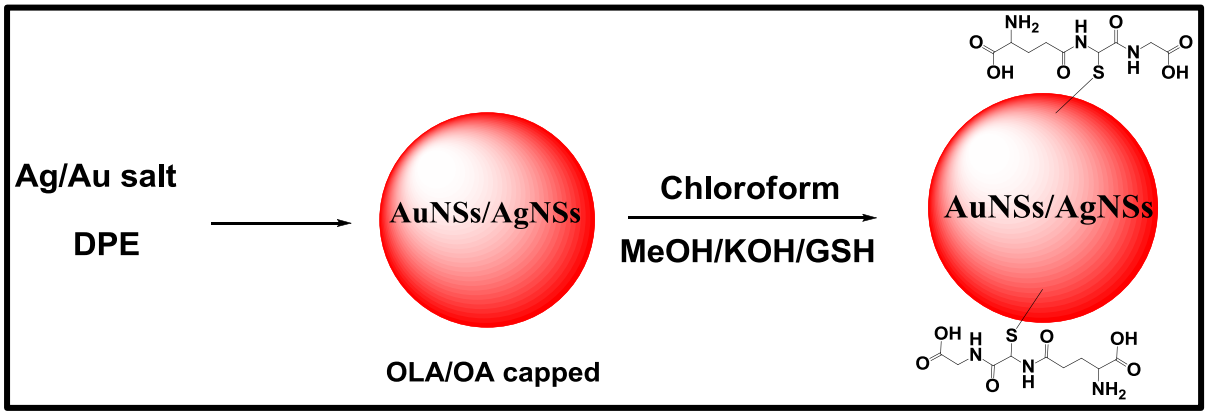

Scheme 3.2: Representation of the synthetic route for the glutathione capped AuNSs@GSH and AgNSs@GSH.

3.1.2.2 CTAB capped AuNPs

CTAB capped AuNPs were used for SERS, hence it is important to note that there were two types of AuNSs capped differently in this work which will be identified by their capping. For the synthesis of AuNRs, AuNSs-CTAB were first synthesised, then converted to AuNRs of two different aspect ratios, AuNRs (2.0) and AuNRs (4.0) in the presence of silver nitrate. Au nanoparticles (AuNPs) of three different aspect ratios (1.0, 2.0 and 4.0, corresponding to AuNSs, AuNRs (2.0) and AuNRs (4.0)) were modified with GQDs@GSH via self-assembly, yielding GQDs@GSH/AuNSs, GQDs@GSH/AuNRs (2.0), and GQDs@GSH/AuNRs (4.0), respectively. This binding was facilitated by ligand exchange where loosely bound cetyl trimethylammonium bromide (CTAB) ligands on the AuNPs are exchanged by the GQDs@GSH. This attachment is facilitated by alkyl-thiol moieties of the glutathione

functionalized GQDs (GQDs@GSH) which provided direct linkage to the nanoparticle surface via self-assembly to the gold surface through the gold-thiolate bond, represented in **Figure 3.1**.

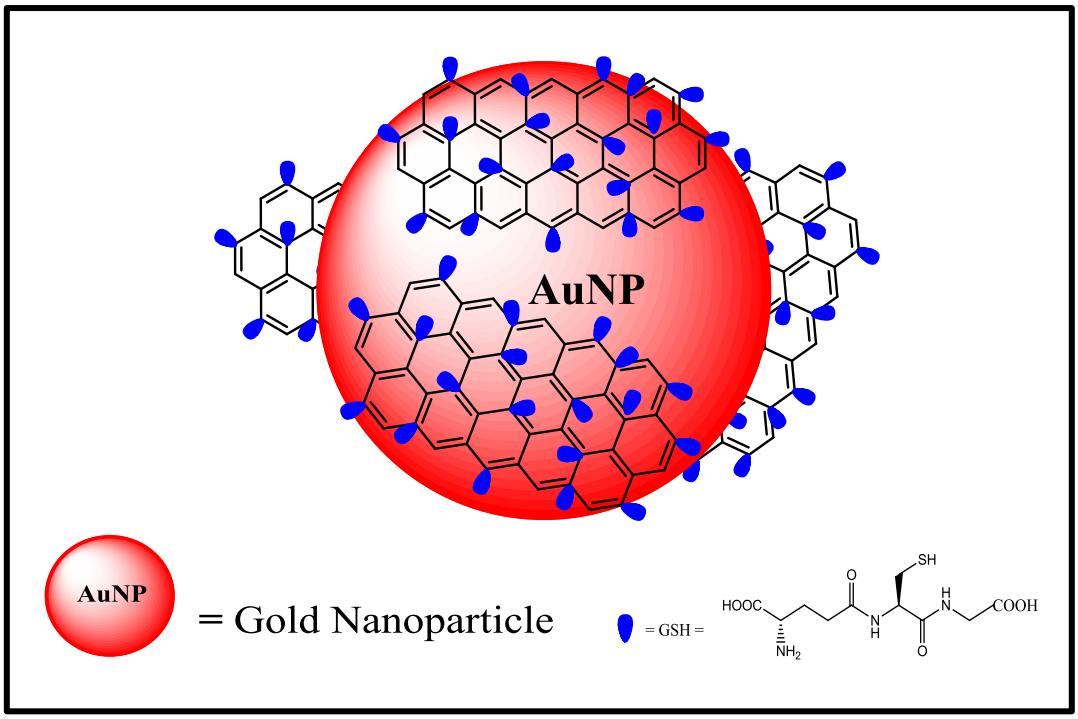

Figure 3.1: Representation of conjugation of GQDs@GSH to AuNPs to form GQDs@GSH/AuNPs via self-assembly.

3.1.3 Pcs/BODIPY

3.1.3.1 Zn tris (tert–butyl) mono carboxyphenoxy (propionic acid) phthalocyanine (4)

The synthesis of compounds **1**, **2** and **3** have been reported elsewhere and will not be discussed in the following subsection. The novel Zn tris (tert–butyl) mono carboxyphenoxy (propionic acid) phthalocyanine {ZnMPPc (**4**)} synthesized in this work will be discussed in detail under this subsection.

Scheme 3.3 shows the synthetic pathway for complex **4**. It involved a cyclotetramerization of the corresponding phthalonitriles (**a** and **b**) in the presence of catalytic DBU, Zn metal salt, and 1-pentanol. Complex **4** was characterized using FT-IR, ^{1}H NMR, MALDI-TOF mass

spectrometry and elemental analysis. The obtained data were consistent with the predicted structure. The compound showed good solubility in most organic solvents. ^{1}H NMR spectrum for complex **4** shows aromatic and aliphatic protons observed between 9.14-6.68 pm and 3.18–2.10 ppm, respectively. Peak integration gave the anticipated total number of protons, confirming the relative purity of the complex. Mass spectral data was in agreement with the proposed structure for complex **4**. For Pc, mass to charge ratio of 910 m/z was expected and obtained. For **4**, FT-IR spectrum confirmed the presence of C=O vibrations at 1719 cm^{-1} and OH vibrations around 3272 cm^{-1}, and C-H vibrations at 3053 and 2953 cm^{-1}.

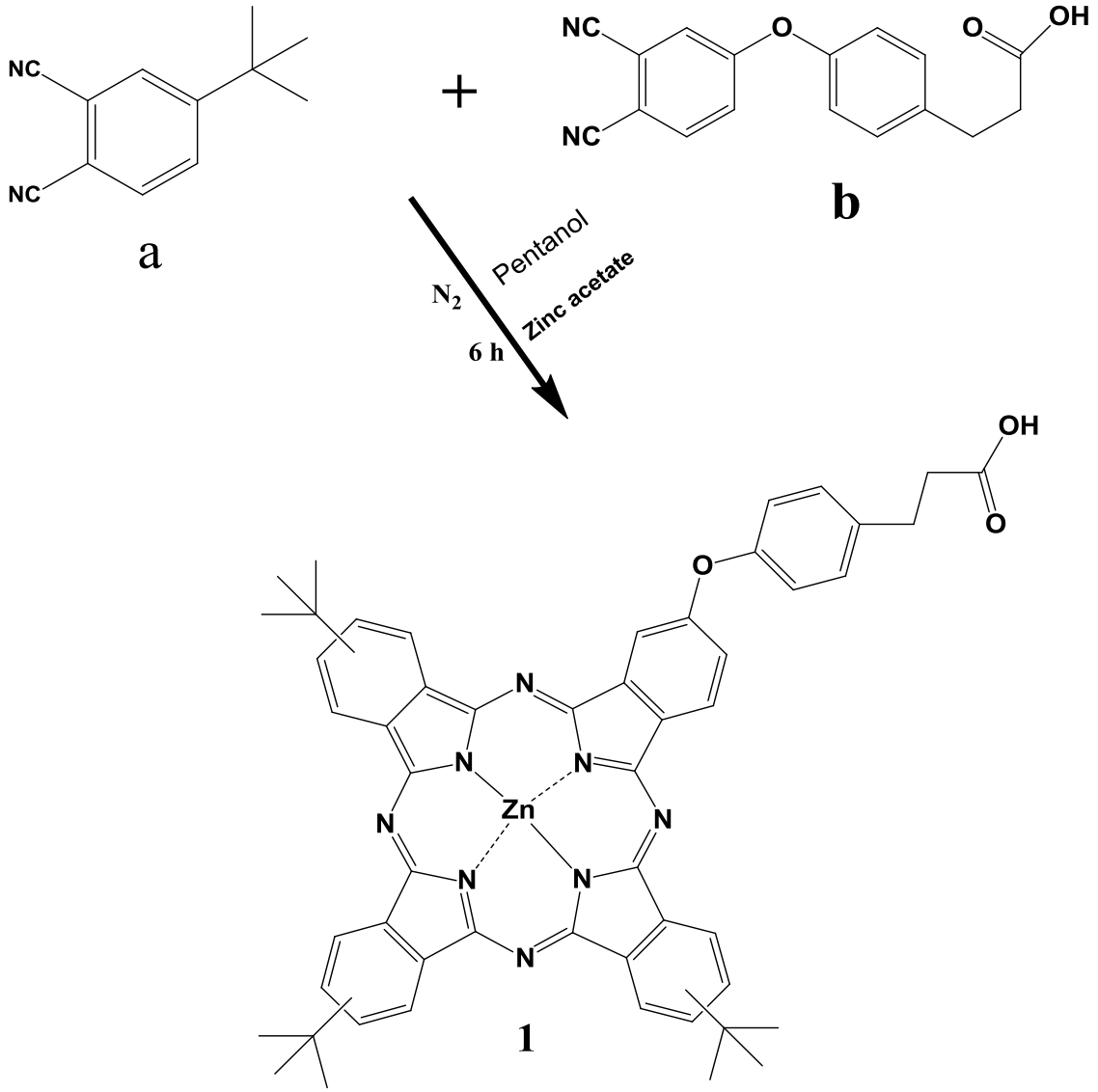

Scheme 3.3. The synthetic pathway for complex 4.

The ground state electronic absorption spectrum of **4** showed monomeric behaviour evidenced by a single (narrow) Q band, typical of metallated phthalocyanines [**22-24**]. The normalized absorption, emission, and excitation spectra of the complex **4**, are shown in **Figure 3.2**. It can be observed that the excitation spectrum was found to be a mirror image of the emission spectrum, and the former was the same as the absorption spectrum with slight changes being due to different types of equipment used. The closeness of maxima of the absorption and excitation spectra, shows that the absorbing species is the same as the emitting one and suggests that the compound does not readily aggregate in solution.

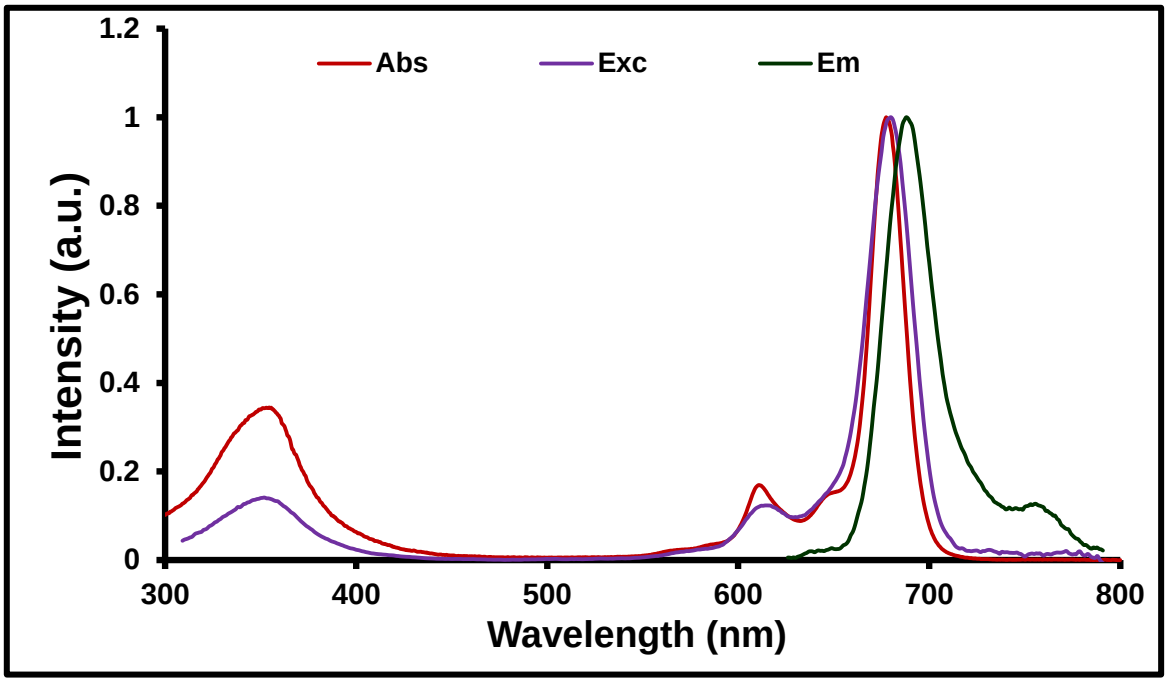

Figure 3.2: Absorption, excitation and emission spectra of complex **4** alone in DMSO.

3.1.3.2 BODIPY

The synthetic route for the carboxylic acid BODIPY is illustrated in **Scheme 3.4**. The synthesis of BODIPY generally involved the condensation of 2,4-dimethyl-3-ethylpyrrole and 4-formylbenzoic acid under reflux in dichloromethane, followed by treatment of the reaction mixture with triethylamine and boron trifluoride diethyl etherate. The structure and purity of the synthesized BODIPY was confirmed by UV–Vis, ^{1}H NMR and ^{13}C NMR.

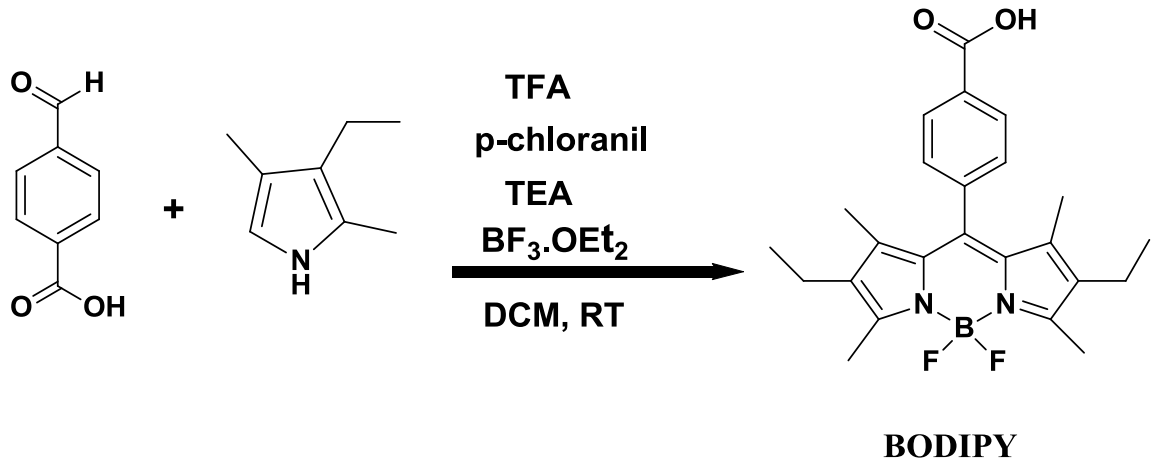

BODIPY

Scheme 3.4: The synthetic procedure for BODIPY dye

The ^{1}H NMR spectrum of **5** depicted aromatic and aliphatic protons between 8.27-7.59 ppm and 2.52–1.01 ppm, respectively. The carbonyl and aromatic carbons were observed between 166 and 128 ppm, and aliphatic carbons between 16-11 ppm in the ^{13}C NMR spectrum. The as-synthesized BODIPY dye exhibits high molar absorption coefficients (~ 129532 M^{-1} cm^{-1}) and hence is a suitable donor molecule due to its high light harvesting properties.

Figure 3.3 shows the normalized absorption, emission, and excitation spectra of the as-synthesized BODIPY (**5**). As can be seen from the figure, the excitation spectrum was found to be a mirror image of the emission spectrum. The closeness of the absorption and excitation spectral maxima shows that the absorbing species is the same as the emitting one, and suggests that the BODIPY does not readily aggregate in solution.

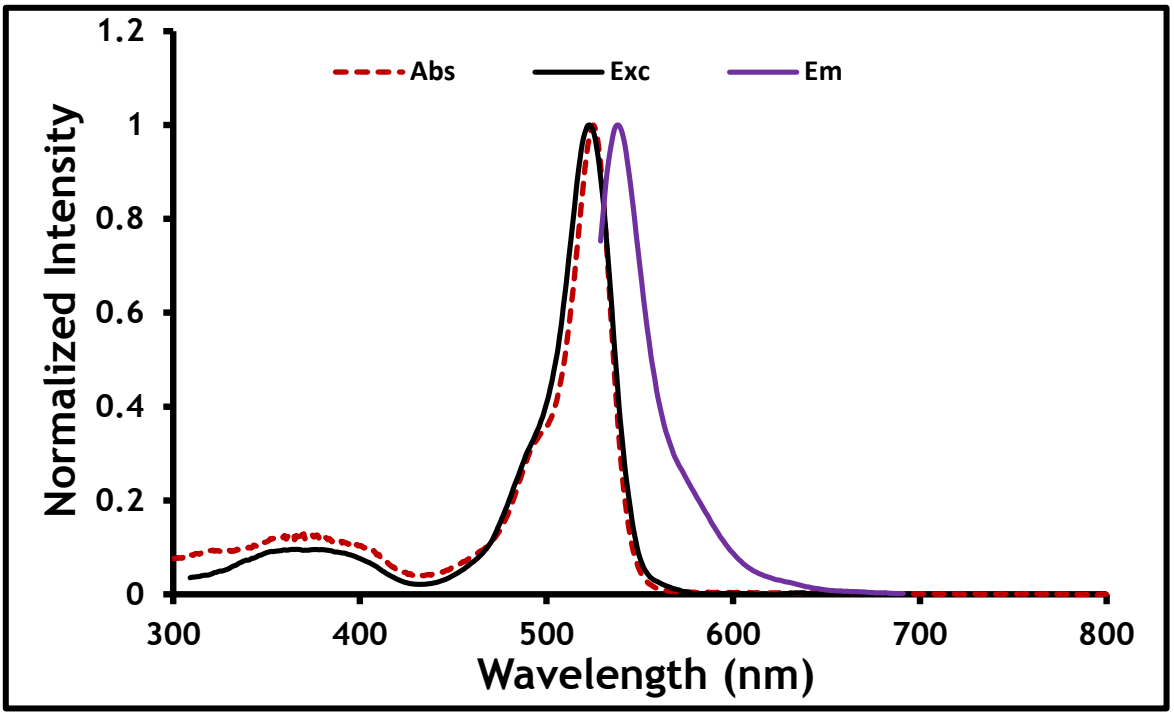

Figure 3.3: Absorption, excitation and emission spectra of BODIPY alone in DMSO.

3.1.4 BODIPY and Metallophthalocyanines –nanoparticle conjugates

The formation of the MPcs-NPs or BODIPY-NPs conjugates via covalent bonding was facilitated by the activation of the carboxylic acid moieties of the MPcs or BODIPY using suitable coupling agents, followed by the addition of amine functionalized NPs (either GQDs@GSH, AuNSs@GSH or AgNSs@GSH), resulting in an amide bond between the respective dye and the NPs. Non-covalent bonding was achieved via π-π interactions owing to the planarity of GQDs, Pcs and BODIPYs. A summary of the conjugates studied in this work is presented below, with a full list of the conjugates in **Table 3.1**.

(i) Compound **1** was conjugated to GQDs, GQDs@GSH and GQDs@GSH-FA via π-π interactions in order to evaluate the effects of the respective GQDs on the photophysicochemical properties of **1** (**Scheme 3.5**).

(ii) Compound **2** was covalently linked to either GQDs@GSH, AuNSs@GSH or AgNSs@GSH and then to FA in tandem. The respective conjugates were

characterized, with subsequent investigation of the photophysical and photochemical properties of the resulting hybrids (**Scheme 3.6**).

(iii) The novel BODIPY (**5**) was covalently linked to GQDs@GSH, with the conjugates further π-stacked to compound **3**. This was compared to a conjugate of **3** and GQDs@GSH alone to study the contribution of the BODIPY as well as with elucidation of the physicochemical properties of the resulting conjugates (**Scheme 3.7**).

(iv) The novel Pc (**4**) was covalently linked to GQDs@GSH, following which AuNPs were synthesized *in situ* on the **4**-GQDs@GSH conjugates. The photophysical and photochemical as well as the Raman scattering properties of the resulting conjugates were evaluated (**Scheme 3.8**).

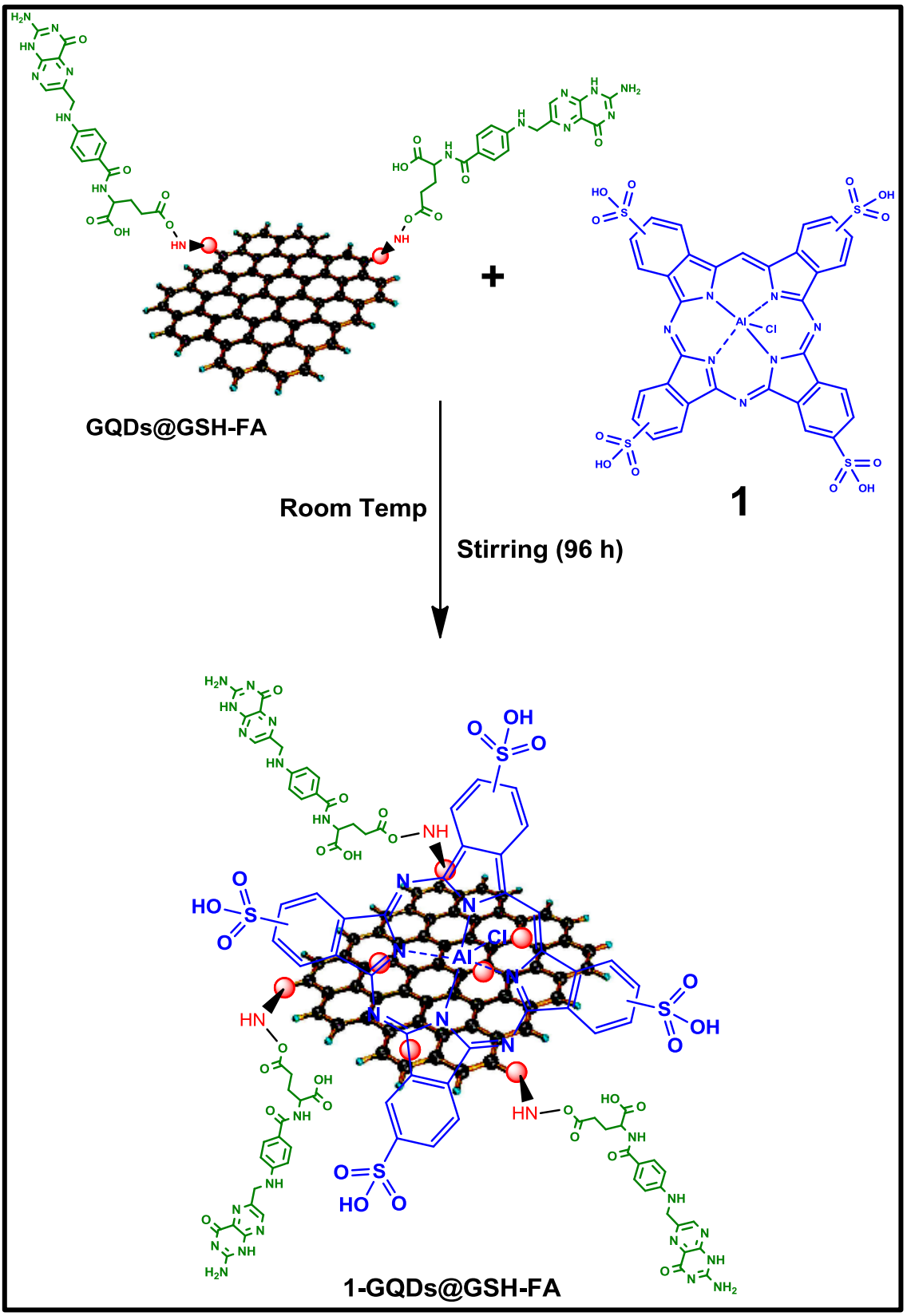

Scheme 3.5: Schematic for the preparation of 1-GQDs@GSH-FA via π-π stacking.

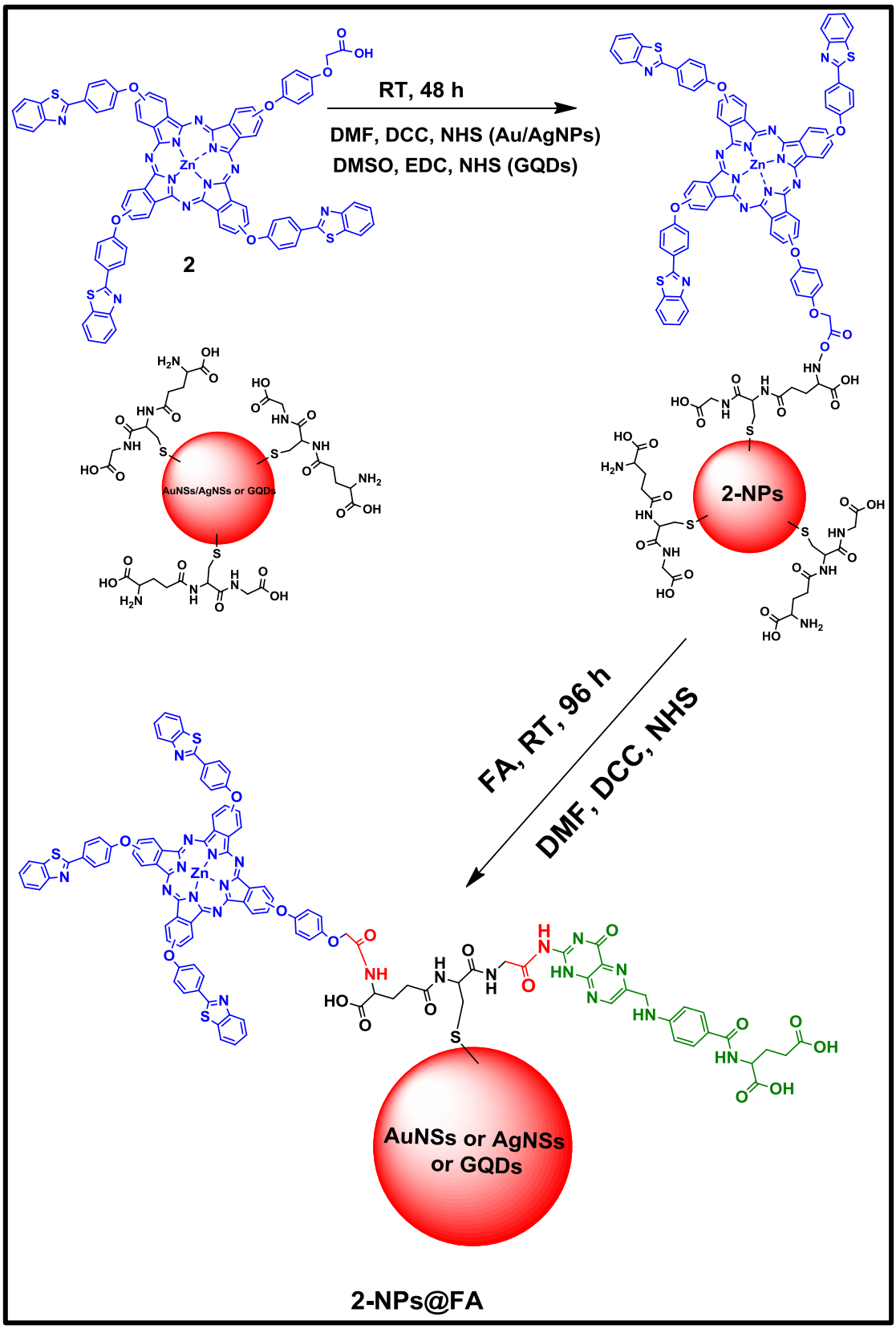

Scheme 3.6: Conjugation of complex 2 to form 2-NPs@FA complexes. (i) DCC/NHS for AgNSs@GSH and AuNSs@GSH, and EDS/NHS for GQDs@GSH, both for 96h at RT.

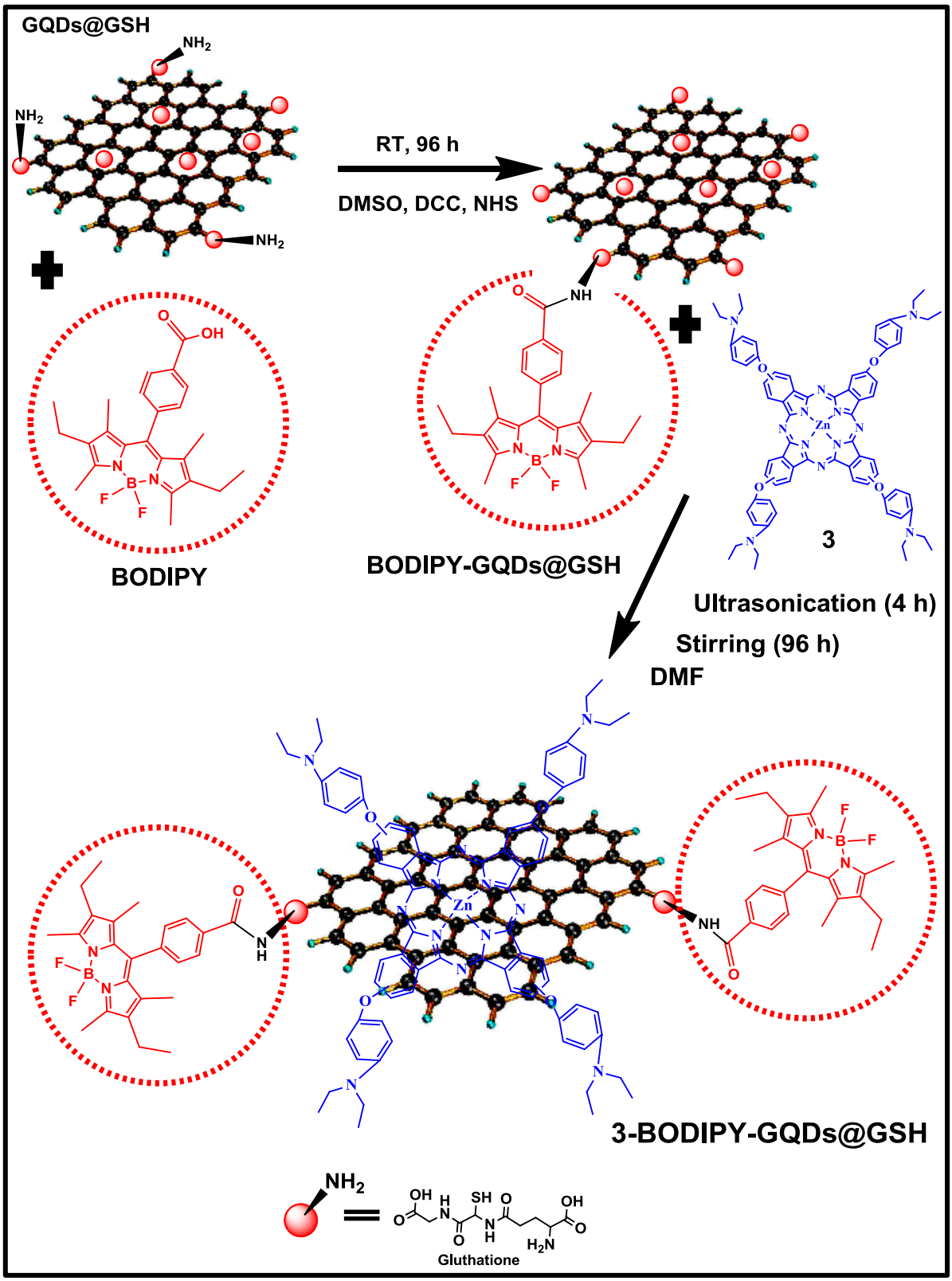

Scheme 3.7: Schematic for the preparation of BODIPY-functionalized graphene quantum dots with illustration of π-π stacking of conjugate and complex 3.

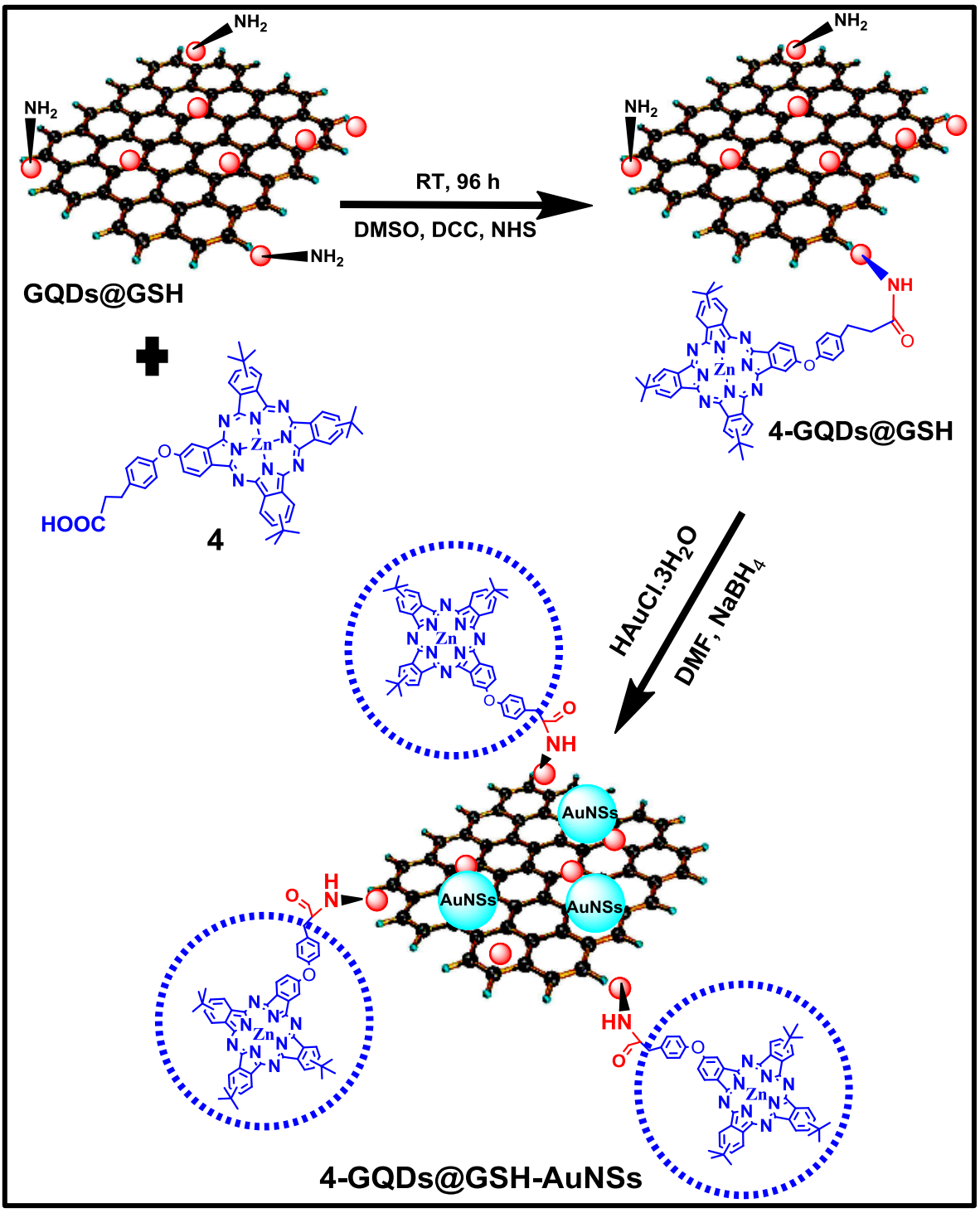

Scheme 3.8: Schematic for the preparation of 4-GQDs@GSH-AuNSs with illustration of covalent interaction of GQDs@GSH and complex 4, and the assembly of AuNSs onto the Pcs/GQDs@GSH surface.

Table 3.1: Q-band of the respective compounds and their corresponding conjugates with BODIPY or Pcs as well as the loading of dyes to respective NPs synthesised in this research work.

Compound/Conjugate	Size (nm) from DLS	λ_{abs} (nm) [a]	Dye-loading (μg Dye/mg NPs)
Nanoparticles below were used for SERS			
AuNSs-CTAB	35	532	-
AuNRs-CTAB	40	532, 664	-
AuNRs-CTAB	50	532, 754	-
GQDs@GSH/AuNSs	40	(332)[a] (532)[b]	-
GQDs@GSH/AuNRs (2.0)	45	(332)[a] (532, 663)[b]	-
GQDs@GSH/AuNRs (4.0)	60	(332)[a] (532, 754)[b]	-
The rest of the nanoparticles were linked to the respective complexes			
GQDs	2	338	-
GQDs@GSH	5.5	332	-
GQDs@GSH-FA	10	330	-
AuNSs@GSH	10.1	531	-
AgNSs@GSH	11.7	416	-
1	-	686	-
1-GQDs	28	686	8
1-GQDs@GSH	35	686	20
1-GQDs@GSH-FA	40	686	16
2	-	680	-
2-AuNSs@GSH	13.5	682 (535)[b]	25
2-AuNSs@GSH-FA	21.1	682	28
2-AgNSs@GSH	16.0	681 (468)[b]	38
2-AgNSs@GSH-FA	19.6	681	45

2-GQDs@GSH	**8.7**	**680**	**15**
2-GQDs@GSH-FA	**10.6**	**680**	**19**
3	**-**	**683**	**-**
3-GQDs@GSH	**21.0**	**682 (332)[a]**	**20**
BODIPY	**-**	**525**	**-**
BODIPY-GQDs@GSH	**8.7**	**526[c] (335)[b]**	**13**
3-BODIPY-GQDs@GSH	**28.2**	**681 (527)[c] (340)[a]**	**26**
4	**-**	**678**	**18**
4-GQDs@GSH	**15.7**	**678 (335)[a]**	**16**
4-GQDs@GSH-AuNSs	**28.2**	**678 (341)[a] (525)[b]**	**18**

Absorption values for [a]GQDs, [b]AuNSs or AgNSs, and [c]BODIPY. AuNSs@GSH and AgNSs@GSH were linked to complex 2.

3.2 Characterization

3.2.1 TEM Images

Figure **3.4** shows the representative TEM images of GQDs@GSH and conjugates with **2**. TEM image of GQDs@GSH shows an overall quasi-spherical morphology and particle size average of about 6 nm. GQDs@GSH was easiest to determine using TEM. Following conjugation of GQDs@GSH to FA there was slight aggregation and sizes could not easily be determined using TEM (**Fig. 3.4**). The same applies to when GQDs@GSH were linked to Pcs **2** and then to FA (**Fig 3.4**).

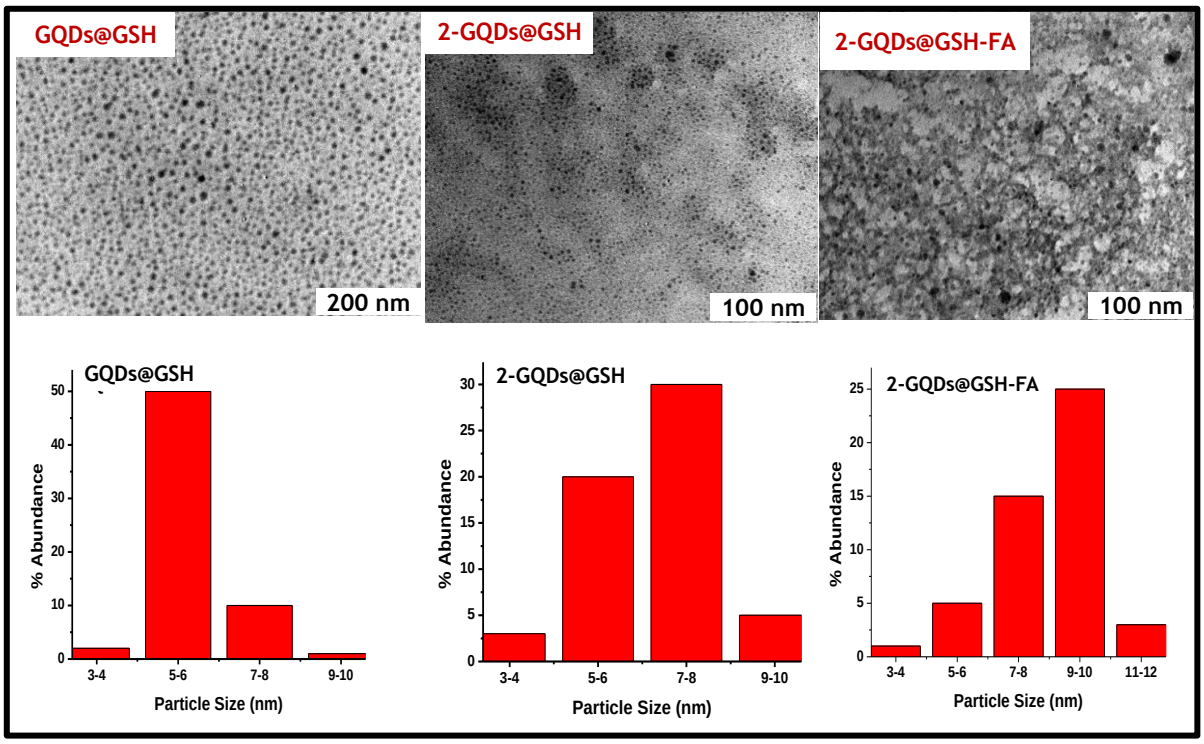

Figure 3.4: TEM images for GQDs@GSH, 2-GQDs@GSH and 2-GQDs@GSH-FA

Figure 3.5 shows TEM images of the AuNSs-CTAB and AuNRs-CTAB (4.0), as well as **4**-GQDs@GSH-AuNSs. TEM images of the CTAB-capped gold nanospheres show the distribution of small particles with an estimated particle size of 20 nm (average) (**Fig. 3.5**). TEM image of AuNRs shows that they are monodispersed (**Fig. 3.5**). Gold nanorods are monodispersed in aqueous solution. The morphology of the AuNSs-CTAB (as an example) did not change upon conjugation except for the slight changes in particle sizes. The average particle size of the conjugated spherical nanoparticles is 28 nm (**Table 3.1**), an increase from 20 nm of the nanospheres alone.

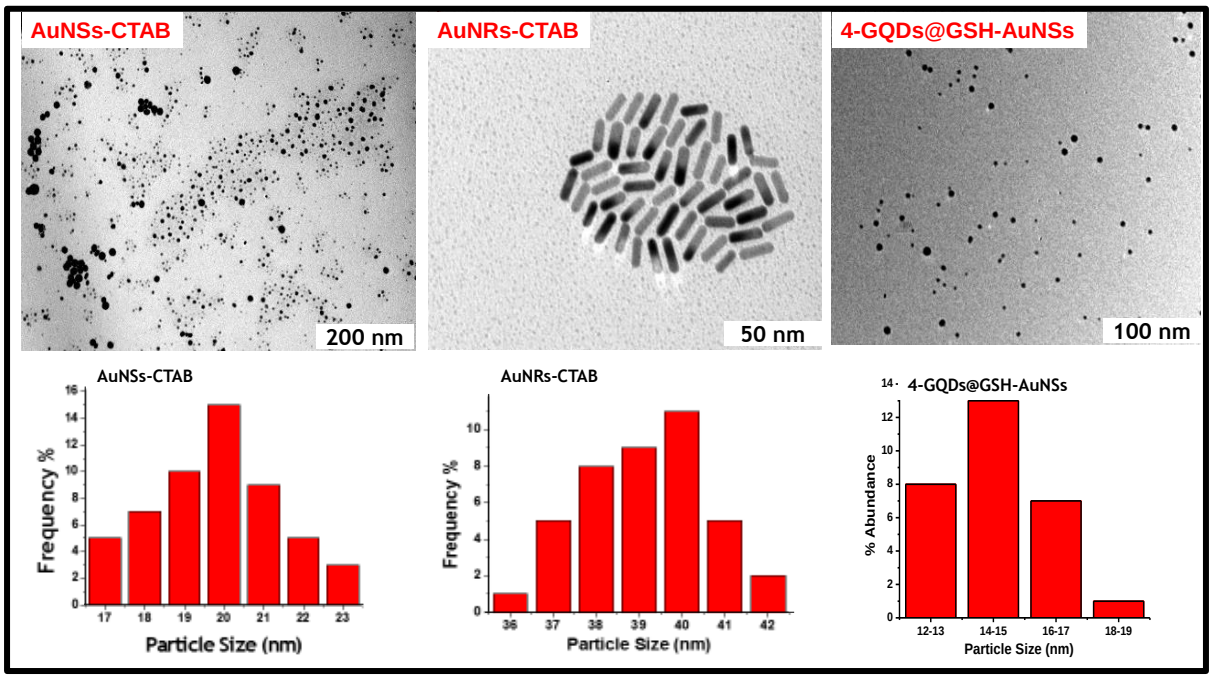

Figure 3.5: TEM images of AuNSs-CTAB and AuNRs-CTAB, and 4-GQDs@GSH-AuNSs with the corresponding size distributions (histograms) below.

For the conjugates of GQDs@GSH with complex **4** and then *in situ* synthesis of AuNPs on the GQDs/Pcs platform, monodispersity was observed in the **4**-GQDs@GSH conjugates. The TEM image shown in **Figure 3.5** clearly shows monodispersed composites of **4**-GQDs@GSH-AuNSs, further highlighting minimal aggregation in the composites. There were also observed size increases of the **4**-GQDs@GSH upon decoration with AuNSs. The increase in size following conjugation in each case confirms the successful modification at each stage and could be as attributed to π–π interaction of MPcs on adjacent NPs [**146,147**], which is possible in phthalocyanines.

3.2.2 AFM

GQDs@GSH and conjugates with complex **4** are used as examples. The AFM images of as-synthesized GQDs@GSH show their topographic morphology (**Figure 3.6**). As illustrated in **Figure 3.6**, the average height of GQDs@GSH is about 1.2 nm. As single-layered graphene

quantum dots or graphene oxide sheets have the thickness of 0.34 nm by AFM measurements, it is estimated that the synthesized GQDs@GSH should contain about three-four graphene layers [**39,148**]. The calculated surface roughness of 0.52 nm of the synthesized GQDs@GSH demonstrates their homogeneity. The topographic morphology of **4**-GQDs@GSH shows an increases in topographical height to about 6 nm (**Fig. 3.6**) and surface roughness value of 2.48 nm. The increase in topographical height could evidence the successful conjugation of the GQDs@GSH to complex **4**. Meanwhile, marked changes in surface morphology were noted for **4**-GQDs@GSH-AuNSs compared to that of either GQDs@GSH alone or **4**-GQDs@GSH (**Fig. 3.6**). The morphology of **4**-GQDs@GSH-AuNSs showed an uneven surface with wrinkles and voids and root mean square (RMS) roughness of 18.3 nm.

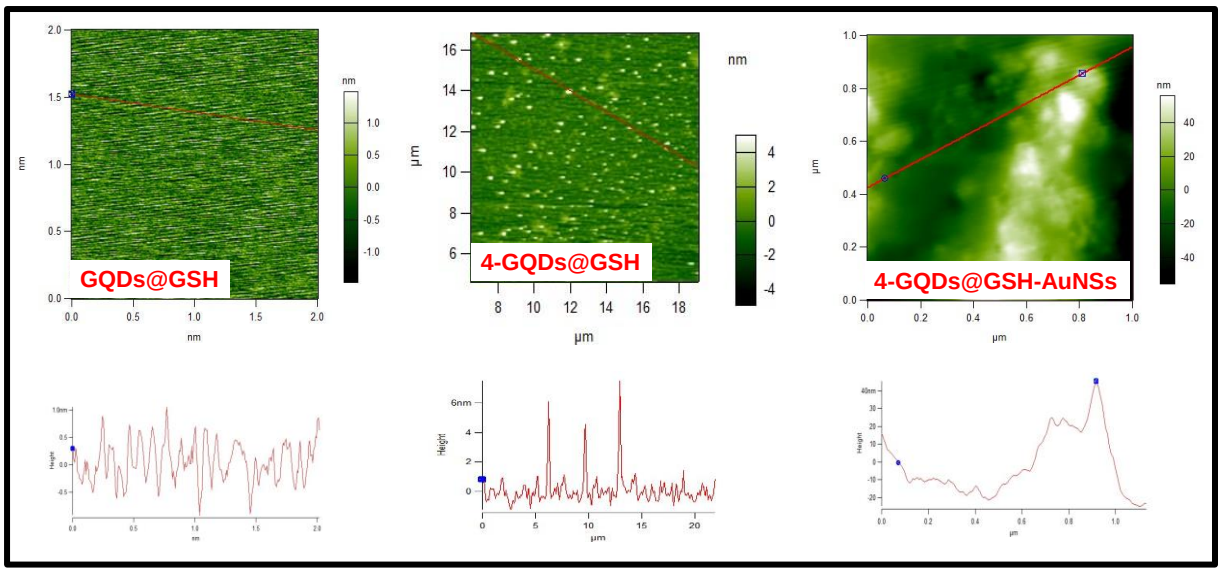

Figure 3.6: AFM images of GQDs@GSH, 4-GQDs@GSH and 4-GQDs@GSH-AuNSs with corresponding 2D height profiles below.

3.3 Energy dispersive spectroscopy (EDS)

Energy dispersive spectroscopy (EDS) was used to determine the elemental composition of the synthesized NPs and conjugates, **Fig. 3.7** using GQDs@GSH, complex **4** and conjugates as

examples. The results obtained were consistent with the expected elemental composition which further confirmed the synthesis of NPs. For complex **4**, the expected elemental composition was observed, which confirmed successful synthesis. Additional S peaks attributed to the presence of GQDs@GSH were observed in **4**-GQDs@GSH, and well as Au peaks owing to the successful assembly of AuNSs on the Pc/GQDs@GSH nanoplatform to form **4**-GQDs@GSH-AuNSs (**Fig.3.17**).

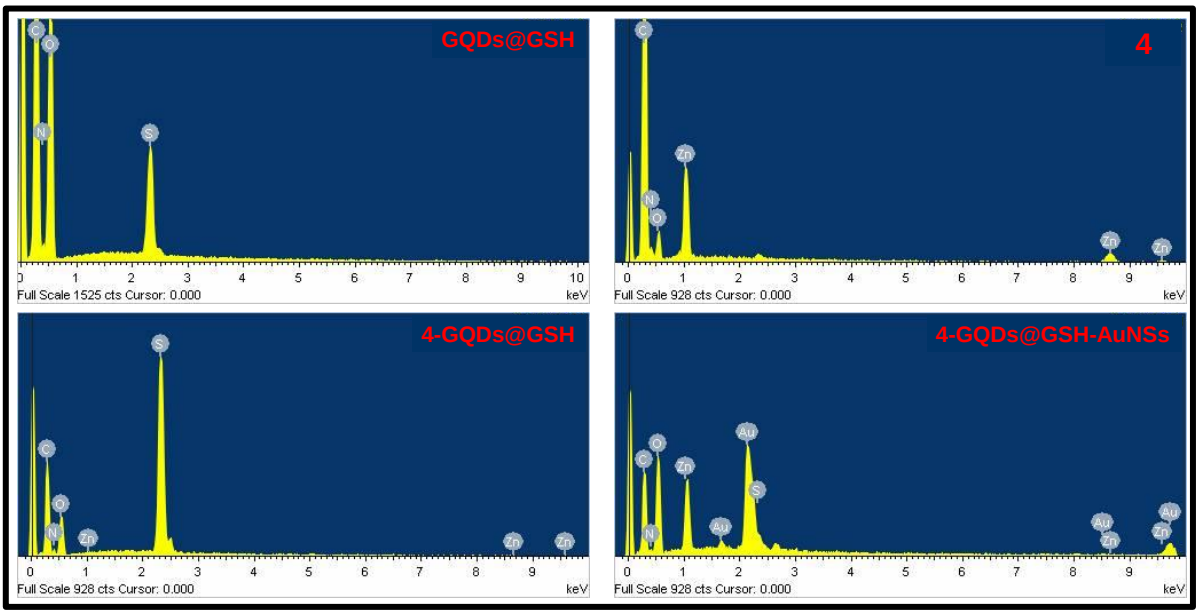

Figure 3.7: Representative EDS of GQDs@GSH, complex 4, 4-GQDs@GSH and 4-GQDs@GSH-AuNSs showing all expected elements.

3.4 Dynamic light scattering measurements (DLS)

All the synthesized NPs and conjugates were further analyzed for size distribution using dynamic light scattering (DLS) techniques, with conjugates of complex **3** with GQDs@GSH alone and BODIPY-GQDs@GSH used as examples (**Fig. 3.8**, data listed in **Table 3.1**). These results show that following conjugation, the hydrodynamic diameters of the GQDs increased, further suggesting the successful formation of desired conjugates. The rest of the DLS sizes

are listed in **Table 3.1**. In all cases, there is an increase in size following conjugation for reasons given above.

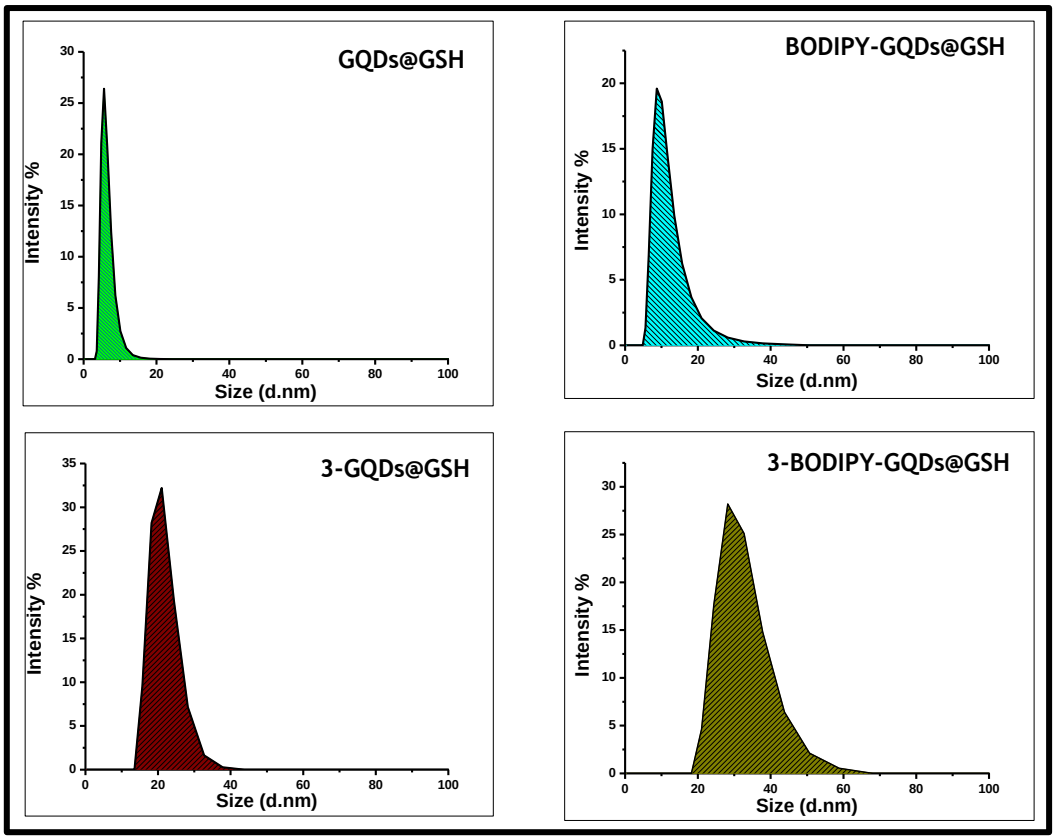

Figure 3.8: Representative DLS graphs showing average particle sizes for GQDs@GSH alone, BODIPY-GQDs@GSH, 3-GQDs@GSH, and 3-BODIPY-GQDs@GSH, showing resultant changes in sizes of the respective GQDs (GQDs@GSH and BODIPY-GQDs@GSH) upon conjugation to complex 3.

3.5 Electronic spectra of NPs and conjugates

3.5.1 GQDs and FA

Figures 3.9 (**A**) and **3.9** (**B**) show the absorption and photoluminescence spectra of GQDs@GSH and GQDs@GSH-FA. From the figure, the strong absorption below 400 nm is attributable to the n–π* electronic transitions caused by the oxygen containing groups on the surface of the GQDs [**149**]. The absorptions of GQDs@GSH showed a slight (2 nm) blue shift

in the presence of FA, **Table 3.1**. This shift can be attributed to the interaction of GQDs@GSH with FA, which is due to decrease in the energy band gap that existed in GQD@GSH alone. GQDs@GSH may exhibit excitation wavelength-dependent (where there is a change in emission wavelength with changes in excitation wavelength) or excitation wavelength-independent (where there is no change in emission wavelength, but there may be a change in intensity) emission. This excitation-dependent fluorescence behaviour is known for carbon-based nanomaterials [**53**] and is proposed to reflect the differences in nanoparticle sizes and surface defects for GQDs [**150**]. Both GQDs@GSH and GQDs@GSH-FA exhibit excitation-dependent photoluminescence (PL) behaviour. GQDs@GSH showed maximum emission at 450 nm and GQDs@GSH-FA at 446 nm, both at an excitation wavelength of 340 nm.

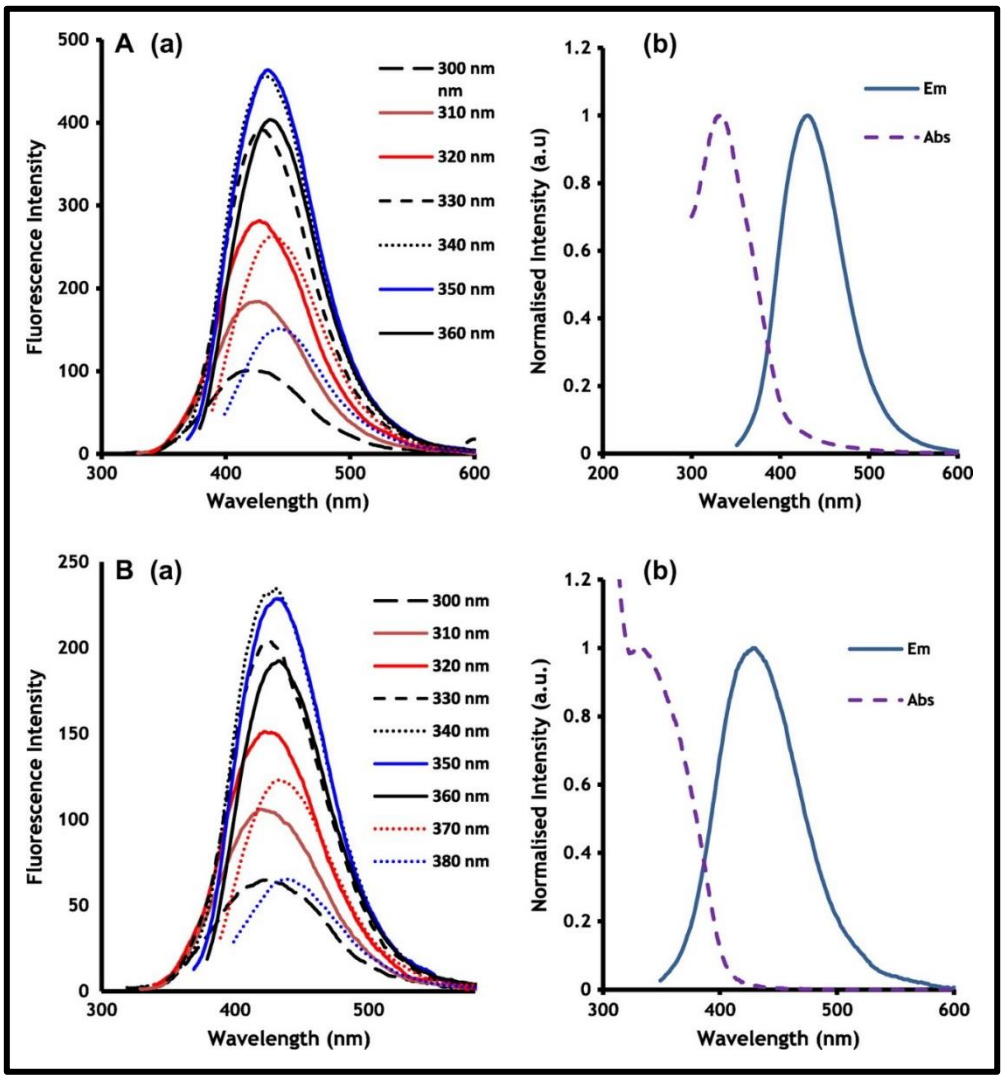

Figure 3.9: (a) Effects of excitation wavelength on emission spectra and (b) absorption and emission spectra of GQDs@GSH (A) and GQDs@GSH–FA (B). Excitation wavelength = 340 nm in DMSO. Em = emission spectra, Abs = absorption spectra.

3.5.2 AuNPs and AgNPs

The UV–Vis spectra of AuNSs@GSH and AgNSs@GSH show a characteristic SPR band at 531 nm and 416 nm respectively (**Fig. 3.10A**).

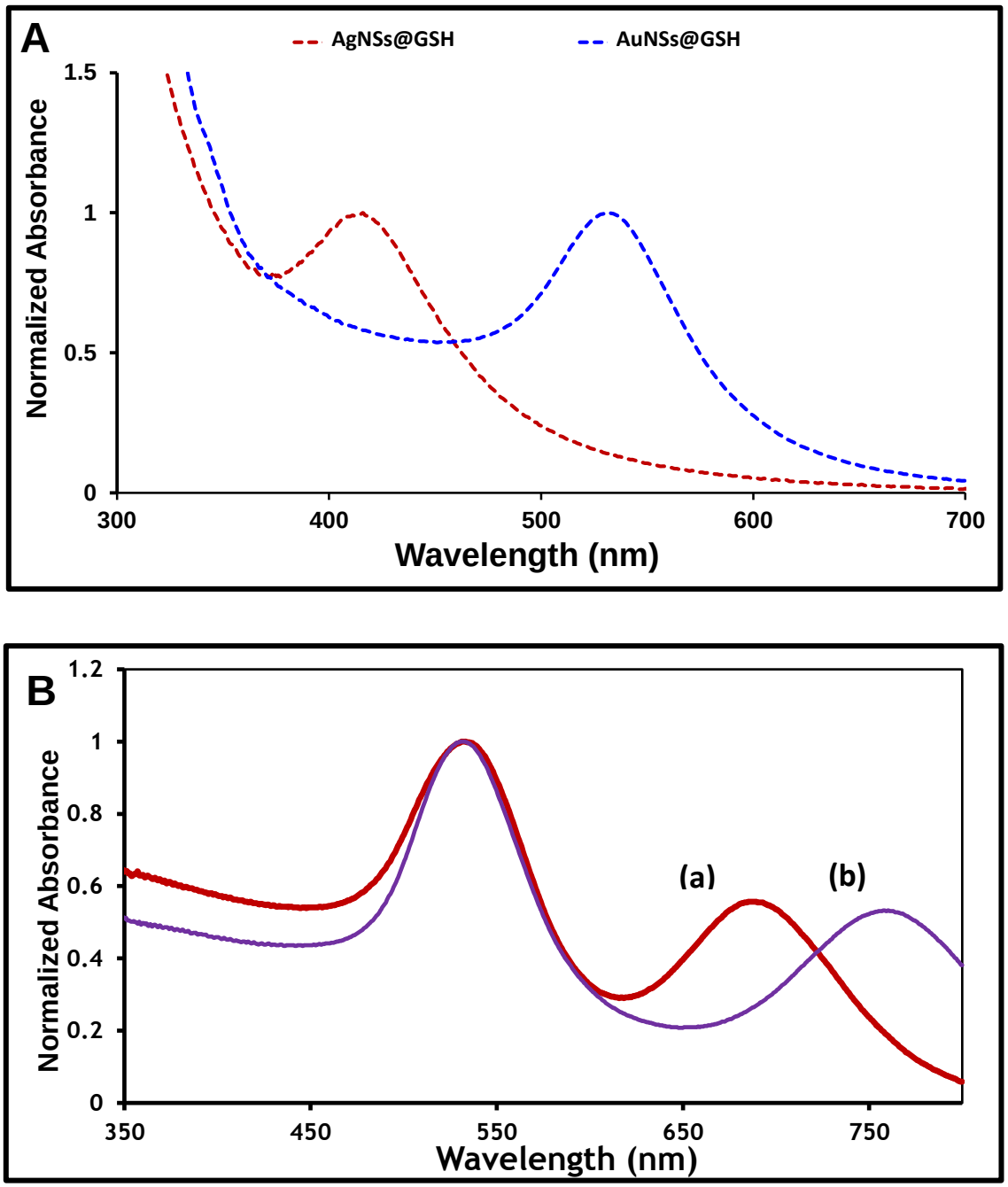

Figure 3.10: Ground state absorption spectra of AuNSs@GSH and AgNSs@GSH (A), and CTAB stabilized (a) AuNRs-CTAB (2.0), and (b) AuNRs-CTAB (4.0) in water (B).

The AuNSs-CTAB displayed an SPR band at 532 nm (**Table 3.1**). Gold nanorods (AuNRs-CTAB) on the other hand have two characteristic SPR peaks (transverse and longitudinal) as observed in **Figure 3.10B** and listed in **Table 3.1**. The transverse peak remained unchanged at

532 nm with change in aspect ratio, while the longitudinal peak was tuned to the near-infrared (NIR) region by increasing the aspect ratio (**Table 3.1**). The AuNRs spectra may be used in monitoring aggregation using the increase in the transverse to longitudinal (T-to-L) peak ratio [**150**]. AuNRs-CTAB (2.0), and AuNRs-CTAB (4.0) showed significant increases in the T-to-L peak ratio after self-assembly of the GQDs@GSH unto their surfaces (**Table 3.2**). The values are: 1.77, 2.0, 2.8, and 2.6 for AuNRs (2.0), AuNRs (4.0), GQDs@GSH/AuNRs (2.0), and GQDs@GSH/AuNRs (4.0) respectively. These changes can indicate potential aggregation of nanorods during the conjugation procedure [**151**]. The observed aggregation in the AuNRs though minimal (as indicated by the relatively small changes in T/L ratio), may be because glutathione (GSH) has both amine and the carboxyl groups, which can act as crosslinking agents between gold nanoparticles, therefore making the conjugates prone to aggregation [**151**].

Table 3.2: Properties of AuNPs showing surface area, transverse to longitudinal peak ratio, as well as loading of GQDs.

Sample	Surface Area (nm^2) (From Eq. 2.1)[a]	Transverse to longitudinal peak ratio[b]
GQDs@GSH/AuNSs	**2830**	**-**
GQDs@GSH/AuNRs (2.0)	**1100**	**1.77 (2.8)**
GQDs@GSH/AuNRs (4.0)	**1415**	**2.0 (2.6)**

[a]Surface area of AuNPs alone. [b]Numbers in brackets are for the respective AuNPs conjugates with GQDs@GSH.

3.5.3 BODIPY/Pcs conjugates

The ground state absorption spectra of **3**-BODIPY-GQDs@GSH (**Fig. 3.11**) showed characteristic absorptions for both complex **3**, as well as the BODIPY-GQDs@GSH moieties. The strong absorption below 400 nm is attributed to the presence of the GQDs@GSH. The absorption bands belonging to the BODIPY shifted from 525 nm when alone to 526 nm and 527 nm for BODIPY-GQDs@GSH and **3**-BODIPY-GQDs@GSH, respectively, **Table 3.1**. For GQDs@GSH, the absorption band shifted from 332 nm for GQDs@GSH alone to 335 nm for BODIPY-GQDs@GSH, and 340 for **3**-BODIPY-GQDs@GSH, **Table 3.1**. Shifts in peak positions can be attributed to increases in the size of the nanoparticles subsequent to conjugation with complex **3** (as illustrated by DLS sizes) (Note: complex **3** was linked to GQDs@GSH and BODIPY-GQDs@GSH). No significant shifts were observed for the Q-band of complex **3** on coordination to either GQDs@GSH or BODIPY-GQDs@GSH (**Table 3.1**). This was also the case for all Pc complexes in the presence of NPs (**Table 3.1**), except for the absorbance of the NPs in the conjugates (**Fig. 3.12**). The retention of the respective absorptions

of the Pcs post conjugation further indicates the preservation of the structural integrity of the respective Pcs following conjugation with NPs.

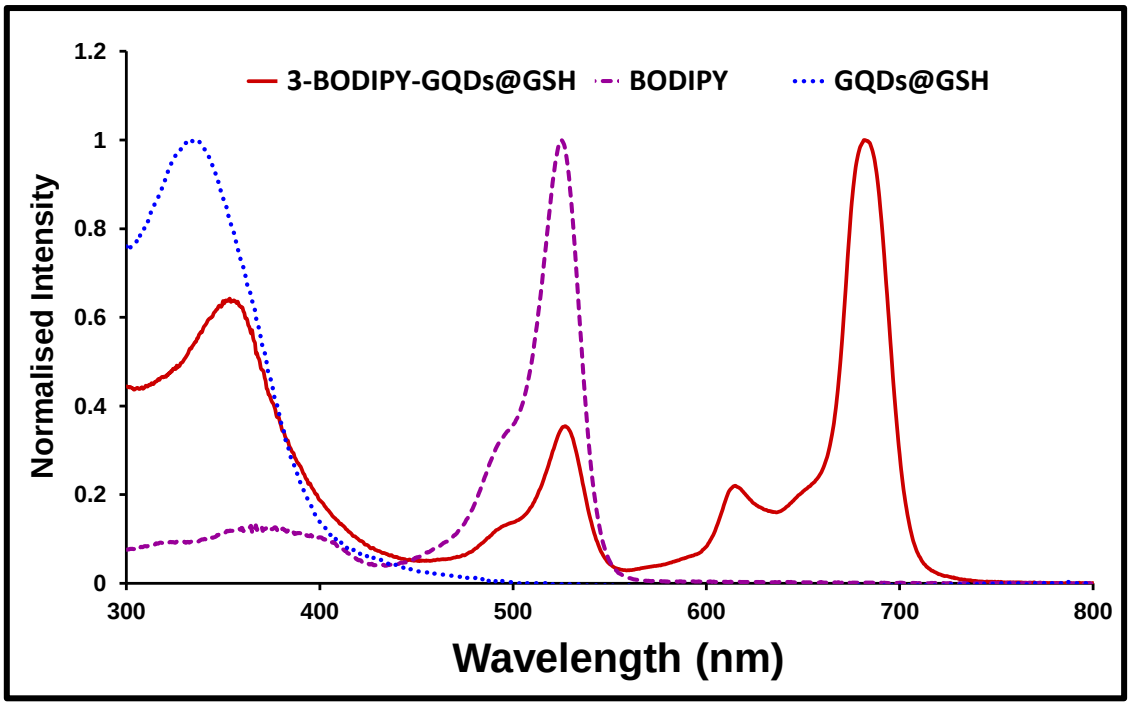

Figure 3.11: Electronic absorption spectra for 3-BODIPY-GQDs@GSH, BODIPY dye, and GQDs@GSH.

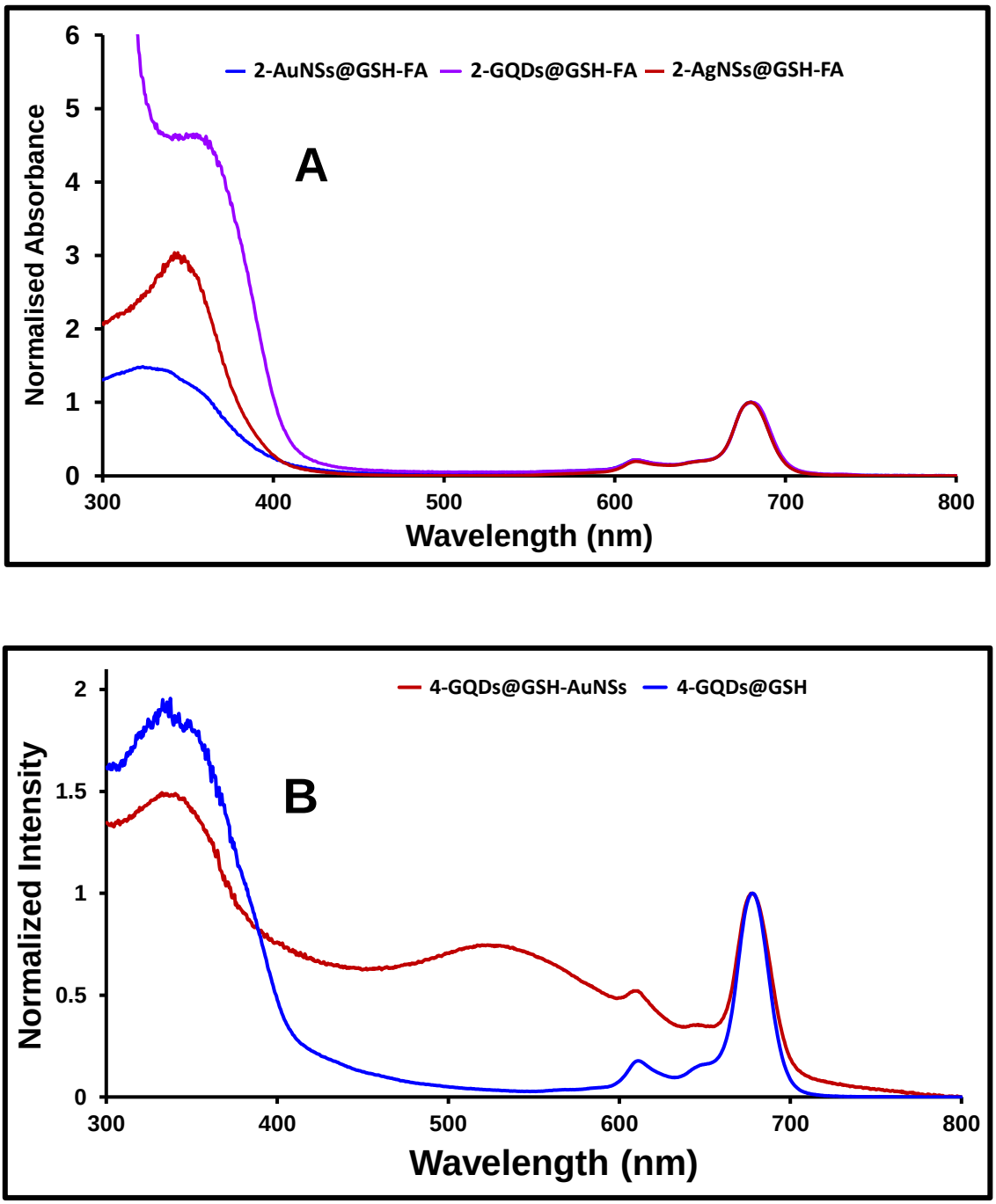

Figure 3.12: Ground state absorption spectra of (A) 2-GQDs@GSH-FA, 2-AuNSs@GSH-FA and 2-AgNSs@GSH-FA, (B) 4-GQDs@GSH and 4-GQDs@GSH-AuNSs in DMSO.

3.5.4 Loading of MPcs and BODIPY to NPs

It is possible that more than one Pcs or BODIPY are linked to the nanoparticles as a consequence of the fact that the approximate size of Pc or BODIPY is 1 nm, which is far less than that of the nanoparticles employed in this work (≥ 2 nm). The loading of BODIPY and Pcs unto the nanoparticles was therefore estimated following literature reports using UV-Vis spectrometry [**137**]. It involves comparing the absorbance intensities of each Pc or BODIPY before and after conjugation. This is then related to the respective molar absorptivity of the respective Pcs or BODIPY to determine loading. The results are summarized in **Table 3.1**.

The mass loading of compound **2** in **2**-AuNSs@GSH-FA, **2**-AgNSs@GSH-FA and **2**-GQDs@GSH-FA, were estimated to be 28, 45 and 19 µg/mg of conjugate, respectively, **Table 3.1**. AgNSs@GSH containing conjugates showed the largest loading, and GQDs@GSH conjugates showed the lowest loading. This could be related to the sizes of the NPs (as was determined by TEM and DLS). The large size of AgNSs@GSH allows for more Pcs to be loaded compared to AuNSs@GSH and GQDs@GSH. The loading of **3** onto the GQDs@GSH and BODIPY-GQDs@GSH was also determined. The largest loading was observed for **3**-BODIPY-GQDs@GSH with a loading of 26 µg/mg of conjugate, compared to **3**-GQDs@GSH with a loading of 20 µg/mg of conjugate. The larger loading of the BODIPY-GQDs@GSH may be as a result of the larger size of the NPs allowing for more Pcs to be loaded. It has been reported that the mass loading of Pcs to NPs is dependent on the size and surface areas of the NPs [**152**]. This trend was observed for most conjugates studied, with the exception of complex **1** where the larger GQDs@GSH-FA had the smaller loading **(Table 3.1)**.

3.6 Zeta potential (ζ)

Zeta potential is a measure of charges carried by particles suspended in a liquid (mostly water). It is widely used for quantification of the magnitude of the charge. The zeta potential is a key indicator of the stability of colloidal dispersions. The magnitude of the zeta potential indicates the degree of electrostatic repulsion between adjacent, similarly charged particles in a dispersion. A high zeta potential confers stability (the solution or dispersion will resist aggregation). When the zeta potential is small, attractive forces may exceed repulsion. Therefore, colloids with high zeta potential (negative or positive) are electrically stabilized.

Zeta potential values for the GQDs are shown in **Table 3.3**. GQDs alone has a potential of −16.4 mV, GQDs@GSH has a potential of -18.1 mV indicative of highly negative surface charges. This is due to the presence of carboxyl and hydroxyl groups in GQDs [**137**]. The zeta potential of GQDs@GSH becomes −7.9 mV upon conjugation to FA. The decrease in the magnitude of the zeta potential points to loss in the dispersibility (and hence stability) of the GQDs following modification, indicative of aggregation in the conjugate GQDs@GSH-FA.

The zeta potential values for conjugates of complex **3** are discussed as examples. Complex **3** alone had a low positive zeta potential of 6.7 mV. However, hybridization with GQDs@GSH and BODIPY-GQDs@GSH, resulted in increase (compared to complex **3**) in the electrostatic repulsions and therefore stability (for **3**-GQDs@GSH and **3**-BODIPY-GQDs@GSH), with zeta potential values of -18.7 mV **a**nd -16.5 mV, respectively (**Table 3.3**). Moreover, the high zeta potential values following hybrid formation points to improvements in the dispersibility of the resulting supramolecular structures, signifying high colloidal stability. This property is very favourable for biological applications [**150**]. For all other conjugates, there was a general increase in dispersibility of the conjugates as compared to the individual Pcs alone (**Table 3.3**), an important property especially in biological applications.

Table 3.3: Zeta potential values of the NPs, Pcs and BODIPY, and their respective conjugates.

Compound	Zeta potential (ζ)
GQDs	-16.4
GQDs@GSH	-18.1
GQDs@GSH-FA	-7.9
AuNSs	7.34
AuNRs (2.0)	14.5
AuNRs (4.0)	20.1
GQDs@GSH/AuNSs	4.86
GQDs@GSH/AuNRs (2.0)	9.24
GQDs@GSH/AuNRs (4.0)	9.64
1	-7.9
1-GQDs	-6.1
1-GQDs@GSH	-8.2
1-GQDs@GSH-FA	-7.1
3	6.7
3-GQDs@GSH	-18.7
BODIPY	-6.4
BODIPY-GQDs@GSH	-11.6
3-BODIPY-GQDs@GSH	-16.5
4	-8.7
4-GQDs@GSH	-21.1
4-GQDs@GSH-AuNSs	-16.7

3.7 FT-IR Spectra

3.7.1 GQDs alone or with FA

FT-IR analysis was used to characterize and determine the surface functional groups of the GQDs. The spectra reveal the presence of functional groups which usually dominate the edges of GQDs [**27**]. The FT-IR spectrum of the pristine GQDs alone show a broad peak around 3615 – 3010 cm^{-1} attributed to the presence of O-H stretching vibration and a peak at 1683 attributed to COOH stretching vibration (**Fig 3.13**). A peak at around 2515 cm^{-1} attributed to the presence of the S-H group can be found in the GQDs@GSH. The successful conjugation of GQDs@GSH to FA to give GQDs@GSH-FA was confirmed using FT-IR (**Fig 3.13**). As can the observed in **Figure 3.13**, the FT-IR spectrum of the GQDs@GSH shows the presence peaks at 3360 and 3217 cm^{-1} attributable to the primary amine which are known to have two "fangs". It can be observed that upon linkage to the FA, the two peaks disappear, with the appearance of a new single peak at 3466 cm^{-1}. The disappearance of the two peaks (N-H) is as a result of chemical bonding of amino group of the GQDs@GSH to the carboxyl groups of the FA. The emergence of a new single peak at 3466 cm^{-1} confirms the successful conjugation and hence formation of the resultant GQDs@GSH-FA (**Fig 3.13**).

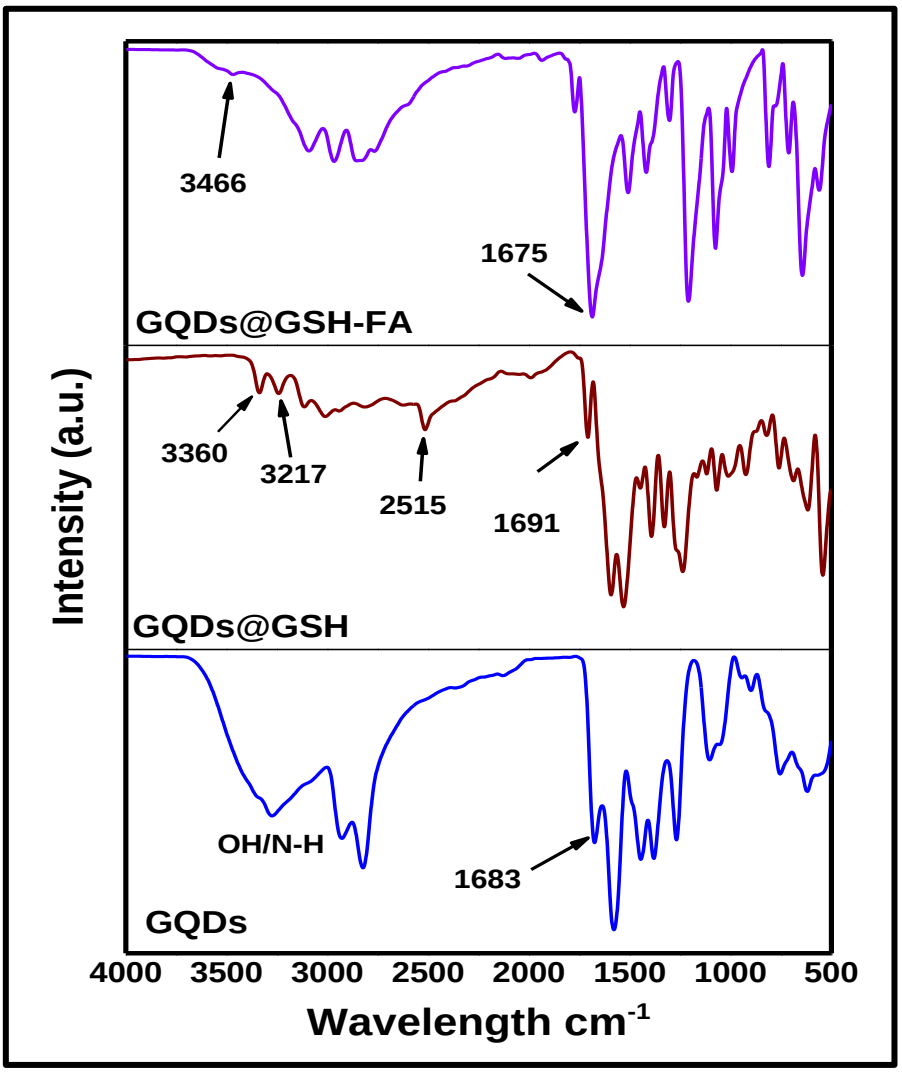

Figure 3.13: FT-IR spectra of the as-synthesized GQDs, GQDs@GSH, and GQDs@GSH-FA.

3.7.2 BODIPY/Pcs conjugates

The FT-IR spectra of the respective Pcs, BODIPY, NPs and their corresponding conjugates were compared. The successful conjugation of BODIPY to GQDs to give BODIPY-GQDs@GSH and the conjugation of complex **4** to GQDs@GSH to give **4**-GQDs@GSH, as well as the subsequent self-assembly of AuNPs onto the **4**-GQDs@GSH nanostructure were confirmed using FT-IR (**Fig. 3.14** and **Fig 3.15**), respectively (as examples). As stated above, the FT-IR spectrum of the GQDs@GSH (**Fig. 3.13**) shows the presence of two peaks at 3360

and 3217 cm^{-1}. It can be observed that upon linkage of the GQDs@GSH to the BODIPY, the two peaks disappear, with the appearance of a new single peak at 3321 cm^{-1} as a result of chemical bonding to carboxyl group of the BODIPY to the amino group of the GQDs@GSH. The emergence of a new single peak at 3321 cm^{-1} confirms the successful conjugation and hence formation of the resultant BODIPY-GQDs@GSH. Moreover, shifts in the C=O peak positions from 1683 cm^{-1} in the BODIPY dye (**Fig. 3.14a**) to 1616 cm^{-1} in the conjugate (BODIPY-GQDs@GSH) (**Fig. 3.14b**) were observed. Shifts in FT-IR bands are indicative of formation of a new compound, and hence confirms the formation of BODIPY-GQDs@GSH. Similar to that of BODIPY-GQDs@GSH, the FT-IR spectrum of the **4**-GQDs@GSH (**Fig. 3.15b**) shows the emergence of a new single peak at 3237 cm^{-1}.

The well-known affinity of Au to S was exploited for the *in-situ* synthesis of **4**-GQDs@GSH-AuNSs. The synthesised AuNSs are assembled onto the **4**-GQDs@GSH surface by Au–S bond due to the sulphur groups (owing to the presence of GSH) of the as-synthesised GQDs@GSH. The FT-IR spectrum of the *in-situ* synthesized **4**-GQDs@GSH-AuNSs is shown in **Figure 3.15b**. The C-H band of **4**-GQDs@GSH at 2932 cm^{-1} blue-shifted to 2923 cm^{-1} in **4**-GQDs@GSH-AuNSs. This may be ascribed to the interaction affinity of S-H groups to Au surface, which has been observed to change the vibration of C-H bonds [**153**]. In addition, the S-H band (which is clearly visible in GQDs@GSH at 2515 cm^{-1} (**Fig. 3.13**)) is absent in **4**-GQDs@GSH-AuNSs. This also suggests the breaking of S-H bond of the thiol in order to form the S-Au bond [**154**].

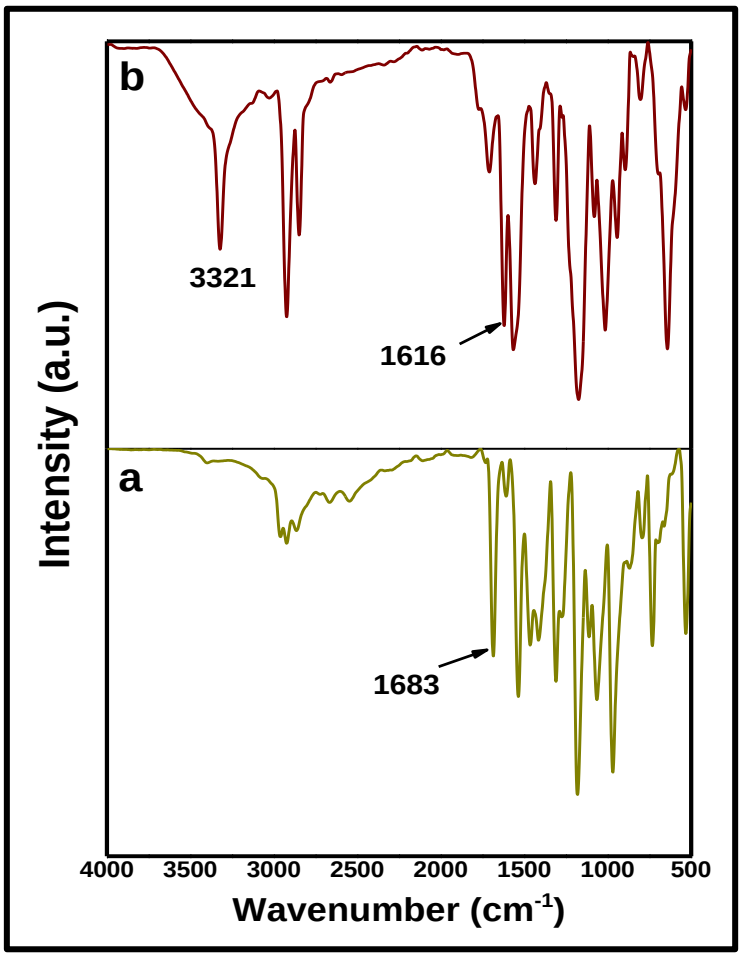

Figure 3.14: FT-IR spectra of (a) BODIPY and (b) BODIPY-GQDs@GSH showing amide bond formation.

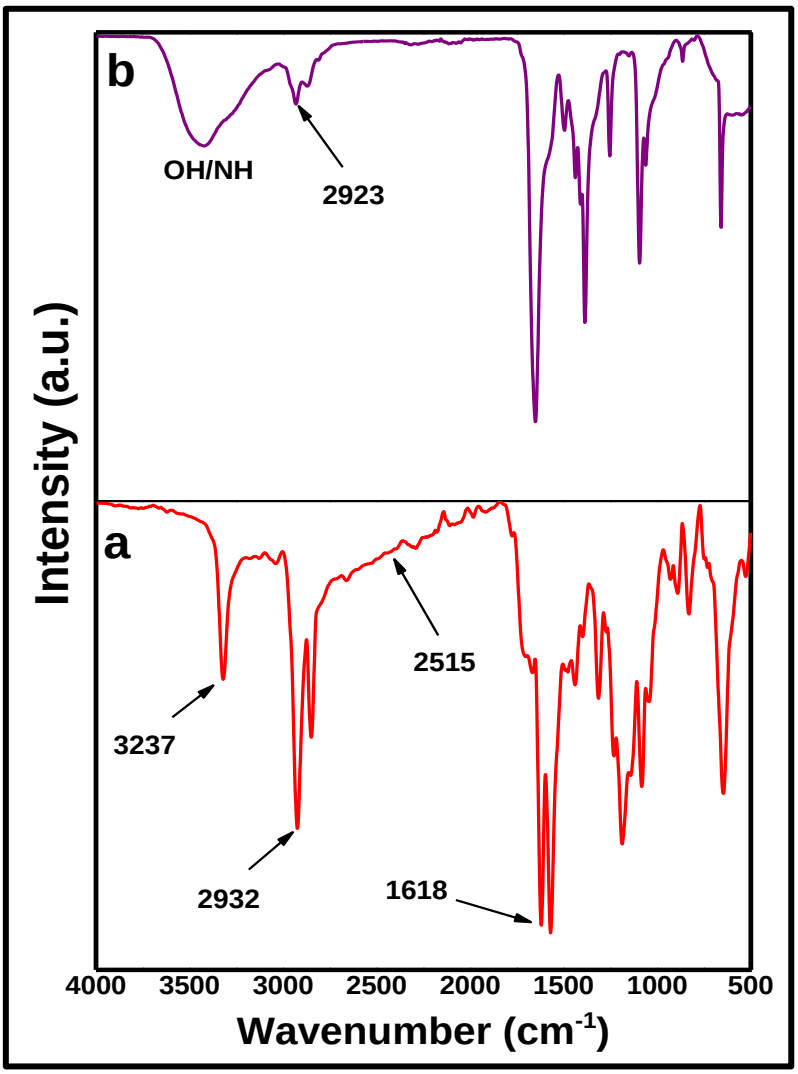

Figure 3.15: FT-IR spectra of 4-GSH@GSH (a) and 4-GQDs@GSH-AuNSs (b).

3.8 X-ray diffractometry (XRD)

3.8.1 GQDs alone or with FA

Structural characterization of the GQDs and FA nanohybrids were carried out using powder XRD and the patterns are shown in **Fig. 3.16**. Both the GQDs alone and GQDs@GSH exhibit main (broad) diffraction peaks at 2θ ~25º which is due to (002) Bragg's reflection of the carbon in the graphene layers [**150**]. The broadness of the XRD peak reflects their small size and is consistent with previous structural analysis results documented for GQDs [**155**]. The sharp peaks for the GQDs@GSH–FA (**Fig. 3.16**) were not present in the GQDs@GSH alone. These

sharp peaks can be attributed to the presence of FA, which has also been reported for other FA conjugates [**156,157**], suggesting an increase in size following conjugation as shown by DLS measurements.

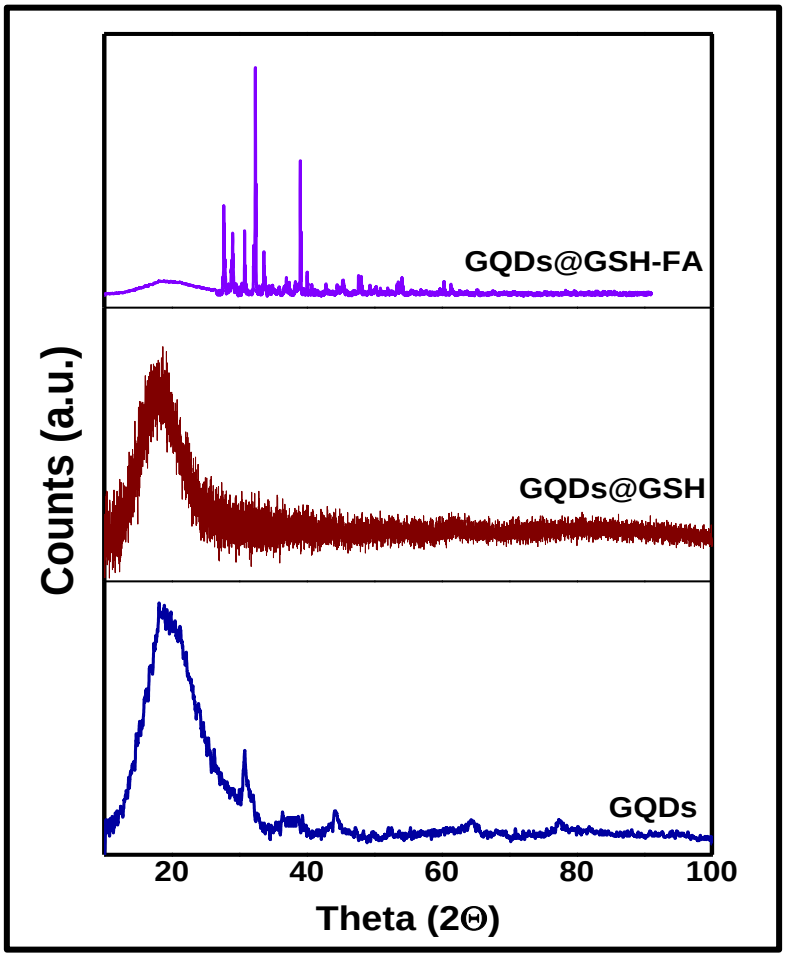

Fig. 3.16: Powder XRD spectra of as-synthesized GQDs, GQDs@GSH, and GQDs@GSH-FA.

3.8.2 AuNPs conjugates

The XRD diffractograms of the respective complexes as well as their conjugates were measured. Complex **2** was linked with AuNSs@GSH and then to FA in tandem and is used as an example. For complex **2**, the XRD pattern (**Fig 3.17**) is typical of phthalocyanines [**158**]. The broadness of the XRD peaks for complex **2**, suggests an amorphous form. AuNSs@GSH

(**Fig 3.17**) on the other hand, shows distinct Braggs reflections corresponding to planes {111}, {200}, {220} {311} and {222} at 2θ = 38.24, 44.54, 64.79, 77.79°, and 82.13° (**Table 3.4)**, which were indexed to the face centred cubic crystal structure of the gold nanoparticles, and conclusively proves the formation of gold nanocrystals with reference to the crystal structures from the PCPDFWIN: Au (#04-0784) [**159**]. **2**-AuNSs@GSH shows peaks due to AuNPs and the broad peaks due to complex **2** around 18.64°, **Fig 3.17c**. **2**-AuNSs@GSH-FA, shows peaks due to **2**-AuNSs@GSH, and additionally, sharp peaks attributed to the presence of FA (**Fig 3.17**), which as has been stated above have also been reported for other FA conjugates [**156,157**]. Debye-Scherrer Eq. (**3.1**) [**160**] was employed for the estimation of the sizes of the AuNSs@GSH:

$$\boldsymbol{d} = \frac{k\lambda}{\beta cos\theta} \qquad (\mathbf{3.1})$$

where λ is the wavelength of the X-ray source (1.5405 Å), k is an empirical constant equal to 0.9, β is the full width at half maximum of the diffraction peak and θ is the angular position (Braggs angle). The average sizes (diameters) are 9.55 nm and 13.35 nm for the AuNSs@GSH and **2**-AuNSs@GSH, respectively. These sizes were in close agreement with the sizes determined using DLS (**Table 3.1**). The sizes of the NPs increase following conjugation as observed above. There were further increases in size upon linking to FA most likely owing to aggregation as discussed above [**161**] (**Table 3.1**). It has however been reported that both the change in interplanar space and the degree of crystallization imply a new crystal form or a new compound in phthalocyanines [**162**]. Thus, the change in 2θ angles and d-spacings including the appearance of new XRD peaks, (**Table 3.4**) confirm a new crystal formation or a new compound, confirming conjugation.

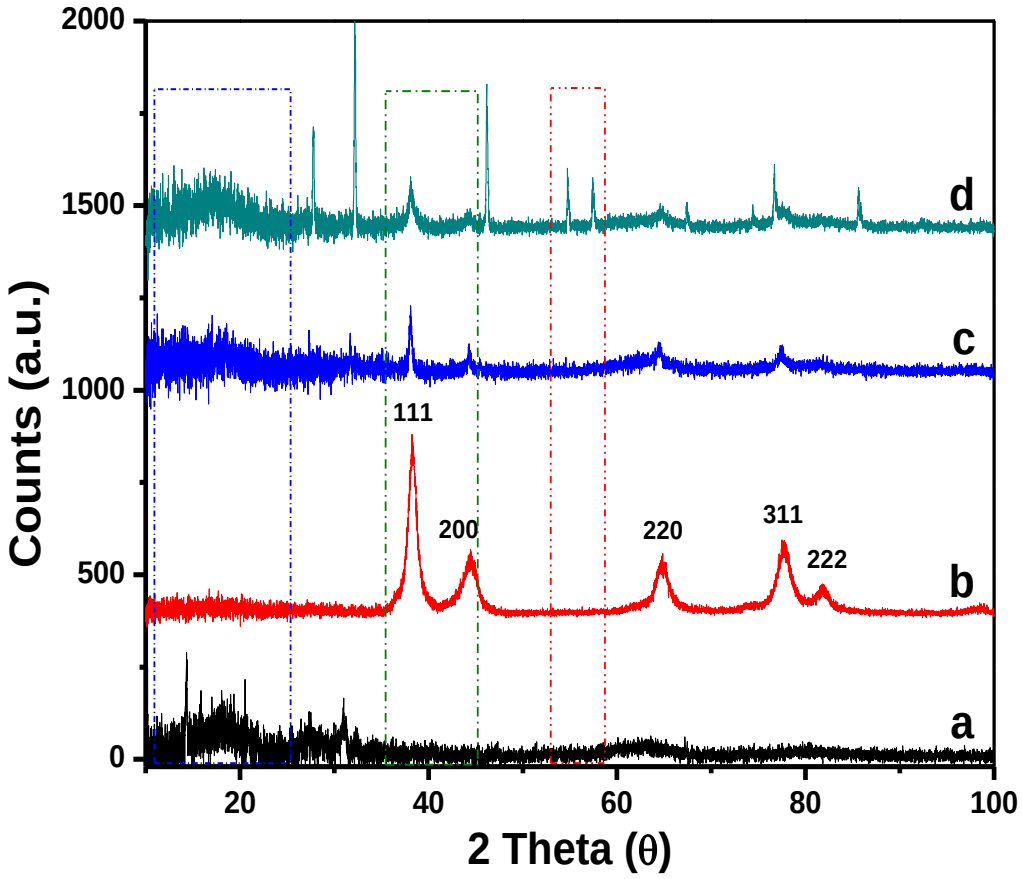

Figure 3.17: XRD patterns for (a) complex 2 alone, (b) AuNSs@GSH, (c) 2-AuNSs@GSH and (d) 2-AuNSs@GSH-FA.

Table 3.4: XRD parameters for complex 2, AuNSs@GSH, 2-AuNSs@GSH and 2-AuNSs@GSH-FA conjugates.

Compound	d-spacing of peaks and 2θ values						
AuNSs@GSH	d-spacing		2.35	2.03	1.44	1.23	1.17
	2θ value		38.24	44.54	64.79	77.77	82.13
2	d-spacing	4.75					
	2θ value	18.64					
2-AuNSs@GSH	d-spacing	4.77	2.37	2.03	1.44	1.23	
	2θ value	18.58	37.96	44.28	64.56	77.50	
2-AuNSs@GSH-FA	d-spacing	4.96	2.36	2.05	1.44	1.24	
	2θ value	17.85	38.15	44.12	64.57	76.70	

3.9 Raman Spectroscopy

3.9.1 GQDs with FA

Raman spectroscopic technique was employed to determine the quality of the GQDs and their nanohybrids with FA. GQDs are known to display characteristic Raman peaks termed the G-band (tangential mode, sp^2) and the D-band (breathing mode, sp^3). The G-band is a result of in-plane vibrations of sp^2 bonded carbon atoms, whereas the D-band is due to out of plane vibrations attributed to the presence of structural defects [**163**]. As shown in **Fig. 3.18**, these peaks occurred at 1593, 1593, and 1509 cm^{-1} (G-band) and 1286, 1287 and 1276 cm^{-1} (D-band) for GQDs, GQDs@GSH and GQDs@GSH-FA, respectively. The observed shifts are due to the cooperative defects of GSH functionalization (heteroatom doping) and covalent linkage to FA, thus stretching of the graphitic layers as previously reported in literature [**163**]. The I_D/I_G, which is the ratio of the intensities of D and G-bands is an important parameter in the study of the structural properties of carbon nanomaterials [**156**]. The intensity of the D-band is expected to be enhanced on functionalization [**164**,**165**], resulting in an increase in the D:G ratio. This

is because the D-band is enhanced by the presence of defects due to conversion of sp^2 to sp^3. The G-band is usually not as affected by defects. Increases in the G-band or D-band intensity on functionalization depends on the type of functionalization (covalent or non-covalent) among other factors. For GQDs, GQDs@GSH and GQDs@GSH-FA, the I_D/I_G were determined to be 0.23, 0.27 and 4.4, respectively. The increase in I_D/I_G reveal that both heteroatom doping with GSH, as well as linking to FA result in greater defects in the GQDs, with the linking to FA having the greatest effect.

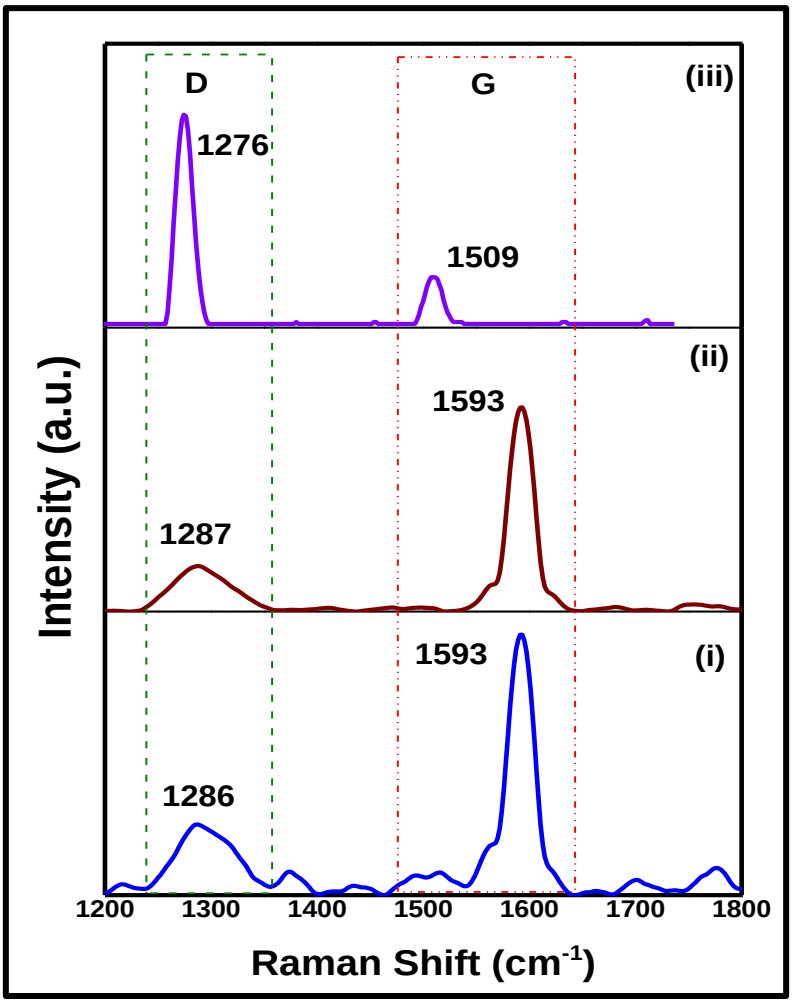

Figure 3.18: Raman spectra for (i) pristine GQDs and (ii) GQDs@GSH and (iii) GQDs@GSH-FA.

3.9.2 BODIPY/Pcs conjugates

As can be seen (**Fig. 3.19**), upon modification of the GQDs@GSH (shown in **Fig. 3.18**) with the BODIPY to form BODIPY-GQDs@GSH, a large shift in the frequency of the D-band is observed from 1287 to 1419 cm^{-1}. The G-band on the other hand, was not as significantly affected. The same band positions applied to **3**-BODIPY-GQDs@GSH, **Fig. 3.19 (ii).** A similar observation applied to the conjugation of the GQDs@GSH to complex **4**, (**Figure 3.19 (iii)**) and chemisorption of AuNSs onto **4**-GQDs@GSH to form **4**-GQDs@GSH-AuNSs (**Figure 3.19 (iv)**). Shifts in the Raman frequencies are often indicative of strong π-electron interactions in hybrid materials [**154**], and hence implying formation of a new complex.

For all conjugates, the I_D/I_G were generally seen to increase following covalent conjugation. For the GQDs@GSH alone the calculated I_D/I_G was 0.27. Upon decoration with BODIPY the resultant I_D/I_G was determined to be 0.40. The I_D/I_G was also observed to increase to 0.30 upon conjugation to complex **4**. In both cases, the increase in the D:G ratio upon modification confirms increases in the structural disorder of the GQDs@GSH [**154**]. There was further increases in I_D/I_G upon self-assembly of the *in-situ* synthesised AuNPs to 0.77 due to Au-S bonds formed. The I_D/I_G for **3**-BODIPY-GQDs@GSH formed via π-π interaction between the BODIPY-GQDs@GSH and complex **3**, was 0.35. The decrease in the D:G ratio is due to increase in the G-band intensity. Increases in the G-band are associated with removal of some amorphous carbon from carbon nanostructures [**166**]. Defects of the graphene core structure of GQDs@GSH (and hence increases in D:G ratios) are not expected for **3**-BODIPY-GQDs@GSH since π-π interaction preserves the structural integrity of both interacting molecules and this type was observed for all the adsorbed complexes.

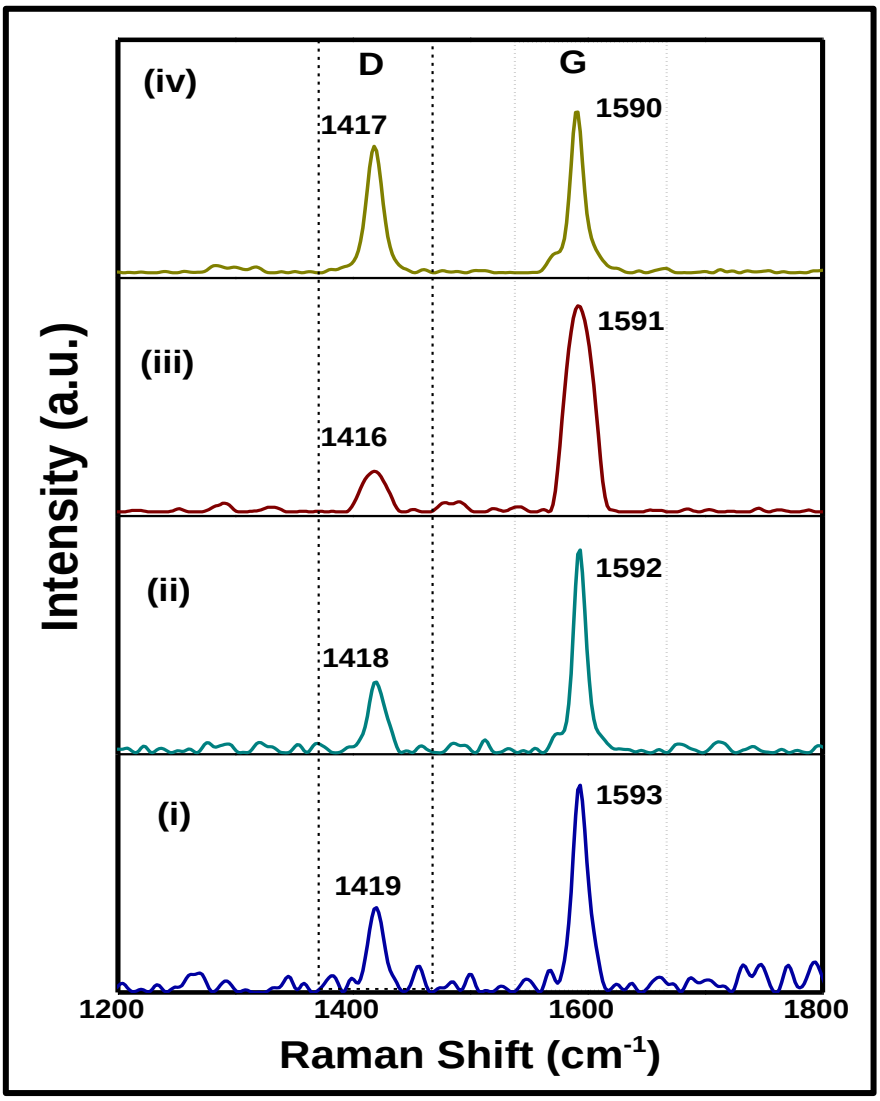

Figure 3.19: Raman spectra of BODIPY-GQDs@GSH (i), 3-BODIPY-GQDs@GSH (ii), 4-GQDs@GSH (iii), and 4-GQDs@GSH-AuNSs (iv), showing the corresponding Raman intensity changes of the GQDs@GSH upon conjugation to BODIPY and then to complex 3, and conjugation to complex 4, and resultant chemisorption of AuNSs to form 4-GQDs@GSH-AuNSs.

3.10 X-ray photoelectron spectroscopy (XPS)

3.10.1 GQDs with FA

XPS was employed to confirm amide bond formation between GQDs@GSH and FA. The N 1s high resolution peak for GQDs@GSH (**Figure 3.20 (a)**) was deconvoluted to yield three components at 396.5 eV, 399.2 eV, and 401.6 eV corresponding to N–H, N–C, and N–C=O, respectively. The component at high binding energy 401.6 eV is due to N–C=O (an amide bond) present in the glutathione, which was used to functionalize the GQDs (GQDs@GSH). The N 1s core level spectra for GQDs@GSH-FA (**Figure 3.20 (b)**) could be fitted to three chemically distinct components with binding energies 399.1, 399.8, and 402.1 eV due to N–C/N=C, N–H, and N–C=O bonds, respectively. The amide bond for GQDs@GSH alone was observed at 401.6 eV with an intensity of 422 cps, but shifted to 402.1 eV for GQDs@GSH-FA with an intensity of 3130 cps. The large increase in intensity is because GQDs@GSH has more than one amide bond due to amide bonds in GSH and the amide bond to FA. For the same mass of GQDs@GSH and GQDs@GSH-FA, the XPS quantification report also revealed an increase in percentage carbons going from GQDs@GSH to GQDs@GSH-FA (56.55% to 68.13%). This increase is evidence of successful conjugation of GQDs@GSH to FA.

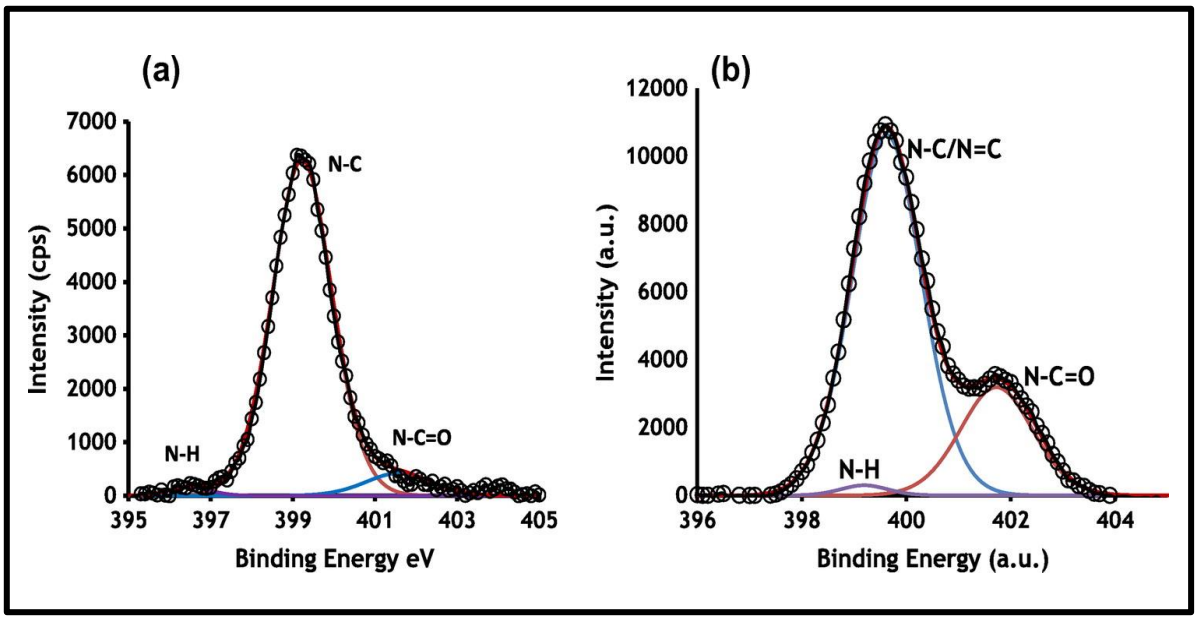

Figure 3.20: High-resolution spectra N1s for GQDs@GSH (a) and GQDs@GSH-FA (b).

3.10.2 Pcs conjugates

XPS analysis was employed in order to confirm the successful linkage of complex **2** to either GQDs@GSH or AuNSs@GSH or AgNSs@GSH and then to FA (used as examples). This was achieved with the core level binding energies aligned with respect to the C1s binding energy (BE) of 285 eV. The survey spectra of complex **2** and the conjugates depicted all the expected atomic compositions with their corresponding binding energies (**Fig. 3.21**). The S, C1s, N1s, O1s, and Z occurred at 161, 285, 400, 531, and 1020 (eV), respectively. The C 1s peaks in the survey spectra for the FA linked conjugates is higher than that of complex **2** alone with 19.70 % for complex **2,** 25.25% for **2**-GQDs@GSH, and 33.52 % for **2**-GQDs@GSH-FA (as examples) owing to the presence GSH and FA (carbon rich compounds) in the conjugates. The GQDs-containing conjugate had the highest carbon content, as GQDs are carbon rich.

The conjugates were further subjected to high resolution of N 1s XPS analysis to confirm the successful conjugation of the Pc to the nanoparticles via amide linkage (**2**-AuNSs@GSH and **2**-AuNSs@GSH-FA, as examples) (**Fig. 3.22 (A)**). The N1s spectra of **2**-AuNSs@GSH and

AuNSs@GSH alone depicted three sub peaks at 397.9, 398.3 and 406.2 eV. The three sub peaks correspond to N-C, N-H and N-C=O respectively, with signal at 406.2 eV attributed to the amide bond for **2**-AuNSs@GSH and AuNSs@GSH. The amide bond peak is high at 4111 cps for **2**-AuNSs@GSH compared to AuNSs@GSH at 3785 cps, due to more amide bonds in the former. Upon further conjugation to FA, slight shifts in the binding energies of the three peaks resulted with the N-H, N-C and N-C=O sub peaks occurring at 395.8, 396.5, and 397.9 eV, respectively. It is noteworthy that intensity of N-C=O was found to increase to 9155 cps after conjugation of the **2**-AuNSs@GSH to FA (**Fig 3.22 (A)**). This apparent increase in the intensity of N-C=O in the FA linked complex suggests increase in amide bond formation, hence successful linkage to FA.

Since sulphur to metal interaction is expected, the high resolution spectra of S 2p were performed. This is because there is a probability of complex **2** in the **2**-AuNSs@GSH (as an example) interacting with the surface of the nanoparticles via an S-metal or N-metal bond (depending the orientation of **2**). It is important to note however, that this possibility should be treated with caution since the glutathione used in functionalizing the nanoparticles also possesses sulphur which will result in S-Au interaction. The S 2p peak of AuNSs@GSH was deconvoluted to three sub peaks due to S–C, S and S-Au, at 160.7 eV, 162.2 eV and 165.4 eV respectively, **Fig 3.22 (B)**. The existence of the three S 2p peaks is as a result of spin–orbit coupling [**167**]. A similar pattern was observed in the conjugates, and upon de-convolution of **2**-AuNSs@GSH, three sub peaks corresponding to S–C, S and S–Au at 161.7 eV, 163.3 eV and 166.8 eV respectively were obtained (**Fig 3.22 (B)**). An increase in the intensity of the S-Au peak from 590 cps (for AuNSs@GSH) to 3361 cps (for **2**-AuNSs@GSH) was also noted. The S-Au peak in the conjugate most likely resulted from the interaction between S–Au from both the sulphur in the Pc ring and the sulphur from GSH since there was appreciable change in intensity of the three subpeaks before and after conjugation. The S-C, and S peaks were also

observed to have changed intensities from 1885 cps and 1281 cps for AuNSs@GSH to 4356 and 3682 cps for **2**-AuNSs@GSH further buttressing that the interaction is as a result of both the GSH and complex **2**.

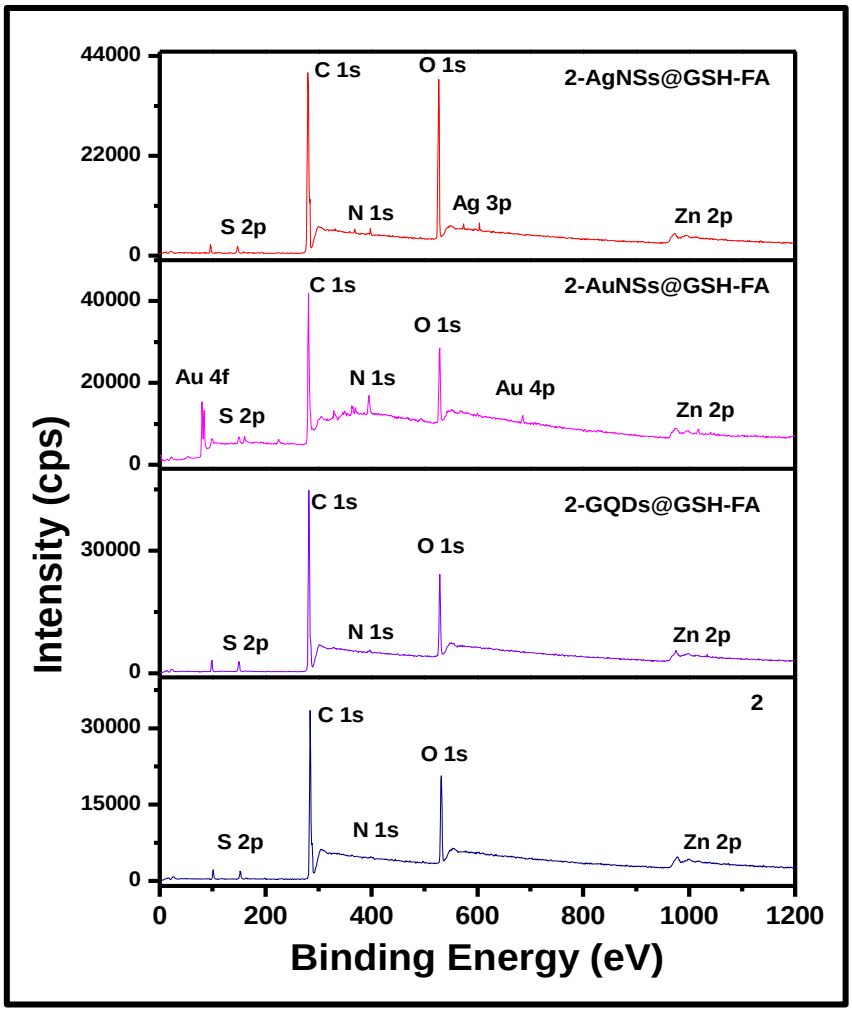

Figure 3.21: XPS spectra Survey spectra for complex **2**, **2**-GQDs@GSH-FA, **2**-AuNSs@GSH-FA and **2**-AgNSs@GSH-FA.

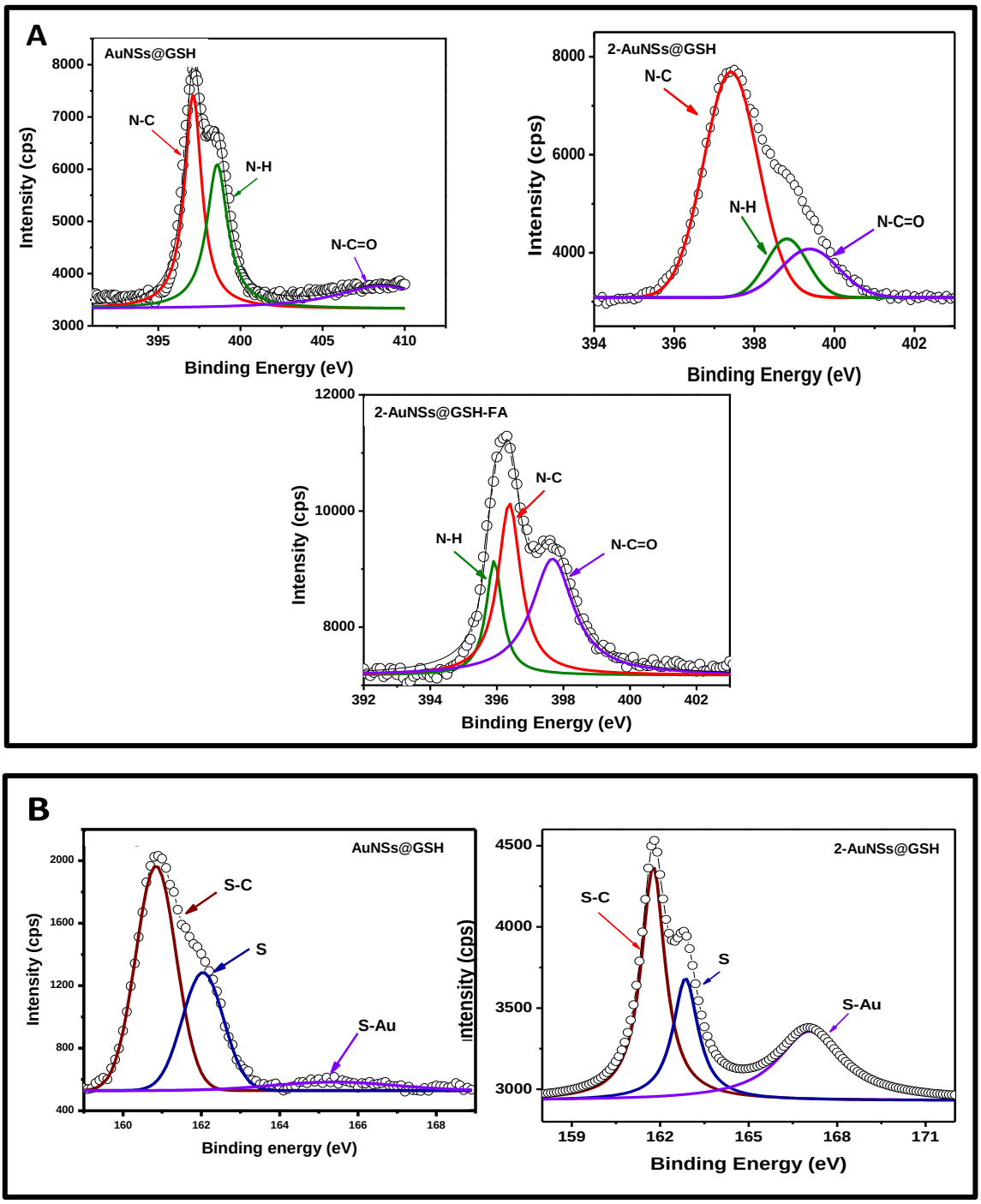

Figure 3.22: XPS high-resolution spectra for (A) N1s for AuNSs@GSH, 2-AuNSs@GSH and 2-AuNSs@GSH-FA, and (B) S 2p high-resolution spectra of AuNSs@GSH alone and the 2-AuNSs@GSH.

3.11 Summary of chapter

The synthesis and characterisation of novel hybrids containing GQDs, AuNPs and AgNPs with Pcs and BODIPY were presented. AuNPs and AgNPs showed their typical semi-crystalline diffraction patterns corresponding to the faced-centred cubic structure of metallic silver and gold, respectively, while the GQDs (either GQDs alone or GQDs@GSH) showed broad diffraction peaks at 2θ ~25^{o} which are due to (002) Bragg's reflection typical of carbon nanostructures. The synthesized BODIPY and Pc molecules showed monomeric behavior in DMSO. The various conjugates were prepared via covalent and non-covalent conjugation. GQDs, AuNSs and AgNSs were functionalized with L-glutathione (GSH) in order to assist coupling to the BODIPY and Pcs. XPS as well as FT-IR results confirmed the successful conjugation of Pcs and BODIPY to the different nanomaterials. The fabrication of conjugates was confirmed by TEM and the sizes of the respective nanoparticles were shown to increase upon conjugation to the respective complexes. In addition to this, the presence of both peaks from the Pc and gold nanoparticles in the XRD patterns confirmed the presence of the different Pcs and BODIPY complexes on the respective NPs in the conjugates. In general, the Pc conjugates showed relatively unchanged Q-band compared to the Pcs alone. They however showed enhancement in their absorption spectra below 600 nm owing the presence of BODIPY or the respective AuNPs, AgNPs or GQDs in the conjugates. Various other techniques were employed for their characterization and the results obtained confirmed fabrication of the respective conjugates with high colloidal stability implied by the zeta potential values obtained.

CHAPTER FOUR

PHOTOPHYSICS AND PHOTOCHEMISTRY

This chapter focusses on the photophysical and photochemical properties of phthalocyanines and BODIPY as well as the effect of AuNPs, AgNPs and GQDs on the photophysicochemical properties of the respective complexes. The photophysical and photochemical parameters of all complexes (**1**-**5**) as well as their respective conjugates were determined in DMSO.

4.1. Fluorescence quantum yields (Φ_F) and lifetimes (τ_F)

The Φ_F values of the quantum dots (GQDs), either metallophthalocyanines (Pcs) or BODIPY, and their conjugates were determined as described in the literatures **[107**], all in DMSO. The fluorescence lifetimes (τ_F) were determined using time correlated single photon counting set-up.

The fluorescence quantum yields of the GQDs/BODIPY in the conjugates $\Phi_{F(GQDs/BODIPY)}^{Conjugate}$ were calculated using **Eq. 4.1**.

$$\Phi_{F(GQDs/BODIPY)}^{Conjugate} = \Phi_{F(GQDs/BODIPY)} \frac{F^{Conjugate}}{F_{(GQDs/BODIPY)}} \quad \textbf{(4.1)}$$

where $\Phi_{F\ (GQDs)}$ is the fluorescence quantum yield of the GQDs alone and was used as a standard. $F_{\ (GQDs/BODIPY)}$ is the fluorescence intensity of the GQDs or BODIPY alone and $F^{Conjugate}$ is the fluorescence intensity of the GQDs/BODIPY when conjugated.

4.1.1 GQDs alone and with FA and other NPs

Fluorescence quantum yield for GQDs (both as pristine GQDs or modified GQDs) were evaluated by exciting where GQDs absorb (340 nm). Fluorescence quantum yield (Φ_F) for GQDs@GSH of 0.27 is within previously reported values for GQDs@GSH [**53**], **Table 4.1**. This value is greater than that observed for pristine GQDs of 0.1 (**Table 4.1**). Photoluminescence properties of GQDs have been linked to the presence of surface groups (hydroxyl and carboxyl) localized within the planes and dangling at the edges of the graphene-

like architecture of GQDs [**157**]. These groups and other intrinsic sites introduce surface defects, which facilitate the relaxation of excitons leading to radiative recombinations [**27**], hence fluorescence emission. The high Φ_F for GQDs@GSH compared to pristine GQDs suggests the formation of more defects in the presence of GSH in the former. The results as presented in **Table 4.1** show that the fluorescence of the GQDs@GSH was quenched in the presence of FA which was reflected in decreased in the fluorescence quantum yield of the resultant GQDs@GSH-FA to 0.21.

For all GQDs employed in this work, the fluorescence lifetimes (τ_F) were found to be single exponential decay (**Figure 4.1**). The fluorescence lifetimes of GQDs@GSH and GQDs@GSH-FA were longer than that for pristine GQDs corresponding to larger fluorescence quantum yields as discussed above, hence showing that the functionalization of GQDs affects their fluorescence properties (**Table 4.1**). The fluorescence lifetime of GQDs@GSH was found to be 3.4 ns, which was greatly reduced post conjugation to FA, corresponding to the decrease in Φ_F.

The results as presented in **Table 4.1** show reduction in the fluorescence quantum yield of the GQDs@GSH upon conjugation to the AuNPs from 0.27 (for GQDs@GSH) to 0.14, 0.15 and 0.17 for GQDs@GSH/AuNSs, GQDs@GSH/AuNRs (2.0), and GQDs@GSH/AuNRs (4.0), respectively. The fluorescence behaviour of the GQDs in the presence of the gold nanoparticles is affected by factors such as the size of the gold nanoparticle and the distance separating them [**32**]. This reduction in fluorescence is advantageous in areas such as SERS since fluorescence interference is often a severe problem often affecting Raman signaling. Fluorescence quantum yields and lifetimes (GQDs@GSH/AuNPs) were also slightly affected by the increasing aspect ratio of AuNPs. This observation is consistent with literature reports, where the degree of polarizability of nanorods increases with their aspect ratio [**168, 169**]. Hence, the trends in

fluorescence quantum yields of the GQDs@GSH/AuNPs conjugates could also be due to the increasing excitation rates of the AuNPs as the aspect ratio increases [**170**].

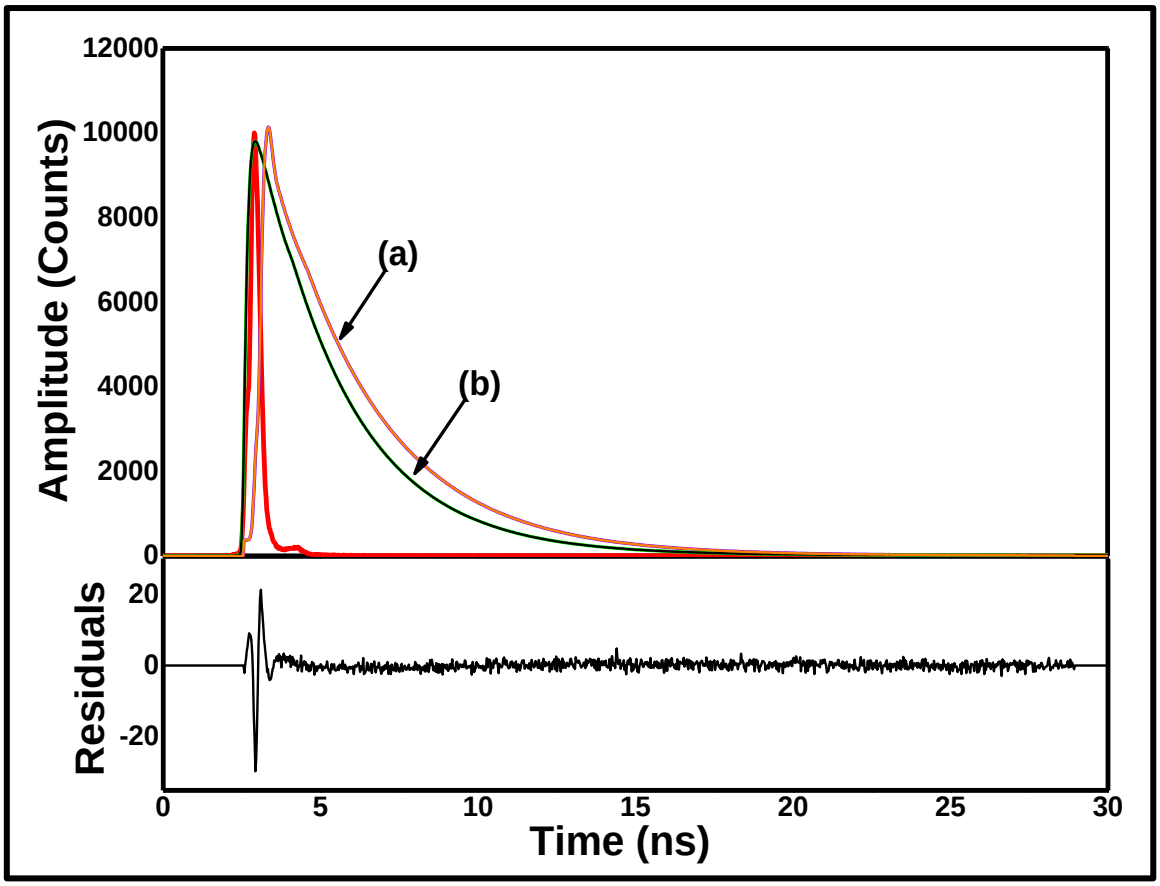

Figure 4.1: Fluorescence decay curve of GQDs@GSH (a) and 2-GQDs@GSH-FA (b) in DMSO at excitation wavelength of 485 and 670 nm, respectively.

Table 4.1: Photophysical parameters of graphene quantum dots (GQDs) in DMSO.

Compound	Φ_F (0.01)	τ_f (ns)
GQDs	0.1	1.2
GQDs@GSH	0.27	3.4
GQDs@GSH-FA	0.21	2.6
GQDs@GSH/AuNSs	0.14	0.43
GQDs@GSH/AuNRs (2.0)	0.15	0.45
GQDs@GSH/AuNRs (4.0)	0.17	0.49

4.1.2 MPcs and BODIPY alone.

The fluorescence quantum yields (Φ_F) of the respective complexes were determined following excitation at their respective absorption band crossover wavelengths with a suitable standard. **Table 4.2** summarizes the obtained results for all complexes synthesized in this work.

Complex **1** with the lighter aluminium metal showed higher Φ_F and τ_F values (0.30 and 5.0 ns, respectively) contrasted against its heavy zinc-metal counterparts. This could be attributed to the fact that heavier metals help induce spin-orbit coupling which in turn promotes faster intersystem crossing to the triplet state. For the zinc-based Pc complexes, the Φ_F for the asymmetrical Pc **4** (0.20) was determined to be much higher than those of complexes **2** and **3** (0.15 and 0.03, respectively), **Table 4.2**. This could be attributed to the lack of symmetry coupled with less deactivation of the excited singlet state of the former thereby encouraging less population at the triplet state. Symmetry is known to promote intersystem crossing to the triplet state [**171**], which usually results in lower Φ_F. For the BODIPY (**5**), the Φ_F was determined to be 0.85 (**Table 4.2**). Mono-exponential decay profiles were observed for all the MPcs and BODIPY, signifying monomeric forms in solution.

4.1.3 MPcs or BODIPY conjugates

A typical fluorescence decay curve for the **2**-GQDs@GSH-FA is shown in **Fig. 4.1** as an example. A mono exponential decay curve was observed for the conjugates. The observed decreases in Φ_F for **2** in the presence of AuNSs@GSH and AgNSs@GSH (**Table 4.2**) can be attributed to the heavy metal effect associated with nanoparticles, which promotes intersystem crossing to the triplet state, reducing fluorescence. For complexes **2**, **3** and **4,** there is insignificant change (or less change) in fluorescence quantum yields in the presence of GQDs owing largely to the lack of heavy metals. There is however, shortening of the fluorescence lifetime for conjugates compared to Pcs alone (except for conjugates of complex **1**). Literature

reports that excitation of a fluorophore in the presence of a nearby metal, may elicit the interaction of free electrons from the metallic surface with the fluorophore and modify the fluorescence behaviour by altering the electric field around the molecule [**172**]. This may give rise to the altering of the fluorescence lifetimes. This phenomenon (resulting in either an increase or decrease in the fluorescence lifetime) depends on the geometry or distance between the metal and molecule [**173,174**]. The observed decrease in fluorescence quantum yields and lifetimes could hence suggest close packing of the Pc on the surface of the nanoparticles. However, this does not apply to GQDs since they do not contain a metal.

GQDs fluorescence was quenched in the presence of all Pc complexes when exciting where the former absorbs. The decrease in fluorescence quantum yields of GQDs in the presence of Pcs could be due to Forster resonance energy transfer (FRET) and other processes which deactivates the excited states [**175**]. Both radiative and non-radiative processes compete in the de-excitation of the molecules. Non-radiative processes quench the fluorescence and decrease the decay times. The radiative lifetime (τ_0), which is the lifetime of the molecule in the absence of the non-radiative processes, can be used to explain the quenching of lifetimes. This lifetime is directly related to the radiative lifetime (τ_0), using fluorescence lifetime (τ_F) and fluorescence quantum yields (Φ_F) of the compounds, using the relationship ($\tau_0 = {}^{\tau_F}/_{\Phi_F}$).

All the Pc-NPs conjugates with high radiative lifetimes (**Table 4.2**) showed lower fluorescence quantum yields in accordance with the model, as observed for complexes **1-4**. As stated above, the geometry or distance between the metal and molecule can alter how they interact in a complex. Therefore, the excited molecule can be pictured as an oscillating dipole in which the lifetime will increase when the oscillating dipole is not in line with the reflected field and decreases when they correlate [**176,177**]. The observed increase in τ_0 values for **2** (**Table 4.2**) in the presence of AuNSs@GSH and AgNSs@GSH suggests an uncorrelated field between the

Pc and the AuNSs@GSH and AgNSs@GSH. When the conjugates were further linked to FA there is increases in τ_0 for **1** and decrease for **2**.

Table 4.2: Fluorescence quantum yield and lifetime parameters of the Pcs, BODIPY and the respective conjugates with GQDs, AuNPs and AgNPs in DMSO.

Compound	τ_0	Φ_F[a]	τ_f (ns)
1	16.7	0.30	5.0
1-GQDs	19.3	0.27 (0.09)	5.2
1-GQDs@GSH	26.1	0.23 (0.02)	6.0
1-GQDs@GSH-FA	27.7	0.22 (0.04)	6.1
2	25.5	0.15	3.82
2-AuNSs@GSH	46.0	0.06	2.74
2-AuNSs@GSH-FA	24.7	0.11	2.76
2-AgNSs@GSH	46.0	0.08	2.74
2-AgNSs@GSH-FA	19.6	0.14	2.77
2-GQDs@GSH	19.9	0.14 (0.19)	2.79 (2.42)
2-GQDs@GSH-FA	22.5	0.12 (0.16)	2.70 (2.21)
3	34	0.03	1.02

3-GQDs@GSH	**89.0**	**0.01** **(0.23)**	**0.89** **(2.84)**
BODIPY	**5.9**	**0.85**	**5.05**
BODIPY-GQDs@GSH	**8.1**	**0.60** **(0.02)**	**[4.85][b]**
3-BODIPY-GQDs@GSH	**78**	**<0.01** **[0.55]** **(0.10)**	**0.78** **[4.76][b]**
4	**16.6**	**0.20**	**3.33**
4-GQDs@GSH	**19.8**	**0.16** **(0.15)**	**3.16** **(2.10)**
4-GQDs@GSH-AuNSs	**39.7**	**0.07** **(0.06)**	**2.78** **(1.38)**

[a]Numbers in round brackets are for excitation where GQDs absorb, square brackets for BODIPY, the rest of the values are where respective complexes absorb. [b]The fluorescence lifetime represents both BODIPY and GQDs@GSH, since both were excited. The values for GQDs alone are listed in Table 4.1.

4.2 Triplet quantum yields (Φ_T) and lifetimes (τ_T)

Triplet quantum yield (Φ_T) represents the fraction of absorbing molecules that undergo intersystem crossing to the metastable triplet excited state. The triplet state quantum yields and lifetimes for all complexes and conjugates are shown in **Table 4.3**. The laser flash photolysis set-up was employed for the triplet state absorption measurements. Typical triplet decay curves of MPcs and their conjugates are shown in **Figure 4.2** using compound **4**, **4**-GQDs@GSH and **4**-GQDs@GSH-AuNSs as examples. The triplet decay curves obeyed second order kinetics which is typical of MPc complexes at high concentration (1×10^{-5} M) due to the triplet–triplet recombination [**178**]. Of all Pcs alone, complex **3** had the largest Φ_T value at 0.63, followed by **2** and **4** both at 0.59, and complex **1** had showed the lowest Φ_T at 0.38. The low value for **1** is due to the smaller Al central metal as discussed above. On conjugation, there is increase in all Φ_T values due to the heavy atom effect for the AuNPs and AgNPs conjugates. Moreover, Pcs are highly aromatic in nature and they interact strongly with GQDs by π-π stacking. Charge transfer processes which lead to the formation of excited-state radical ion pair in Pcs-carbon nanomaterial systems are known [**179**,**180**]. The presence of the FA also resulted in increased triplet state population of the respective Pcs (**1** and **2**), which could translate into higher photosensitizing ability. The τ_T values for all conjugates decrease with corresponding increasing Φ_T as expected. Intersystem crossing lifetimes τ_{isc} were evaluated using fluorescence lifetime (τ_F) and triplet quantum yields (Φ_T) of the compounds, using the relationship ($\tau_{isc} = {\tau_F}/{\Phi_T}$). There is an observed decrease in the τ_{isc} values for all conjugates compared to Pcs alone (**Table 4.3**).

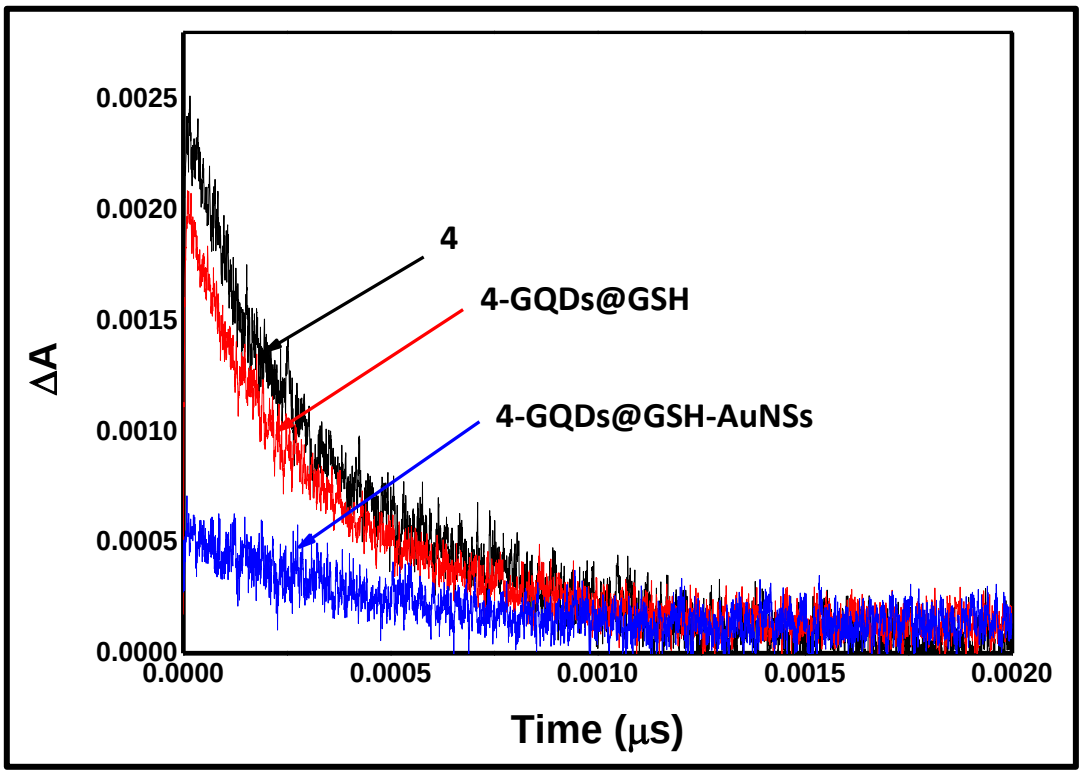

Figure 4.2: Representative excited state triplet absorption decay curves for 4 alone, 4-GQDs@GSH and 4-GQDs@GSH-AuNSs in DMSO at excitation wavelength of 674 nm.

4.3 Singlet oxygen quantum yield studies

The singlet oxygen quantum yield (Φ_Δ) was determined by the chemical photodegradation of singlet oxygen quencher (DPBF) in DMSO. Singlet oxygen is a product of efficient interaction of the triplet state of photosensitizer with the ground state molecular oxygen (resulting in energy transfer from the photosensitizer to the molecular oxygen). Irradiation of the main absorption bands of the complexes showed the stability of the complexes over the irradiation period. **Figures 4.3 (A)** and **(B)** show the singlet curves for the **2**-AuNSs@GSH-FA and **2**-GQDs@GSH-FA, respectively (as examples), showing changes in DPBF absorbances over time (**Figures 4.3 (A)** and **(B) (insets)**).

A significant increase in singlet oxygen generation was observed as evidenced by singlet oxygen quantum yield upon conjugation to the AuNSs@GSH, AgNSs@GSH and

GQDs@GSH with the **4**-GQDs@GSH-AuNSs having the highest singlet oxygen generation (**Table 4.3**) of all complexes. The high Φ_{Δ} correspond to high Φ_{T}. Amongst other factors, the efficiency of singlet oxygen generation depends on the energy, quantum yield and lifetime of the triplet state. The enhancement in singlet oxygen quantum yields in **Table 4.3** for all Pcs when conjugated to the NPs corresponds to the increase in triplet quantum yields. Upon conjugation of either **2**-AuNSs@GSH or **2**-AgNSs@GSH to FA, even greater enhancements in singlet quantum yields were observed with the **2**-AgNSs@GSH-FA having a quantum yield of 0.82 (**Table 4.3**). An increase in Φ_{Δ} in the presence of FA was also observed for complex **1**-GQDs@GSH-FA and **2**-NPs@GSH-FA. The Increased Φ_{Δ} in the presence of FA is important for biological applications. Furthermore, an enhancement in the singlet oxygen quantum yields for **3**-BODIPY-GQDs@GSH of 0.70 was observed (compared to **3**-GQDs@GSH with 0.58, **Table 4.3**) highlighting the possible advantages of the introduction of the BODIPY core to the GQDs structure. The increase in singlet oxygen quantum yields shows that the resultant conjugates may be used for PDT applications.

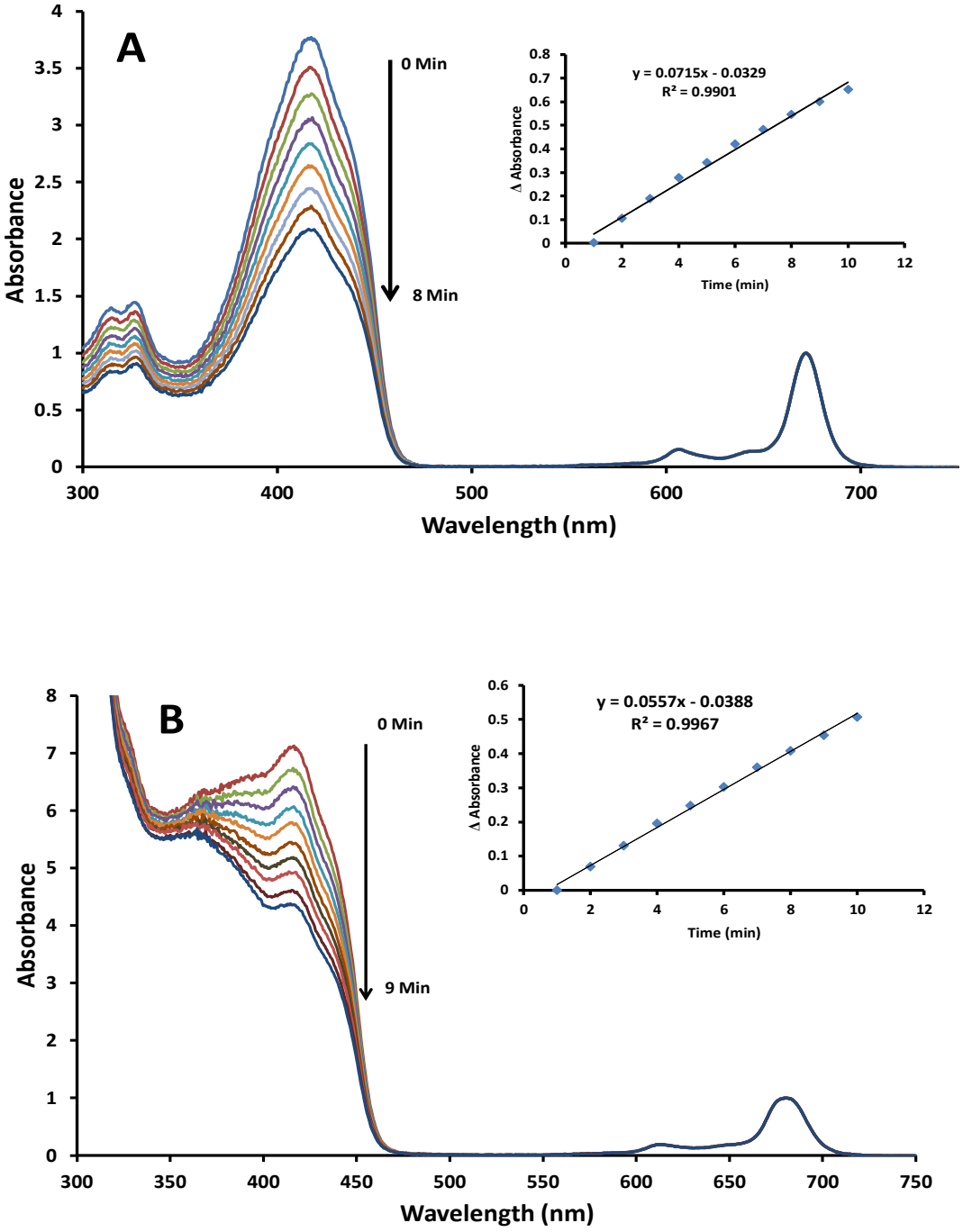

Figure 4.3: Sample spectra showing the generation of singlet oxygen using DPBF as a single oxygen quencher for 2-AuNSs@GSH-FA (A) and 2-GQDs@GSH-FA (B) both in DMSO. Insets: Change in DPBF absorbance over time.

Table 4.3: Triplet and singlet parameters of the complexes and respective conjugates.

Compound	τ_{isc} (ns)	Φ_T	τ_T (ns)	Φ_Δ
1	13.2	0.38	1335	0.37
1-GQDs	8.7	0.60	560	0.42
1-GQDs@GSH	8.0	0.75	270	0.52
1-GQDs@GSH-FA	8.1	0.75	240	0.54
2	6.5	0.59	347	0.32
2-AuNSs@GSH	4.3	0.64	300	0.60
2-AuNSs@GSH-FA	4.1	0.67	254	0.62
2-AgNSs@GSH	3.8	0.74	275	0.72
2-AgNSs@GSH-FA	3.3	0.85	240	0.82
2-GQDs@GSH	4.6	0.61	197	0.50
2-GQDs@GSH-FA	4.3	0.63	225	0.54
3	1.59	0.63	322	0.50
3-GQDs@GSH	1.33	0.67	221	0.58

BODIPY	**-**	**-**	**-**	**0.10**
BODIPY-GQDs@GSH	**-**	**-**	**-**	**0.28**
3-BODIPY-GQDs@GSH	**1.00**	**0.78**	**177**	**0.70**
4	**5.6**	**0.59**	**359**	**0.56**
4-GQDs@GSH	**4.8**	**0.67**	**309**	**0.65**
4-GQDs@GSH-AuNSs	**3.0**	**0.91**	**38**	**0.87**

4.4 Summary of chapter

The photophysics and photochemistry of the MPcs and BODIPY as well as their conjugates were studied in DMSO. All the studied conjugates exhibited good photophysicochemical behaviour with relatively high triplet and singlet quantum yields. The Pc macrocycles with heavy central metals (Zn) exhibited higher triplet and singlet quantum yields in comparison to the ones with relatively light metal (Al) prior to conjugation to NPs, and this could be due to the heavy-atom effect obtained from the former. For all MPcs, conjugation to NPs (either GQDs, AuNSs or AgNSs) resulted in a decrease in the fluorescence quantum yields. The conjugates also displayed higher triplet quantum yields, which translated into higher singlet oxygen quantum yields compared to complexes alone. In all cases, the presence of FA also resulted in higher singlet oxygen quantum yields for the Pcs, than without.

CHAPTER FIVE

SURFACE-ENHANCED RAMAN SCATTERING (SERS)

This chapter reports on the effect of AuNPs shape and aspect ratio on SERS activity of GQDs@GSH-AuNPs. It also discusses the design of novel Pcs/GQDs/AuNPs SERS agents, and describes the SERS behaviour of such potential Raman-active PDT agents for the first time.

5.1 Determination of the concentration of GQDs@GSH alone and in the conjugates (Estimated)

The volume of individual GQDs@GSH particles were determined from the sizes of GQDs@GSH (determined from DLS results) on the assumption of homogeneous GQDs@GSH (from AFM results) using equation **5.1**:

$$\text{Single Particle Volume (GQDs@GSH)} = \frac{4}{3}\pi r^3 \qquad \textbf{(5.1)}$$

To determine the volume of GQDs@GSH in solution, a 100 ml GQDs@GSH solution was weighed, and then dried to obtain the powder of GQDs@GSH (weighed before and after drying). The densities of both the solution and dried GQDs@GSH were determined. The total volume of GQDs@GSH in 100 ml solution was then determined using equation **5.2**.

$$\text{Total Volume (GQDs@GSH)} = \frac{Dry\ weigth\ of\ GQDs@GSH}{Density\ of\ GQDs@GSH\ (in\ solution)} \qquad \textbf{(5.2)}$$

The number of GQDs@GSH particles in solution was then determined using equation **5.3**.

$$\text{Number of Particles (GQDs@GSH)} = \frac{Total\ Volume\ (GQDs@GSH)}{Single\ Partcle\ Volume\ (GQDs@GSH)} \qquad \textbf{(5.3)}$$

Finally, using this value, the concentration of GQDs@GSH in solution was approximated using Avogadro's constant, N_A (6.0×10^{23}).

To appreciate the SERS effect, the enhancement factor (EF) of **4**-GQDs@GSH-AuNSs or GQDs@GSH/AuNPs when compared to GQDs@GSH alone or **4**-GQDs@GSH was quantitatively determined according to **Eq. 2.1**, now **Eq. 5.4** [**145**].

$$EF = \frac{I_{SERS}\, C_{Raman}}{I_{Raman} C_{SERS}} \qquad (5.4)$$

where I_{SERS} represents the Raman spectral intensities of GQDs@GSH/AuNPs or **4**-GQDs@GSH in the presence of AuNSs, while I_{Raman} represents spectral intensities of GQDs@GSH or **4**-GQDs@GSH alone. C_{Raman} is the estimated concentration of the GQDs@GSH alone and C_{SERS} represents estimated concentrations of GQDs@GSH in GQDs@GSH/AuNPs, **4**-GQDs@GSH and **4**-GQDs@GSH-AuNSs.

5.2 SERS Experiments

5.2.1 GQDs with AuNPs

AuNPs used in this sub-section are capped with CTAB and are thus, no longer stated for ease. **Fig. 5.1** shows the effect of the amounts of AuNSs and AuNRs on the SERS activity of the GQDs@GSH/AuNPs composites. At 1 mg/mL AuNPs, the enhancement factor (EF, calculated using **Equation 5.4**) is the same, but at 2 mg/mL the EF is smaller for AuNSs (with aspect ratio of 1.0), followed by AuNRs (2.0) and AuNRs (4.0). It has been reported that the AuNPs with the highest aspect ratio give higher SERS activity [**181**] as observed with 2 mg/mL of AuNPs in **Fig. 5.1**. However, experimental observations show that this theory is highly dependent on aggregation. Zeta potential measurements reported in previous chapters also showed more aggregation for the AuNSs (with the lower zeta potential) which is also in agreement with the lower fluorescence quantum yield for GQDs@GSH/AuNSs as aggregation affects fluorescence. The aggregation behaviour differences between spheres and rods are known to primarily be due to steric interaction and physical packing uniqueness, attributes that

are highly influenced by surface curvature [**182**]. The AuNSs with higher curvature, compared to the AuNRs with more longitudinal surfaces, are more prone to aggregation than the rods. Moreover, this higher curvature amongst spheres also influences the orientation of GQDs@GSH on the nanoparticle surfaces. The GQDs@GSH will most likely be compressed on the GQDs@GSH/AuNSs surfaces as compared to an extended brush-like layer for AuNRs. This compressed conformation of the adsorbed GQDs@GSH invariably is more prone to aggregating than the conformation in AuNRs. A similar observation has been reported for AuNPs decorated with poly acrylic acid (PAA) [**183**].

The results suggest that the interplay nanoparticle shape and resultant aggregation may have resulted in the observed EF values. The SERS effects of AuNPs therefore is not only dependent on mere simple nanoparticle plasmons as was previously thought. Aggregation is a well-known factor that can greatly affect SERS activity of nanostructures [**184-186**], where aggregating agents are commonly employed to aggregate different irregular nanoparticles in order to improve their SERS activity. This is because it leads to increased interactions between the colloid particles, affording larger surface plasmon resonances and greater surface enhancement. However, in cases where extensive aggregation occurs, the colloid particles will quickly precipitate out of solution and the SERS signal will be lost [**187,188**] and SERS activity begins to rapidly decrease, as was observed (**Fig. 5.1**).

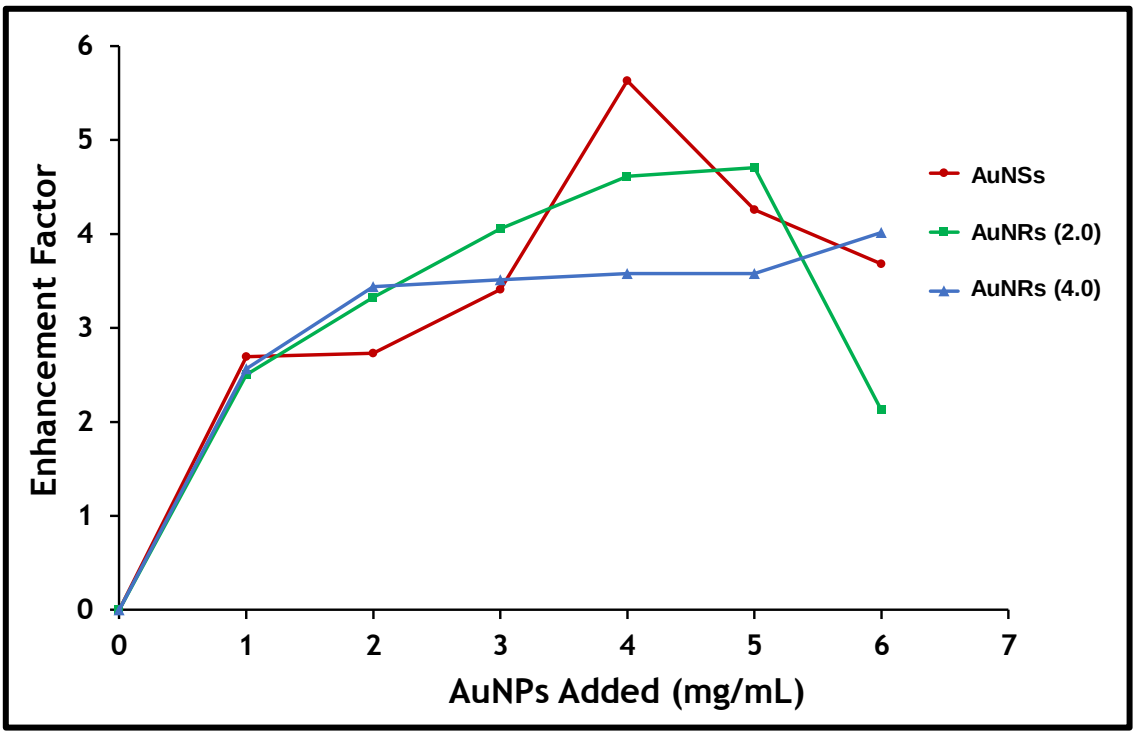

Figure 5.1: Enhancement factor of the nanocomposites of GQDs@GSH (at 1 mg/mL) with AuNSs, AuNRs (2.0), and AuNRs (4.0) showing SERS activity as a function of concentration of the AuNPs added to form the composite.

5.2.2 Pcs/GQDs/AuNPs composites

Figure 5.2 shows the Raman spectra of GQDs@GSH alone, **4**-GQDs@GSH and **4**-GQDs@GSH-AuNSs. As expected, highly enhanced Raman peaks with good signal-to-noise ratio were observed for **4**-GQDs@GSH-AuNSs as opposed to GQDs@GSH alone (**Fig. 5.2**), with vibrational frequencies comparable to those of GQDs@GSH. The Raman spectra of the GQDs@GSH alone (**Figure 5.2**) shows the peaks associated with primary amides (-NH_2 stretches) found at 3371 and 3251 cm^{-1} [**189**]. The disappearance of the NH_2 bands in the conjugate further serves as proof of successful conjugation of complex **4** to GQDs@GSH (**Fig 5.2**). It also shows the presence of a peak at 2552 cm^{-1} attributable to the S-H bond stretch [**190**], which is not observed following the assembly of AuNSs (**Figure 5.2**). There is an

appearance on a new peak at 306 cm^{-1} attributable to the S-Au bond [**190-192**], confirming the successful assembly of AuNSs on the Pcs/GQDs@GSH platform. An overall 32-fold enhancement was observed based on D-band analysis (**Fig. 5.2**). This unprecedented increase in the Raman signal of **4**-GQDs@GSH-AuNSs (compared to that of either **4**-GQDs@GSH or GQDs@GSH alone) could be attributed to the fact that colloidal metal nanostructures such as can be found in **4**-GQDs@GSH-AuNSs are known to give rise to local electromagnetic fields normally referred to as electromagnetic 'hot-spots', which result in significantly enhanced Raman signals. Hot spots in graphitic structures may also result due to the presence of C-O bonds, which provide active sites for the adsorption metal atoms or clusters. This, together with the low fluorescence of the composites are reasonable explanations for the impressive enhancements seen in the GQDs/Pcs/AuNPs hybrid.

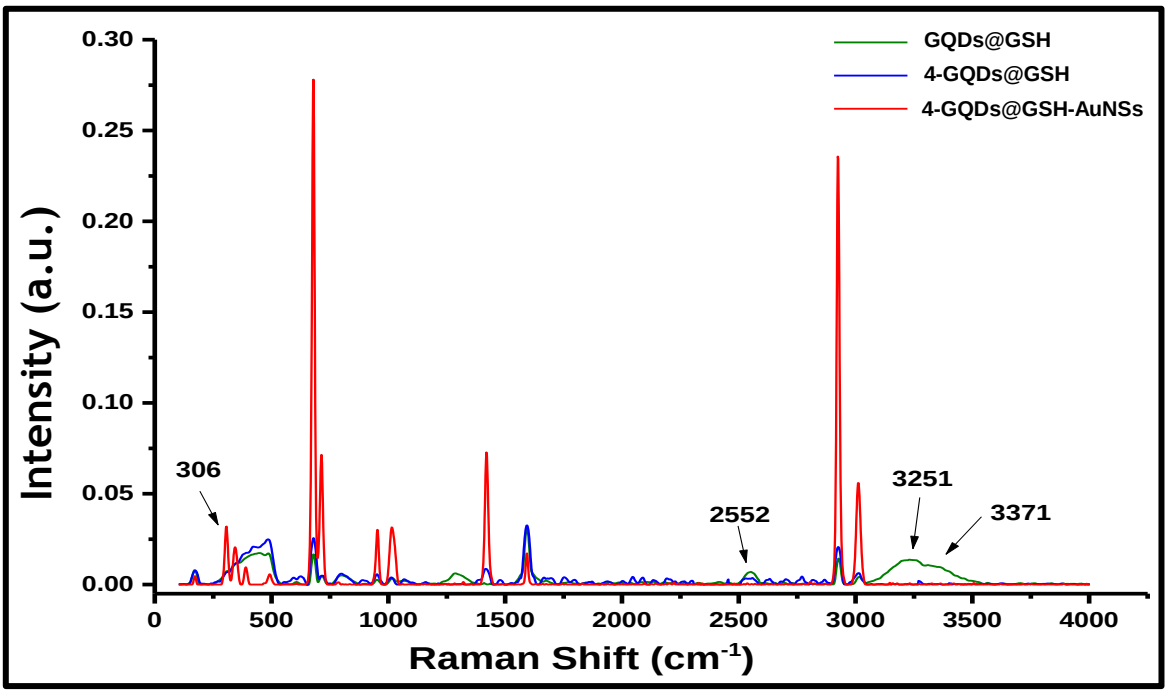

Figure 5.2: Raman spectra of 1 mg/mL each of GQDs@GSH alone, 4-GQDs@GSH and 4-GQDs@GSH-AuNSs composites showing that the AuNPs were formed on the sulphur containing Pcs/GQDs@GSH nanoplatform. This resulted in the observed enhancement of the Raman properties of the Pc/GQDs complexes, afforded by the successful chemisorption of the AuNSs.

5.2.3 Reproducibility of SERS signals

The SERS signal of **4**-GQDs@GSH-AuNSs (as an example) was examined in order to ascertain the uniformity and reproducibility of composites by recording their Raman signals 7 days after preparation. The relative standard deviation (RSD) was calculated to be about 1.01 % (using the D-band) evidencing the excellent SERS signal uniformity and reproducibility of Raman signals obtained (**Figure 5.3**).

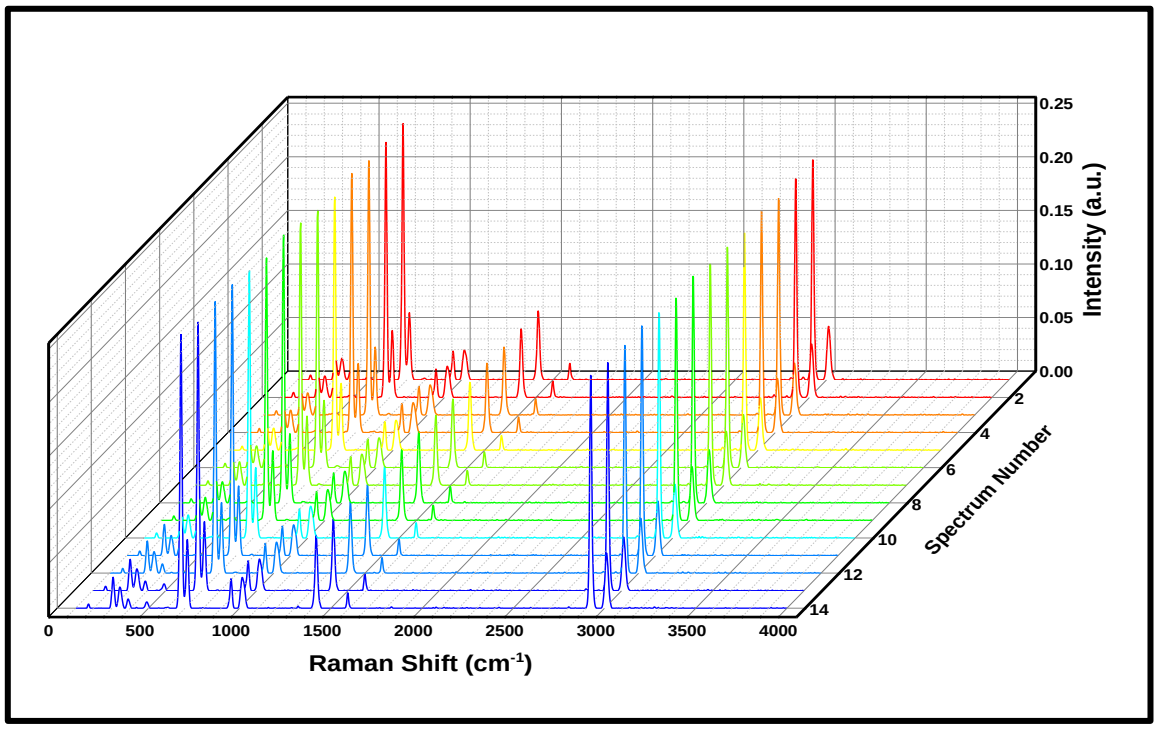

Figure 5.3: Raman spectrum of 4-GQDs@GSH-AuNSs showing the high reproducibility of Raman signals of 4-GQDs@GSH-AuNSs with RSD of 1.01 %. 14 Raman measurements were taken after 7 days of storage without any marked differences in the Raman positions or peak intensities.

5.3 Summary of chapter

The dependence of the SERS activity of gold nanoparticles on their aspect ratio and shape was investigated using GQDs@GSH as probe molecule. SERS properties of AuNPs assembled onto functional graphene quantum dots-phthalocyanines (GQDs@GSH/Pcs) arrays are also presented. Results highlight, for the first time that at higher concentrations, unlike what was previously believed, SERS activity becomes less positively correlated to increases in aspect ratio of AuNPs and that aggregation becomes the prevailing factor affecting SERS activity though further studies may need to be carried out to properly quantify this contribution.

This work also demonstrated strong SERS properties achievable by combining the intrinsic properties of Pcs, GQDs@GSH and AuNPs with an unprecedented intrinsic maximal enhancement factor of more than 30-fold. The observed Raman enhancement can be explained to have resulted from the AuNPs being chemisorbed unto the GQDs@GSH/Pcs hybrid. These nanostructures also displayed very stable and reproducible Raman signals. These results highlight the remarkable potential of this composite as unique Raman-based PDT dosimetric agents.

CHAPTER SIX

GENERAL CONCLUSIONS AND FUTURE PROSPECTS

This chapter gives a general summary of the work detailed in this thesis, future prospects and direction.

6.1 Conclusions

The successful synthesis and characterization of phthalocyanines (Pcs), BODIPY as well as GQDs, AuNPs and AgNPs is presented in this research work. Conjugates were formed either via π-π interactions or by taking advantage of GSH functionality which allows for amide bond formations. The morphologies of the NPs and their conjugates were assessed using transmission electron microscopy and X-ray diffraction. The results obtained from DLS and zeta potential experiments are in accordance with results well-documented in the literature for GQDs and functionalized GQDs. FT-IR and X-ray photoelectron spectra were used to confirm the successful formation of the amide bond between the Pcs or BODIPY and NPs, hence formation of the respective conjugates. Through correlation between the structural characterization of each individual complex and conjugates with either GQDs, AuNPs or AgNPs using microscopic techniques such as TEM, EDS and AFM, as well as their optical, photophysical and photochemical properties, this work reports huge improvements in the triplet state parameters of complexes that resulted from combining them with nanomaterials (metallic and carbon based). For all complexes, there were drastic reductions in fluorescence quantum yields upon conjugation to the NPs, which translated into significantly higher singlet oxygen quantum yields for the respective conjugates. Post folic acid introduction, triplet state parameters of the conjugates were further enhanced. Thus, the results highlight the importance of FA in Pcs conjugates. The increased singlet oxygen generation of the conjugates in the presence of FA therefore presents the possibility for new generation of Pc-based conjugates to be useful for targeted-PDT applications.

Results from SERS experiments show that AuNPs decorated with GQDs gain an excellent SERS ability suggesting a significant chemical interaction between the Au nanoparticles and the GQDs. Results indicate that GQDs decorated AuNSs have higher aggregation propensity compared to anisotropic AuNRs, as observed from the zeta potential values. The geometric differences between the AuNPs resulted in unique conformation of the GQDs onto their surfaces. This resulted in differences in steric hindrances, hence yielding the respective SERS activity of the different conjugates, with AuNSs possessing the highest SERS activity. The observations suggest that for AuNPs, SERS activity cannot simply be explained on the basis of the relative plasmonic behaviour of the respective noble nanoparticles as was previously believed, an observation likely to be of crucial importance for other plasmonic applications.

Results further highlight that the novel nanocomposites herein reported, (by combining the intrinsic properties of Pcs, GQDs@GSH and AuNPs) resulted in even greater Raman scattering properties. With an unprecedented intrinsic maximal enhancement factor of more than 30-fold, this work demonstrates that such nanostructures also retain more than 90% of their original SERS intensities after a week of storage, displaying superb stability under ambient conditions. This work therefore demonstrated for the first time, the possibility of both efficient singlet oxygen generation and significant Raman scattering potential in a nanosystem, demonstrating its potential as a novel PDT dosimetric agent.

6.2 Future Prospects

While this work has successfully demonstrated the effect of GQDs, in the design of potential PDT agents with a full photophysical work-up, it will be noble to investigate the effect doping of the GQDs with metallic and non-metallic heteroatoms to probe the effect that this may have on the photophysical properties of such conjugates with Pcs. Upon conjugation to GQDs and FA, there were huge improvements in the water solubility of the conjugates herein reported. As a result, the evaluation of the photophysical and photochemical properties of these conjugates in aqueous media to confirm that these conjugates can be applied in biological environments could prove crucial in PDT. The use of GQDs in SERS is a promising and fast growing field hence, the development of novel Raman active-PDT agents is crucial. GQDs have captured a lot of attention due to their biocompatibility and unique Raman properties. The coupling of other carbon based nanoparticles could prove an important research area in the areas of theranostics and PDT dosimetry.

REFERENCES

1. A. B. P. Lever, H. J. Emeleus, A. G. Sharpe (Eds), In: Advances in Inorganic Chemistry and Radiochemistry, Academic Press, New York, 7 (1965) 28.
2. N. B. McKeown, In: Phthalocyanine Materials-Synthesis, Structure and Function, Cambridge University Press, 1998.
3. K. Kadish, Kevin M. Smith, Roger Guilard (eds), In The Porphyrin Handbook, Academic Press, San Diego CA, USA, 15 (2003).
4. F. H. Moser, A.I. Thomas, In: The Phthalocyanines Manufacture and Application, CRC Press, Boca Raton FL, 2 (1983).
5. C. W. Foster, J. Pillay, J. P. Metters, C.E. Banks, Sensors (Switzerland), 14 (2014) 21905.
6. S. Griveau, M. Gulppi, J. Pavez, J. H. Zagal, F. Bedioui, Electroanalysis, 15 (2003) 779.
7. J. Pillay, S. Vilakazi, J. Porphyrins Phthalocyanines, 16 (2012) 785.
8. I. Okura. Photosensitization of Porphyrins and Phthalocyanines Gordon and Breach Publishers, Germany, 2001.
9. E. V. Filonenko, V. V. Sokolov, V. I. Chissov, E. A. Lukyanets, G. N. Vorozhtsov. Photodynamic therapy of early esophageal cancer. Photodiagn. Photodyn. Ther., 5 (2008) 187.
10. R. Bonnett, Chemical Aspects of Photodynamic Therapy. Gordon and Breach Science Publishers, Amsterdam, 2000.
11. A. Ogunsipe, J. Chen, T. Nyokong, New J. Chem., 28 (2004) 822.
12. M. Özçeşmeci, İ. Özçeşmeci, E, Hamuryudan, Polyhedron, 29 (2010) 2710.
13. S. K. Das, N. K. Subbaiyan, F. D'souza, A. S. Sandanayaka, T. Wakahara, O. Ito, J. Porphyrins Phthalocyanines, 15 (2011) 1033.

14. G. Bottari, G. de la Torre, D. M. Guldi, T. Torres, Chem. Rev., 110 (2010) 6768.
15. C. C. Leznoff, C. R. McArthur, Y. Qin, Can. J. Chem., 71 (1993) 1319.
16. S. V. Kudrevich, H. Ali, J. E. van Lier, J. Chem. Soc. Perkin Trans., 1 (1994) 2767.
17. T. Torres, J. Porphyrins Phthalocyanines, 4 (2000) 325
18. N. Kobayashi, R. Kondo, S. Nakajima, T. J. Osa, Am. Chem. Soc., 112 (1990) 9640.
19. C. C. Byeon, M. M. McKerns, W. Sun, T. M Nordlund, C. M Lawson, G. M Gray, Appl. Phys. Lett., 84 (2004) 5174.
20. G. de la Torre, C. G. Claessens, T. Torres, Chem. Commun., (2007) 2000.
21. A.M. Paoletti, G. Pennesi, G. Rossi, A. Generosi, B. Paci, V.R. Albertini, Sensors, 9 (2009) 5277.
22. A. M. Schaffer, M. Gouterman, E. R. Davidson, Theoret. Chim. Acta, 30 (1973) 9.
23. J. McHugh, M. Gouterman, C. Weiss, Theoret. Chim. Acta, 24 (1987) 246.
24. M. Gouterman, In the Porphyrins, (Ed. D. Dolphin), Part A. Physical Chemistry, Academic Press, New York, 1978.
25. J. Park, J. Joo, S. G. Kwon, Y. Jang, T. Hyeon, Angew. Chem. Int. Ed., 46 (2007) 4630.
26. C. P. Poole, F. J. Owens, Introduction to nanotechnology. Hoboken, John Wiley and Sons, New Jersey, 2003.
27. S. Benítez-Martínez, M. Valcárcel, Trends Anal. Chem., 72 (2015) 93.
28. J. M. Tsay, X. Michalet, Chem Biol., 12 (2005) 1159.
29. P. Juzenas, W. Chen, Y. Sun, M. A. N. Coelho, R. Generalov, N. Generalova, I. L. Christensen, Adv. Drug. Deliv. Rev., 60 (2008) 1600.
30. L. A. Ponomarenko, F. Schedin, M. I. Katsnelson, E. W. Hill, K. S. Novoselov, A. K. Geim, Science, 320 (2008) 356.
31. D. Pan, C. Xi, Z. Li, L. Wang, Z. Chen, B. Lu, M. Wu, J. Mater. Chem. A, 1 (2013) 3551.

32. X. Yan, X. Cui, B. S. Li, L.S. Li, Nano Lett., 10 (2010) 1869.

33. J. Zhao, G. Chen, L. Zhu, G. Li, Electrochem. Commun., 13 (2011) 31.

34. H. Razmi, R. Mohammad-Rezaei, Biosens. Bioelectron., 41 (2013) 498.

35. J. Shen, Y. Zhu, X. Yang, J. Zong, J. Zhang, C. Li, New J. Chem., 36 (2012) 97.

36. J. Ge, M. Lan, B. Zhou, W. Liu, L. Guo, H. Wang, Q. Jia, G. Niu, X. Huang, H. Zhou, X. Meng, P. Wang, C. S. Lee, W. Zhang, X. Han, Nat. Commun., 5 (2014) 4596.

37. J. Peng, W. Gao, B. K. Gupta, Z. Liu, R. Romero-Aburto, L. Ge, L. Song, L. B. Alemany, X. Zhan, G. Gao, A. S. Vithayathil, B. A. Kaipparettu, A. A. Marti, T. Hayashi, J. J. Zhu, P. M. Ajayan, Nano Lett., 12 (2012) 844.

38. Y. Dong, C. Chen, X. Zheng, L. Gao, Z. Cui, H. Yang, C. Guo, Y. Chi, M. C. Li, J. Mater. Chem., 22 (2012) 8764.

39. D. Pan, J. Zhang, Z. Li, M. Wu, Adv. Mater., 22 (2010) 734.

40. Q. Liu, B. Guo, Z. Rao, B. Zhang, J. R. Gong, Nano Lett., 13 (2013) 2436.

41. H. Tetsuka, R. Asahi, A. Nagoya, K. Okamoto, I. Tajima, R. Ohta, A. Okamoto, Adv. Mater., 24 (2012) 5333.

42. F. Liu, M. H. Jang, H.D. Ha, J. H. Kim, Y. H. Cho, T. S. Seo, Adv. Mater., 25 (2013) 3657.

43. S. Chen, J. Liu, M. Chen, X. Chen, J. Wang, Chem. Commun., 48 (2012) 7637.

44. Y. Dong, J. Shao, C. Chen, H. Li, R. Wang, Y. Chi, X. Lin, G. N. Chen, Carbon, 50 (2012) 4738.

45. P. L. Choyke, H. Kobayashi, Abdom. Imaging, 31 (2006) 224.

46. Y. Li, Y. Zhao, H. Cheng, Y. Hu, G. Shi, L. Dai, L. Qu, J. Am. Chem. Soc., 134 (2012) 15.

47. C. Hu, Y. Liu, Y. Yang, J. Cui, Z. Huang, Y. Wang, L. Yang, H. Wang, Y. Xiao, J. Rong, J. Mater. Chem. B, 1 (2013) 39.

48. Y. Dong, H. Pang, H. B. Yang, C. Guo, J. Shao, Y. Chi, C. M. Li, T. Yu, Angew. Chem. Int. Ed., 52 (2013) 7800.
49. P. Luo, Z. Ji, C. Li, G. Shi, Nanoscale, 5 (2013) 7361.
50. W. Kwon, Y. Kim, C. Lee, M. Lee, H. C. Choi, T. Lee, S. W. Rhee, Nano Lett., 14 (2014) 1306.
51. X. Li, S. Zhu, B. Xu, K. Ma, J. Zhang, B. Yang, W. Tian, Nanoscale, 5 (2013) 7776.
52. B. Sapkota, A. Benabbas, H. Y. G. Lin, W. Liang, P. Champion, M. Wanunu, ACS Appl. Mater. Interfaces, 9 (2017) 9378.
53. J. Liu, X. Zhang, Z. Cong, Z. Chen, H. Yang, G. Chen, Nanoscale, 5 (2013) 1810.
54. S. Wang, L. Zachary, S. C. Ivan, Q. Li, RSC Adv., 5 (2015) 41248.
55. J. Turkevich, P. C. Stevenson, J. Hillier, Discuss. Fara. Soc., 11 (1951) 55.
56. X. Liu, M. Atwater, J. Wang, Q. Dai, J. Zou, J. P. Brennan, Q. Huo, J. Nanosci. Nanotechnol., 7 (2007) 3126.
57. X. Huang, S. Neretina, M.A. El-Sayed, Adv. Mater., 21 (2009) 4880.
58. J. Caoa, T. Suna, K. T.V. Grattan, Sens. Actuators B, 195 (2014) 332.
59. R. E. Messersmith, G. J. Nusz, S. M. Reed, J. Phys. Chem. C, 117 (2013) 26725.
60. S. Link, M.A. El-Sayed, J. Phys. Chem. B, 109 (2005) 10531.
61. T. M. Fahmy, P. M. Fong, A. Goyal, W. M. Saltzman, Mat. Today, 8 (2005) 18.
62. E. Roger, S. Kalscheuer, A. Kirtane, B. R. Guru, A. E. Grill, J. Whittum-Hudson, J. Panyam, Mol. Pharmaceutics, 9 (2012) 2103.
63. M. Fenech, Mutat. Res., 475 (2001) 57.
64. J. Sudimack, R. J. Lee, Adv. Drug Deliv. Rev., 41 (2000) 147.
65. O. Issarachot, J. Suksiriworapong, M. Takano, R. Yumoto, V. B. Junyaprasert, J. Nanopart. Res., 16 (2014) 2276.

66. C. Carbone, A. Campisi, T. Musumeci, G. Raciti, R. Bonfanti, G. Puglisi, European J. Pharm. Sci., 52 (2014) 12.
67. A. Treibs, F. H. Kreuzer, Lieb. Ann. Chem., 718 (1968), 208.
68. G. Ulrich, R. Ziessel, A. Harriman, Angew. Chem. Int. Ed., 47 (2008) 1184.
69. J. H. Boyer, A. M. Haag, G. Sathyamoorthi, M. L. Soong, K. Thangaraj, T. G. Pavlopoulos, Heteroat. Chem., 4 (1993) 39.
70. X. Jia, X. Yu, X. Yang, J. Cui, X. Tang, W. Liu, W. Qin, Dyes Pigm., 98 (2013) 195.
71. N. Adarsh, R. R. Avirah, D. Ramaiah, Org. lett., 12 (2010) 5720.
72. Z. Wang, X. Hong, S. Zong, C. Tang, Y. Cui, Q. Zheng, Sci. Rep., 5 (2015) 12602.
73. N. Shivran, M. Tyagi, S. Mula, P. Gupta, B. Saha, B. S. Patro, S. Chattopadhyay, Eur. J. Med. Chem., 122 (2016) 352.
74. Y. Yang, L. Zhang, C. Gao, L. Xu, S. Bai, X. Liu, RSC Adv., 4 (2014) 38119.
75. A. Loudet, K. Burgess, Chem. Rev., 107 (2007) 4891.
76. F. L. Arbeloa, J. Bañuelos, V. Martínez,T. Arbeloa, I. L. Arbeloa, Int. Rev. Phys. Chem., 24 (2005) 339.
77. F. L. Arbeloa, T. L. Arbeloa, I. L. Arbeloa, I. García-Moreno, A. Costela, R. Sastre, F. Amat-Guerri, Chem. Phys., 236 (1998) 331.
78. O. J. Achadu, T. Nyokong, Dyes Pigm., 145 (2017) 189.
79. O. J. Achadu, T. Nyokong, Anal. Chim. Acta, 991 (2017) 113.
80. O. J. Achadu, T. Nyokong, Talanta, 166 (2017) 15.
81. O. J. Achadu, T. Nyokong, Spectrochim. Acta A, 174 (2017) 339.
82. O. J. Achadu, T. Nyokong, New J. Chem., 41 (2017) 1447.
83. S. Centane, O. J. Achadu, T. Nyokong, Electroanalysis, 29 (2017) 2470.
84. R. Matshitse, K. E. Sekhosana, O. J. Achadu, T. Nyokong, J. Coord. Chem., 70 (2017) 3308.

85. T. Mthethwa, T. Nyokong, J. Lumin., 157 (2015) 207.

86. S. D'Souza, P. Mashazi, J. Britton, T. Nyokong, Polyhedron, 99 (2015) 112.

87. O. M. Bankole, O. Osifeko, T. Nyokong, J. Photochem. Photobiol. A, 329 (2016) 155.

88. O. M. Bankole, T. Nyokong, J. Mol. Str., 1136 (2017) 309.

89. N. Nombona, K. Maduray, E. Antunes, A. Karsten, T. Nyokong, J. Photochem. Photobiol. B: Biol., 107 (2012) 35.

90. A. N. Gowda, M. Kumar, A.R. Thomas, R. Philip, S. Kumar, ChemistrySelect, 1 (2016) 1361.

91. H. G. Baldovi, V.M. Blas-Ferrando, J. Ortiz, H. Garcia, F. Fernandez- Lazaro, A. Sastre-Santos, Chem. Phys. Chem., 17 (2016) 1579.

92. S. Wang, J. Wang, J. Chen, J. Mater. Chem. B, 2 (2014) 1594.

93. P. Khoza, E. Antunes, J. Chen, T. Nyokong, J. Lumin., 134 (2013) 784.

94. N. Nombona, W. Chidawanyika, T. Nyokong, Polyhedron, 30 (2011) 654.

95. Y. Zheng, S. Chen, B. Zheng, M. Ke, J. Huang, Chem. Lett., 43 (2014) 1701.

96. O. M. Bankole, T. Nyokong, J. Photochem. Photobiol. A, 319 (2016) 8.

97. S. Osati, H. Ali, E. Johan, V. Lier, Tetrahedron Lett., 56 (2015) 2049.

98. H. Yanik, M. Göksel, S. Yeşilot, M. Durmuş, Tetrahedron Lett., 57 (2016) 2922.

99. C. Gol, M. Malkoç, S. Yesilot, M. Durmus, Dyes Pigm., 111 (2014) 81.

100. K. Sakamoto, E. Ohno. Prog. Org. Coat., 31 (1997) 139.

101. N. Nwaji, T. Nyokong, J. Lumin., 192 (2017) 1167.

102. D. Dei, G. Chiti, M. P. De Filippis, L. Fantettia, F. Giuliani, F. Giuntini, M. Soncin, G. Jori, G. Roncucci, J. Porphyrins Phthalocyanines, 10 (2006) 147.

103. S. Bondock, W. Fadaly, M. A. Metwally, Eur. J. Med. Chem., 45 (2010) 3692.

104. V. S. Padalkar, V. D. Gupta, K. R. Phatangare, V. S. Patil, P. G. Umape, N. Sekar, J. Saudi Chem. Soc., 18 (2011) 262.

105. J. Cai, M. Sun, X. Wu, J. Chen, P. Wang, X. Zong, M. Ji, Eur. J. Med. Chem., 263 (2013) 702.

106. P. Suppan, Chemistry and Light, Royal Society, Cambridge, 1st ed., 1994.

107. J. R. Lakowicz, Principles of Fluorescence Spectroscopy, 3rd ed., Springer Science Business Media, LCC, New York, 2006.

108. H. De Vries, D. A. Wiersma, J. Chem. Phys., 70 (1979) 5807.

109. S. Fery-Forgues, D. Lavabre, J. Chem. Educ., 76 (1999) 1260.

110. A. Harriman, M.C. Richoux, J. Chem. Soc. Faraday Trans. II, 76 (1980) 1618.

111. A. M. Brouwer. Standards for photoluminescence quantum yield measurements in solution (IUPAC Technical Report). Pure Appl. Chem., 83 (2011) 2213.

112. J. W. Boag, J. Photochem. Photobiol, 8 (1968) 565.

113. T. H. Tran-Thi, C. Desforge , C. Thiec, S. J. Gaspard, Phys. Chem., 93 (1989) 1226.

114. R. Schmidt, J. Photochem. Photobiol., 82 (2006) 1161.

115. M. C. DeRosa, R. J. Crutchley, Coord. Chem. Rev., 234 (2002) 351.

116. T. Tørring, S. Helmig, P. R. Ogilby, K. V. Gothelf, Acc. Chem. Res., 47 (2014) 1799.

117. T. Nyokong, E. Antunes, In The Handbook of Porphyrin Science, Kadish, K. M. Smith, R. M. Guilard R. (Eds.) World Scientific, Singapore, 7, 2010.

118. H. Lu. J. Mack, Y. Yang, Z. Shen, Chem. Soc. Rev., 43 (2014) 4778.

119. M. T. Jarvi, M. S. Patterson, B. C. Wilson, Biophys. J., 102 (2012) 661.

120. N. Nombona. K. Maduray, E. Antunes, A. Karsten, T. Nyokong, J. Photochem. Photobiol. B, 107 (2012) 35.

121. O. Osifeko, T. Nyokong, Dyes Pigm., 131 (2016) 186.

122. J. P. Celli, B. Q. Spring, I. Rizvi, C. L. Evans, K. S. Samkoe, S. Verma, B. W. Pogue, T. Hasan, Chem. Rev., 10 (2010) 2795.

123. B. C. Wilson, M. S. Patterson, L. Lilge, Lasers Med. Sci., 12 (1997) 182.

124. M. K. Michele, A. Darafsheh, M. Ahmad, C. J. Finlay, C. T. Zhu, Proc. SPIE. Int. Soc. Opt. Eng., 9694 (2016) 96940.

125. E. F. Silva, F. A. Schaberle, C. J. Monteiro, J. M. Dąbrowski, L. G. Arnaut, Photochem. Photobiol. Sci., 7 (2013) 1187.

126. Z. Huang, H. Xu, D. A. Meyers, A. I. Musani, L. Wang, R. Tagg, A. B. Barqawi, Y. K. Chen, Technol. Cancer Res. Treat., 7 (2008) 309.

127. A. Farhadi, Á. Roxin, B. C. Wilson, G. Zheng, Theranostics, 5 (2015) 469.

128. S. Pang, T. Yang, L. He, Trends Anal. Chem., 85 (2016) 73.

129. G. Lu, C. Li, G. Q. Shi, Chem. Mater., 19 (2007) 3433.

130. W. Xu, X. Ling, J. Xiao, M. S. Dresselhaus, J. Kong, H. Xu, Z. Liu, J. Zhang, Proc. Natl. Acad. Sci. U. S. A., 109 (2012) 9281.

131. W. Zhu, Plasmonics for surface-enhanced Raman scattering: from classical to quantum. Doctoral dissertation, Harvard University, 2014.

132. J. S. Thakur, H. Dai, G. K. Serhatkulu, R. Naik, V. M. Naik, A. Cao, A. Pandya, G. W. Auner, R. Rabah, M. D. Klein. C. Freeman, J. Raman Spectrosc., 38 (2007) 127.

133. Y. Oshima, H. Shinzawa, T. Takenaka, C. Furihata, H. Sato, J. Biomed. Opt., 15 (2010) 17009.

134. A. B. Veloso, J. P. F. Longo, L. A. Muehlmann, B. F. Tollstadius, P. E. N. Souza, R. B. Azevedo, P. C. Morais, S. W. da Silva, Sci. Rep., 7 (2017) 74691.

135. F. Hennrich, K. Krupke, S. Lebedkin, K. Arnold, R. Fischer, D. E. Resasco, M. M. Kappes, J. Phys. Chem. B., 109 (2005) 10567.

136. E. Dube, N. Nwaji, D. O. Oluwole, J. Mack, T. Nyokong, J. Photochem. Photobiol. A, 349 (2017) 148.

137. D. Qu, M. Zheng, L. Zhang, H. Zhao, Z. Xie, X. Jing, E. H. Raid, H. Fan, Z. Sun, Sci. Rep., 4 (2014) 5294.

138. T. Mthethwa, E. Antunes, T. Nyokong, Dalton Trans., 43 (2014) 8230.

139. S. Liu, G. Chen, P.N. Prasad, M.T. Swihart, Chem. Mater., 23 (2011) 4098.

140. N. Rapulenyane, E. Antunes, T. Nyokong, New J. Chem., 37 (2013) 1216.

141. N. Masilela, T. Nyokong, J. Photochem. Photobiol. A, 223 (2011) 124.

142. N. R. Jana, L. Gearheart and C. J. Murphy, J. Phys.Chem. B, 105 (2001) 4065.

143. S. Banfi, G. Nasini, S. Zaza, E. Caruso, Tetrahedron, 69 (2013) 4845.

144. W. Chidawanyika, T. Nyokong, Carbon, 48 (2010) 2831.

145. P. Ma, F. Liang, Q. Diao, D. Wang, Q. Yang, D. Gao, D. Song, X. Wang, RSC Adv., 5 (2015) 32168.

146. Z. Li, C. He, Z. Wang, Y. Gao, Y. Dong, C. Zhao, Z. Chen, Y. Wu, W. Song, Photochem. Photobiol. Sci., 15 (2016) 910.

147. K. Kameyama, M. Morisue, A. Satake, Y. Kobuke, Angew Chem., 117 (2005) 4841.

148. M. Morisue, S. Ueda, M. Kurasawa, M. Naito, Y. Kuroda, J. Phys. Chem. A., 116 (2012) 5139.

149. Y. Wang, L. Zhang, R. P. Liang, J. M. Bai, Anal. Chem., 85 (2013) 9148.

150. X. Wu, F. Tian, W. Wang, J. Chen, M. Wu, J.X. Zhao, J. Mater. Chem. C., 31 (2013) 4676.

151. I. Uddin, P. Poddar, N. Phogat., Mater. Focus, 2 (2013) 80.

152. M. Bouchoucha, R. C. Gaudreault, M. A. Fortin, Adv. Funct. Mater., 24 (2014) 5911.

153. P. P. Joshi, S. J. Yoon, W. G. Hardin, S. Emelianov, K. V. Sokolov,. Bioconjug. Chem., 24 (2013) 878.

154. K. C. Nguyen, Adv. Nat. Sci.: Nanosci. Nanotechnol., 3 (2012) 45008.

155. B. Lambert, H. F. Shurvell, D. A. Lightner, R. G. Cooks, Introduction to Organic Spectroscopy, Macmillan, New York, (1987).

156. L. Stobinski, B. Lesiak, A. Malolepszy, M. Mazurkiewicz, B. Meirzwa, J. Zemek, P. Jiricek, P. Bieloshapka, J. Electron Spectrosc. Relat. Phenom., 195 (2014) 145.

157. Y. Wang, C. Zhang, H. Li, G. Zhu, S. Bao, S. Wei, L. Zheng, M. Ren, Z. Xu, J. Mater. Chem. B, 3 (2015) 296.

158. Y. Li, Y. Hu, Y. Zhao, G. Q. Shi, L. E. Deng, Y. B. Hou, L. T. Qu, Adv. Mater., 23 (2011) 776.

159. C. K. Chua, Z. Sofer, P. Šimek, O. Jankovský, K. KlÍmová, S. Bakardjieva, S. H. Kučková, M. Pumera, ACS Nano, 9 (2015) 2548.

160. R. E. Dinnebier, S. J. L. Billinge Eds, Powder Diffraction: Theory and Practice, RSC Publishing, Cambridge, (2008).

161. J. Ji, D. Wu, L. Liu, J. Chen, Y. Xu, Polym. Bull., 68 (2012) 1707.

162. R. Jenkins, R. L. Synder, Introduction to X-ray Diffractometry, Wiley and Sons, New York, 1996.

163. S. Kim, D. H. Shin, C. O. Kim, S. S. Kang, S. S. Joo, S. H. Choi, S. W. Hwang C. Sone, Appl. Phys. Lett., 102 (2013) 53108.

164. W. Chidawanyika, T. Nyokong, Carbon, 48 (2010) 2831.

165. E. P. Dillon, C. A. Crouse, A. R. Barron, ACS Nano, 2 (2008) 156.

166. K. Yang, M. Gu, Y. Guo, X. Pan, G. Mu, Carbon, 47 (2009) 1723.

167. R. Schmidt, E. McNellis, W. Freyer, D. Brete, T. Grebel, C. Gahl, K. Reuter, M. Weinelt, Appl. Phys. A., 93 (2008) 267.

168. T. Ming, L. Zhao, H. Chen, K. C. Woo, J. Wang, H. Lin, Nano Lett., 11 (2011) 2296.

169. X. Huang. X. M. A. El-Sayed. J. Adv. Res., 1 (2010) 13.

170. K. E. Achuyuthan, A. M. Achyuthan, S. M. Brozik, S. M. Dirk, T. R. Lujan, J. M. Romero, J. C. Harper, Anal. Sci., 28 (2012) 433.

171. M. T. Colvin, A. B. Ricks, A. M. Scott, D. T. Co, M. R. Wasielewski, J. Phys. Chem. A, 116 (2012) 1923.

172. C. D. Geddes, J. R. Lakowicz, J. Fluoresc., 12 (2002) 121.

173. J. R. Lakowicz, Y. Shen, S. D'Auria, J. Malicka, J. Fang, Z. Gryczynski, I. Gryczynski, Anal. Biochem., 301 (2002) 261.

174. Y. Kaneko, Y. Nishimura, N. Takane, T. Arai, H. Sakuragi, N. Kobayashi, D. Matsunaga, C. Pac, K. Tokumaru, J. Photochem. Photobiol.: A, 106 (1997) 177.

175. O. J. Achadu, I. Uddin, T. Nyokong, J. Photochem. Photobiol.: A, 317 (2016) 12.

176. J. R. Lakowicz, Anal. Biochem. 298 (2001) 1.

177. J.R. Lakowicz, Anal. Biochem. 337 (2005) 171.

178. M. G. Debacker, O. Deleplanque, B. Van Vlierberge, F. X. Sauvage, Laser Chem., 8 (1988) 1.

179. G. Bottari, G. de la Torre, D.M. Guldi, T. Torres, Chem. Rev., 110 (2010) 6768

180. G. Bottari, J.A. Suanzes, O. Trukhina, T. Torres, J. Phys. Chem. Lett., 2 (2011), 905.

181. S. T. Sivapalan, B. M. DeVetter, T. K. Yang, T. Dijk, M. V. Schulmerich, P. S. Carney, R. Bhargava, C. J. Murphy, ACS Nano, 7 (2013) 2099.

182. K. Furusawa, Z. Shou, N. Nagahashi, Colloid Polym. Sci., 270 (1992) 212.

183. N. A. R. M. Afrooz, S. T. Sivalapalan, C. J. Murphy, S. M. Hussain, J. J. Schlager, N. B. Saleh, Chemosphere, 91 (2013) 93.

184. S. E. J. Bell, M. R. McCourt, J. Phys. Chem. Chem. Phys., 11 (2009) 7455.

185. A. M. Schwartzberg, C. D. Grant, A. C. Wolcott, E. Talley, T. R. Huser, R. Bogomolni, J. Z. Zhang, J. Phys. Chem. B, 108 (2004) 19191.

186. C. Fang, Y. Xie, M. R. Johnston, Y. Ruan, B. Z. Tang, Q. Peng, Y. Tang, J. Phys. Chem. A, 119 (2015) 8049.

187. N. R. Yaffe, E. W. Blanch, Vib. Spectrosc., 48 (2008) 196.

188. S. Sánchez-Cortés, J. V. Garcia-Ramos, G. Morcillo, J. Colloid Interface Sci., 167 (1994) 428.

189. P. Larkin. Infrared and Raman Spectroscopy: Principles and Spectral Interpretation, Elsevier Inc: New York, 2011.

190. I. Dolamic, B. Varnholt, T. Bu¨rgi, Phys.Chem. Chem. Phys., 15 (2013) 19561.

191. B. Varnholt, P. Oulevey, S. Luber, C. Kumara, A. Dass, T. Bürgi, J. Phys. Chem. C, 118 (2014) 9604.

192. T. Shang, C. Wang, L. Ren, X. Tian, D. Li, X. Ke. Chen, A. Yang, Nanoscale Research Letters, 8 (2013) 4.